ANOMALIES OF GEOMAGNETIC VARIATIONS IN THE SOUTHWESTERN UNITED STATES

BY

ULRICH SCHMUCKER

UNIVERSITY OF CALIFORNIA PRESS
BERKELEY · LOS ANGELES · LONDON
1970

BULLETIN OF THE SCRIPPS INSTITUTION OF OCEANOGRAPHY
OF THE UNIVERSITY OF CALIFORNIA
LA JOLLA, CALIFORNIA

Volume 13

Approved for publication January 12, 1968
Issued March 26, 1970
Price, $3.00

UNIVERSITY OF CALIFORNIA PRESS
BERKELEY AND LOS ANGELES
CALIFORNIA

◆

UNIVERSITY OF CALIFORNIA PRESS, LTD.
LONDON, ENGLAND

[CONTRIBUTION FROM THE SCRIPPS INSTITUTION OF OCEANOGRAPHY, NEW SERIES]

ISBN: 0-520-09318-6

LIBRARY OF CONGRESS CATALOG CARD NUMBER: 72-627675

PRINTED IN THE UNITED STATES OF AMERICA

CONTENTS

Abstract ix
Notation x

1. Introduction 1
    1.1 Induction anomalies of geomagnetic variations 1
    1.2 Basic equations 2
    1.3 Conductivity distribution in the earth's crust and mantle . . . 5
    1.4 The conductivity-temperature relation in the upper mantle . . 7

2. Instruments and Field Operations 9
    2.1 Askania variograph 9
    2.2 Intercalibration of the variographs 9
    2.3 Temperature coefficients of the variometers 10
    2.4 Time signals and synchronization of records 10
    2.5 Field stations 11
    2.6 Base-line control 12
    2.7 Causes for loss of records 12

3. Data Reduction 13
    3.1 Basic concepts 13
    3.2 Selection of time intervals for analysis 14
    3.3 Scaling and scaling errors 14
    3.4 Separation of anomalous and normal parts 15
    3.5 Power and cross spectra 16
    3.6 Spectral analysis of single events 17
    3.7 Spectra of storms 19
    3.8 Correlation analysis between anomalous and normal parts (transfer functions) 20
    3.9 Residuals 21
    3.10 Induction and perturbation arrows 22
    3.11 Special case I: Unrelated normal Z-variations 24
    3.12 Special case II: Elongated anomalies 24
    3.13 Special case III: Pilot study 25
    3.14 Contribution of scaling errors to residuals 26
    3.15 Examples for correlated Z-variations 28
    3.16 Separation of internal and external parts 29
    3.17 Analysis of diurnal variations and pulsations 32

4. Description of the Anomalies 33
   - 4.1 Introduction 33
   - 4.2 Rio Grande anomaly of bays and other fast disturbances . . . 33
   - 4.3 Rio Grande anomaly of diurnal variations 36
   - 4.4 Coastal anomaly in California of bays and other fast disturbances 38
   - 4.5 Inland anomalies in California and Nevada 46
   - 4.6 Coastal anomaly in California during magnetic storms 49
   - 4.7 Anomalies of diurnal variations in California 52
   - 4.8 Anomalies of pulsations in California 53
   - 4.9 IGY network in the midwestern United States 53

5. Electromagnetic Induction in Stratified Conductors 55
   - 5.1 Introduction and references 55
   - 5.2 Spherical conductors 56
   - 5.3 Plane conductors 61
   - 5.4 Special case I: Uniform conductors 66
   - 5.5 Special case II: 2-layer model 68
   - 5.6 Direct Inversion of Surface Observations 69
   - 5.7 Special case III: Limitations of PRICE's method 69
   - 5.8 Shell-core and sheet-substratum models 72

6. Electromagnetic Induction in Nonuniform Conductors 77
   - 6.1 Introduction 77
   - 6.2 Surface anomalies 78
   - 6.3 Relaxation method for surface anomalies 79
   - 6.4 Intermediate anomalies 81
   - 6.5 Deep anomalies: 1st interpretation 82
   - 6.6 Deep anomalies: 2nd interpretation 83
   - 6.7 Conformal mapping methods 86

7. Interpretation of the Anomalies 92
   - 7.1 Primary source field and mean conductivity distribution . . . 92
   - 7.2 Coastal anomaly in California 93
   - 7.3 Method of calculations 100
   - 7.4 Inland anomalies in California and Nevada 103
   - 7.5 Rio Grande anomaly 104

Conclusions and Suggestions for Further Work 113
Acknowledgment 114
Appendix I: Trend Functions for the Long-periodic Background of Single Events 117
Appendix II: Spherical Bessel Functions 119
Appendix III: Elliptic Surface Anomalies 121
Appendix IV: Computer Programs 125

Literature Cited 127
Table 1: Error Residuals in Z (Eq. 3.29). 133
Table 2: Normalized Sheet-Current Density in the Ocean (Q_ϕ) Offshore the California Coast and in Surface Layers on Land (Q_L). From Equations 6.5 and 7.2 133
Table 3: Depth of Perfect Substitute Conductor h^* in (km). 133
Table 4: List of Survey Stations 134
Tables 5-10: Transfer Values between the Anomalous and Normal Parts of Bays and Other Fast Variations 139
Tables 11-15: Second and Third Time Harmonic of Diurnal Variations during Quiet Days (Sec. 3.17) 153
Table 16: Mean Amplitude Ratio of Vertical to Horizontal Pulsations (Sec. 3.17). 158
Plates I-VI 160

ANOMALIES OF GEOMAGNETIC VARIATIONS IN THE SOUTHWESTERN UNITED STATES

BY

ULRICH SCHMUCKER

ABSTRACT

Local differences of transient geomagnetic variations have been studied in the southwestern United States with a network of temporary magnetic field stations, equipped with Askania variographs. Large anomalous Z-variations, accompanied by a slight reduction of the horizontal amplitude, have been found along the California coast for fast and slow variations (bays, magnetic storms, diurnal variations). These coastal Z-variations gradually disappear inland, within about 200 km from the coast. The coastal anomaly of bays and other fast disturbances are interpreted as an "edge effect" of oceanic induction currents. This interpretation suggests relatively high internal conductivities under the California coast when compared to Lahiri and Price's model "d".

Less prominent anomalies of fast variations occur further inland in California and Nevada which are explicable partially by superficial conductivity contrasts. There remain, however, clear indications of a local uplift of highly conductive mantle material along the eastern slope of the Sierra Nevada and near Napa, north of San Francisco. Both areas are characterized by young volcanic activity and high terrestrial heat flow, supporting the hypothetical correlation between high internal temperatures and high conductivities.

A profile of stations from Tucson, Arizona, to Sweetwater, Texas, revealed a general reduction of the Z-amplitude of fast and slow variations west of the Rio Grande, accompanied by a local increase of the D-amplitude at Las Cruces, New Mexico. These observations have been interpreted by a general increase of mantle conductivity under the southern Arizona Rockies and a zone of very high conductivity under the Rio Grande Rift Belt, which is noted for its intensive vulcanism in recent times. The mantle under southern Arizona and the California coast seems to be three times better conducting than the mantle under West Texas at the same level between 50 and 300 km depth, which could be explained by a lateral temperature increase of 100° C from east to west. These conclusions conform with changes of terrestrial heat flow. Velocity and attenuation of seismic P_n-waves undergo likewise a distinct change between West Texas and southern Arizona.

NOTATION

All quantities are measured in electromagnetic C.G.S. units (emu). Electrical conductivity values are quoted occasionally in the M.K.S. unit $(\Omega m)^{-1}$ which is equivalent to 10^{-11} emu. A convenient unit of the electric field is (mV/km) = 1 emu. The time factor of harmonic oscillations is always $\exp(+i\omega t)$ and frequencies are given usually in cycles per hour = cph. The letters "u" and "v" identify as subscript or added in parenthesis the real and imaginary part of complex quantities, e.g., $z_P = z_P(u) + i\, z_P(v)$. Bold type characters indicate vectors.

A	earth's radius
$\mathbf{c}$	induction arrow, pertaining to Z_a (sec. 3.10)
c(f)	complex parameter (a length), representing a stratified conducting substratum for a given frequency (sec. 5.5/6)
$C_X(f)$	Fourier transform of X(t) (eq. 3.3)
D(t)	magnetic east component of $\mathbf{F}(t)$
$\bar{D}$, D_a	normal and anomalous part of D(t)
d_H, d_D, d_Z	transfer functions for D_a (sec. 3.8)
f	frequency
$\mathbf{F}(t)$	magnetic variation vector
$\bar{\mathbf{F}}$, $\mathbf{F}_a$	normal and anomalous part of $\mathbf{F}(t)$
H(t)	magnetic north component of $\mathbf{F}(t)$ except chapters 5 and 6
$\mathbf{H}(t)$	chapters 5 and 6: horizontal component of $\mathbf{F}(t)$
$\bar{H}$, H_a	normal and anomalous part of H(t)
h_H, h_D, h_Z	transfer functions for H_a (sec. 3.8)
$\mathbf{H}^+(t)$	tangential components of $\mathbf{F}(t)$ on outer (+) and inner
$\mathbf{H}^-(t)$	(-) surface of a thin conducting sheet or shell
h_P	projection of the horizontal transfer functions h_H, h_D and d_H, d_D on the direction of a profile of field stations (eq. 3.26)
$h^*(f)$	depth of perfect substitute conductor, real part of c(f)
i	$\sqrt{-1}$
j(t)	integrated sheet current density per unit length in thin sheets or shells (eq. 1.8)
$\bar{j}$, j_a	normal and anomalous part of j(t)
$j_n(iz)$	spherical Bessel function of the 1st kind (App. II)
k	wave number of primary source field in nonconducting medium

K	propagation constant of downward diffusing field in stratified conductors (eqs. 5.11 and 31).
Kf	Kertz's operator applied to f(x) (sec. 3.16)
p_ν	skin-depth value of the ν^{th} layer (eq. 5.1)
$p_c(f)$	skin-depth value of the uniform substitute conductor, $p_c/2$ is the imaginary part of c (f)
p, **q**	perturbation arrows (sec. 3.10), pertaining to H_a and D_a
Q	normalized sheet-current density (eq. 6.4)
Q*	1-2 Q
q_H, q_Z	transfer functions for j_a (eq. 6.6)
$S_X(f)$	power spectrum of X (t)
$S_{XY}(f)$	cross spectrum between X (t) and Y (t)
t	time
Y	true east component of **F** (t)
Z (t)	vertical component of **F**(t), positive down
$\overline{Z}$, Z_a	normal and anomalous part of Z (t)
z_H, z_D, z_Z	transfer functions for Z_a (sec. 3.8)
z_P	projection of vertical transfer functions z_H and z_D on the direction of a profile of field stations (eq. 3.26)
∇^2	Laplacian operator
ϵ_D, ϵ_H, ϵ_Z	residuals of correlation analysis (sec. 3.9)
$\mathfrak{E}$	tangential electric variation vector (eq. 5.40)
η_n, $\eta(k)$	induction parameter of uniform conductors (sec. 5.4)
η_s	induction parameter of shell-core models (sec. 5.8)
$\eta_n(iz)$	spherical Bessel functions of the 2nd kind (App. II)
σ	electrical conductivity
τ	total conductivity of thin sheets or shells (eq. 1.7)
$\overline{\tau}$, τ_a	normal and anomalous part of τ
ω	$2\pi f$

1. INTRODUCTION

1.1 Induction Anomalies of Geomagnetic Variations

Superposed upon the permanent magnetic field of the earth are those transient fluctuations of small amplitude and short duration which are commonly known as geomagnetic variations. They consist of two parts, one of external and the other of internal origin. The external and primary part arises from transient current systems in the ionosphere or beyond. The internal part is from secondary eddy currents which are induced electromagnetically within the conductive layers of the earth's interior. These currents limit the depth of penetration of the incident variation field which varies from a few kilometers for fast pulsations (60 cph = cycles per hour) to hundreds of kilometers for the slow diurnal variations (1/24 cph). Hence, the subterranean eddy currents flow during sufficiently slow variations well within the earth's upper mantle, thereby revealing the internal distribution of electrical conductivity down to a depth of, say, 600 km.

Except for a complex outermost shell of oceans and continental surface layers we may assume that the conductivity changes primarily with depth in accordance with the radial changes in composition, temperature, and pressure (sec. 1.4). Currents which are induced from the outside in such a stratified conductor flow in concentric shells or sheets and produce a secondary surface field which resembles in its spatial configuration the primary source field from above.

Suppose pronounced and consistent differences occur among simultaneously recorded variations at adjacent sites, say, less than 100 km apart, and suppose that they cannot be related to some ionospheric current concentration such as the equatorial or auroral jet. We may conclude then that these differences are anomalous in the sense that they are of internal origin and due to an unequal distribution of conductivity. The resulting perturbation of the otherwise stratified flow of internal eddy currents is responsible for the observed induction anomaly of the transient variation field at the earth's surface. It is the objective of geomagnetic depth sounding to find such anomalies with a closely spaced net of temporary magnetic recording stations.

This presentation deals with various anomalies which were discovered in the southwestern United States between 1959 and 1962. A preliminary evaluation of the material presented here has been published in the proceedings of the Berkeley symposium on geomagnetic induction problems (Schmucker, 1964). A comprehensive review of the entire subject can be found in Rikitake's treatise entitled "Electromagnetism and the earth's interior" (1966).

At first sight the electrical conductivity σ of subterranean matter may not seem to be a very noteworthy parameter. There is, however, its close relation to temperature, following the general theory of semiconduction, and even a relatively small rise in ambient temperature may cause a substantial increase of the conductivity (sec. 1.4). We have to bear in mind, however, that semiconduction in nonmetallic solids is primarily an impurity effect. Thus, minute changes of composition can have an equally strong effect upon σ, not counting the largely unknown influence of pressure.

This limits the effective use of the conductivity as an absolute thermometer for the earth's interior. There remains, however, the important aspect to use σ as relative thermometer, namely, to infer deep-seated lateral gradients of conductivity and possibly temperature from their distorting effect upon the internal part of geomagnetic variations. Such thermal imbalances in the upper mantle could be connected with ascending and descending branches of convection cells or with local concentrations of radioactive heat sources, which may be the underlying cause for the diversified tectonic and magmatic history of the earth's outermost layers.

Two inherent limitations of geomagnetic depth sounding should be mentioned. Since the magnetic observations are made within a small area, small in comparison to the spatial extent of the primary inducing field from above, a complete separation of internal and external parts of the transient variation field is not possible. A separation of this kind would be necessary to determine the overall change of conductivity with depth in the surveyed area (sec. 1.3). Hence, induction anomalies of the internal part, which are recognized usually without formal separation of internal and external parts, have to be interpreted on the basis of a preconceived mean conductivity distribution which has been inferred as function of depth from other sources of information (sec. 1.3).

Second, oceans and continental surface layers form a thin conducting cover of great complexity. The flow of shallow eddy currents is therefore highly distorted, in particular near coastlines because of the outstanding conductivity contrast of seawater and rock formations on land. This may or may not lead to an anomalous behavior of geomagnetic variations, depending on the relative strength of those eddy currents and their contribution to the internal part in the area under consideration. Surface effects of this kind have to be taken into account before postulating a deep-seated cause for a given induction anomaly.

1.2 Basic Equations

The incident variation field diffuses downward through the conducting layers of the earth with amplitude reduction and phase rotation. The governing equations are Maxwell's field equations of the transient electromagnetic vector field $\mathbf{E}$ and $\mathbf{F}$. We use here their quasi-stationary approximation (in emu):

$$\operatorname{curl} \mathbf{F} = 4\pi\sigma\mathbf{E} \qquad \text{and} \qquad \operatorname{curl} \mathbf{E} = -\mu\,\partial\mathbf{F}/\partial t \qquad (1.1)$$

with $\text{div}(\mu\mathbf{F}) = 0$, σ denoting the isotropic conductivity and μ the magnetic permeability.

We disregard the small deviation of μ from unity above and within the earth and set $\mu = 1$. This renders $\text{div}\,\mathbf{F} = 0$ and makes $\mathbf{F}$ expressible as sum of a poloidal and a toroidal vector field. The toroidal mode has no radial component (in spherical coordinates) and is connected therefore with the minute magnetic effect of vertical displacement currents in the air above the ground which we consider a perfect insulator ($\sigma = 0$). This effect is not contained in the quasi-stationary approximation (1.1).

Hence, we deal in the following only with the predominant poloidal magnetic mode which is irrotational in nonconducting matter and thereby derivable as gradient of a scalar potential function above the ground:

$$\mathbf{F} = -\text{grad}\,U \tag{1.2}$$

with $\nabla^2 U = 0$.

Using $\exp(i\omega t)$ as common time factor, the elimination of $\mathcal{E}$ from (1.1) gives

$$\nabla^2\mathbf{F} + \left[\frac{\text{grad}\,\sigma}{\sigma} \times \text{curl}\,\mathbf{F}\right] = 4\pi i\omega\mu\sigma\mathbf{F} \tag{1.3}$$

as basic differential equation for $\mathbf{F}$ below the earth's surface, where σ is a continuous and differentiable function of location. Outside and inside solutions for $\mathbf{F}$ are linked by the continuity condition that the field vector passes without change from the nonconducting air into the conducting layers below the ground.

The associate current field $\sigma\mathcal{E}$ is likewise nondivergent for the quasi-stationary approximation and toroidal. Hence, equation 1.3 does not contain the magnetic effect of radial current components. We observe that

$$\sigma\,\text{div}\,\mathcal{E} = -(\mathcal{E}\cdot\text{grad}\,\sigma) \tag{1.4}$$

since $\text{div}(\sigma\mathcal{E}) = 0$. Thus, volume charges and their electrostatic effects render $\text{div}\,\mathcal{E} \neq 0$ in the presence of tangential conductivity gradients.

We return to the magnetic variation field, which is of prime interest here, and introduce the following perturbation type approach. Considering the conductivity σ at a certain subsurface level z we distinguish between its constant normal part $\bar{\sigma}$ and its variable anomalous part σ_a. The transient magnetic field vector shall be likewise the sum of a normal plus anomalous part, $\mathbf{F} = \bar{\mathbf{F}} + \mathbf{F}_a$, the latter representing the superficial induction anomaly of the observed variation field.

Let us replace the normal conductivity distribution $\bar{\sigma}(z)$ by a stratified substratum, consisting of various layers of uniform but different conductivity. Equation 1.3 then reduces to a diffusion equation

$$\nabla^2\bar{\mathbf{F}} = 4\pi i\omega\mu\bar{\sigma}\bar{\mathbf{F}} \tag{1.5}$$

for the normal variation field in each layer. Appropriate solutions will be presented in chapter 5.

For the superimposed anomalous variation field we obtain in a similar way

$$\nabla^2 \mathbf{F}_a + \left[\frac{\text{grad }\sigma}{\bar{\sigma} + \sigma_a} \text{ x curl } (\bar{\mathbf{F}} + \mathbf{F}_a)\right] = 4\pi i\omega\mu \;\; [\; \bar{\sigma}\, \mathbf{F}_a + \sigma_a(\bar{\mathbf{F}} + \mathbf{F}_a) \;] \quad (1.6)$$

where $\bar{\mathbf{F}}$ is a solution of (1.5), so that $(\bar{\mathbf{F}} + \mathbf{F}_a)$ satisfies the starting equation (1.3). Thus, (1.6) is the basic equation for the interpretation of induction anomalies in terms of lateral conductivity variations σ_a within a preconceived normal distribution $\bar{\sigma}(z)$.

A difficult obstacle for geomagnetic depth sounding is the irregular flow of eddy currents in oceans and continental surface layers as pointed out above. Pertinent calculations are greatly simplified when we use Price's method (1949) concerning the induction in thin sheets (or shells) which are embedded in nonconducting matter. The induction in such sheets is controlled by the transverse magnetic field component Z and by their total conductivity

$$\tau = \int_0^d \sigma(z)\,dz. \quad (1.7)$$

The integration is carried out over the thickness d of the sheet from the outer to the inner side. The integrated sheet-current density per unit length follows then as

$$\mathbf{j} = \int_0^d \mathcal{E}(z) \cdot \sigma(z)\,dz = \mathcal{E} \cdot \tau \quad (1.8)$$

when $\mathcal{E}(z)$ is treated as a constant. Limits for the required uniformity of the electric field vector are discussed in section 5.7.

Let $\mathbf{H}^+$ and $\mathbf{H}^-$ be tangential field vectors at corresponding points on the outer and inner side of the sheet. Because of the thinness of the sheet we may set

$$4\pi\mathbf{j} = [\; \mathbf{n} \text{ x } (\mathbf{H}^+ - \mathbf{H}^-)] , \quad (1.9)$$

(Price's eq. 7), where $\mathbf{n}$ is a unit vector pointing normal to the sheet from the inner to the outer side. The sheet may be nonuniform, i.e., τ may vary from place to place, provided that these variations occur on a scale which is large in comparison to d. This ensures that the vertical component Z passes without change through the sheet, $Z^+ = Z^-$.

Internal and external magnetic solutions are linked by the boundary conditions

$$\text{div}(\mathbf{H}^+ - \mathbf{H}^-) - \left(\frac{\text{grad } \tau}{\tau} \cdot [\mathbf{H}^+ - \mathbf{H}^-]\right) = 4\pi i\,\omega\tau Z \quad (1.10)$$

(Price's eq. 9) which is the "thin-sheet version" of (1.3), Z being positive down. The right-hand side contains in Z the driving force of the induced sheet current while the term containing grad τ directs this current around zones of low into zones of high conductivity. Considering again separate solutions for a normal state $(\bar{\mathbf{H}}, \bar{Z}, \bar{\tau})$ and a superimposed perturbation $(\mathbf{H}_a, Z_a, \tau_a)$ we obtain in analogy to (1.5) and (1.6)

$$\text{div}(\bar{\mathbf{H}}^+ - \bar{\mathbf{H}}^-) = 4\pi i\omega\mu\bar{\tau}\bar{Z} \quad (1.11)$$

$$\text{div}(\mathbf{H}_a^+ - \mathbf{H}_a^-) - \left([\text{grad }\tau]/\tau \cdot [\mathbf{H}^+ - \mathbf{H}^-]\right) = 4\pi i\omega\mu(\bar{\tau}Z_a + \tau_a Z). \quad (1.12)$$

1.3 Conductivity Distribution in the Earth's Crust and Mantle

The electric conduction in near-surface rock formations is mainly electrolytic through salty solutions filling pores and cracks. Hence, unconsolidated clastic sediments have conductivities between 0.1 and 1 $[\Omega m]^{-1}$ $(= 10^{-11}$ cgs) in contrast to dense and therefore poorly conducting igneous rocks (0.01-0.001 $[\Omega m]^{-1}$; cf. Keller, 1966). Seawater in comparison has a conductivity of 3-4 (3.5% salinity, 0°-10°C), copper a conductivity of 10^8 $[\Omega m]^{-1}$.

Rocks become more and more insulating under pressure when their pores and cracks are closed, and the earth's crust must be indeed a very poor conductor. There is convincing evidence, however, that the conductivity rises again at greater depth and it is not unreasonable to relate this rise to the downward increase of temperature (sec. 1.4).

Two methods have been in use to infer the change of conductivity with depth from geomagnetic induction phenomena. The first and classical method (cf. Chapman and Bartels, chap. 22) is based on magnetic observations alone and uses the average surface ratio of internal to external parts, thereby smoothing out regional differences in the internal conductivity distribution. This method proved the existence of a conducting "core" beneath a high-resistivity intermediate zone and a thin conductive top layer of geological strata and oceans.

Lahiri and Price (1939) deduced two possible distributions, representing limiting cases, which are compatible with the internal parts of semidiurnal Sq-variations and smoothed storm-time D_{st}-variations. In the first model "e" an insulating layer extends downward to 600 km depth where the conductivity rises abruptly to infinity. The top layer has a total conductivity of $5.1 \cdot 10^{-6}$ emu·cm which is equivalent to about 1500 m of seawater (eq. 1.7).

In the alternative model "d" the conductivity rises smoothly with depth according to $\sigma(r) \sim (A/r)^{37}$ beneath a surface shell of 500 m seawater (r: distance from the earth's center, A: earth's radius). Starting with $\sigma(A) = 0.004$ $[\Omega m]^{-1}$ at zero depth the conductivity reaches 0.1 at 500 km and unity at 900 km depth (fig. 1).

The slow diurnal variations obviously propagate in either model with little attenuation through the upper mantle above 500 km, and their internal part cannot yield more than an upper permissible limit for the existing conductivity here. Detailed information about this depth range comes therefore from fast variations with a reduced depth of penetration. Rikitake (1950) was the first to attempt a worldwide analysis of bays and other short-period events. It soon became evident, however, that their internal part is subject to numerous anomalies and that the upper mantle must be extremely nonuniform as far as its conductivity is concerned.

Figure 1 shows the downward attenuation of bays within model "d", using a continental top layer with $4 \cdot 10^{-7}$ emu·cm as total conductivity. We see that the bulk of the eddy currents flows above 400 km depth. Thus, bays are ideally suited for geomagnetic depth sounding in the upper mantle beneath continents. Seawater, on the other hand, is conductive enough to shield bays

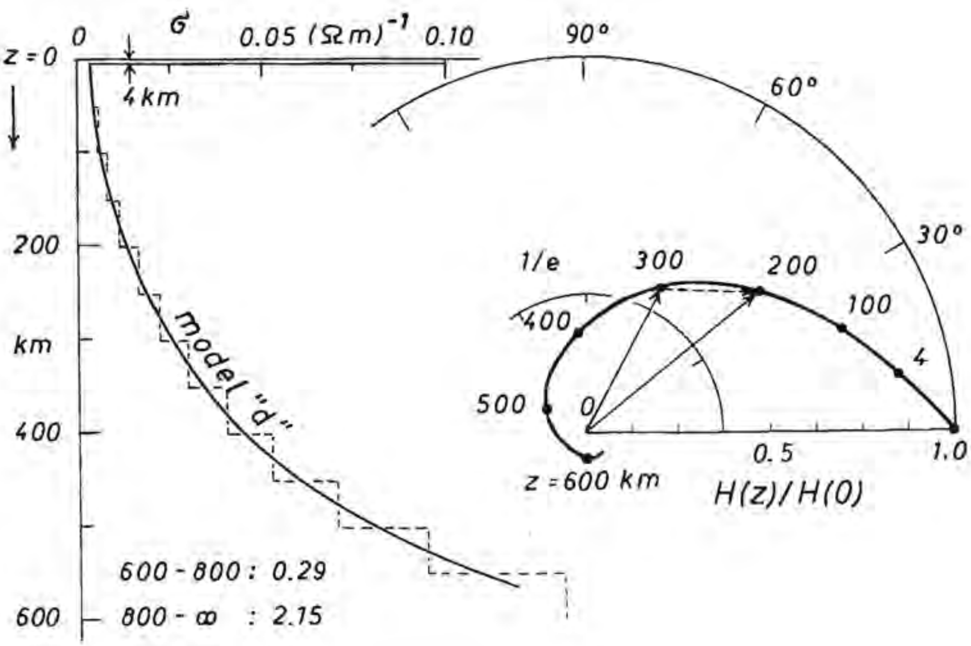

Fig. 1. Lahiri and Price's conductivity model "d" for the upper mantle beneath a continental surface cover. Polar diagram shows amplitude reduction and phase rotation of the tangential H-component of a downward diffusing bay ($f = 1$ cph). $H(z)$ lags in phase relative to $H(O)$ and is attenuated to $1/e$ at 330 km depth which may be regarded as depth of penetration of bays under normal continental conditions. Dashed arrow represents the relative amplitude ($\cdot 4\pi$) and phase of the integrated induction current within the indicated depth range. The calculations have been carried out for the dashed 15-layer approximation, evaluating equation 5.47,48 with $k = 0$.

from the underlying crust and mantle, even though this depends critically on the deep conductivity distribution (sec. 5.8). An oceanic top layer of 4 km thickness, for instance, would reduce the incident bay field to one-fifth of its surface amplitude, when model "d" is used for the crust and upper mantle.

The second method, introduced by Tichonov and Cagniard (1953), uses the surface impedance of the incident variation field, i.e., the ratio of tangential electric to orthogonal magnetic field fluctuations. It is presumed that the primary field is of great lateral uniformity in comparison to its depth of penetration. The impedance yields in this way as function of frequency estimates for the underlying conductivity as function of depth, excluding again lateral nonuniformities. The analysis of such magnetotelluric observations at various sites confirmed essentially the results of the first-mentioned magnetic method.

1.4 The Conductivity-Temperature Relation in the Upper Mantle

Probable mineral constituents of the upper mantle, e.g., olivine, are semiconductors, i.e., they are insulators at low temperatures and fairly good conductors at high temperatures according to the relation

$$\sigma(T) = \sigma_0 \cdot \exp(-T_0/T) \tag{1.13}$$

(T: absolute temperature in ° K). The coefficients σ_0 and T_0 are constants over limited ranges of T for a given pressure and composition. Their numerical values reflect the number, mobility, and activation energy of charge carriers which may be electrons (in the conduction band), corresponding holes (in the valence band), or positive and negative ions. Small impurities in the lattice are of great importance, since they can multiply the number and availability of such carriers. A concise review can be found in Hamilton's article (1965) and it may suffice to cite here some experimental results.

Hughes (1955) studied the conductivity of olivine as function of temperature and pressure between 1333° K and 1513° K and from 0 to 8.5 kbar which is the ambient pressure in 30 km depth. The natural logarithm of the conductivity showed for constant pressure a fairly linear relation to the inverse temperature as required by (1.13). Extrapolated to zero pressure the coefficients followed as $\sigma_0 = 2.1 \cdot 10^{-5}$ cgs and $T_0 = 31,200°$ K ($T_0/k = 2.7$ eV where k is Boltzmann's constant). This implies that the conductivity is doubled approximately by a temperature increase of $(T^2/T_0) \cdot \ell n\, 2 = 50°$ K within the indicated range.

Similar experiments by other authors led to comparable results (Tozer, 1959). It seems that the exponential coefficient T_0 is less dependent on the specific mineral composition than the preexponential coefficient σ_0. The influence of pressure is uncertain. Hughes found that the conductivity of olivine decreases about 4% per kbar pressure increase for a given temperature within the ranges from above. This he explained by a corresponding increase of T_0, i.e., by an increase of the necessary activation energy T_0/k to mobilize charge carriers. Hamilton (1965) came to different conclusions in a slightly lower temperature range. He found no change or even a small reduction of T_0 when the pressure was increased in steps from 11.5 to 31.8 kbar between different temperature runs.

In summary, the inversion of mantle conductivity into ambient temperature depends critically upon the assumed composition and the postulated influence of pressure. As stated by Hamilton with respect to olivine, a tenfold increase of its conductivity "can be produced by a 200° K increase in temperature (from 800 to 1000° K), a 10% increase in fayalite, or a 40 kbar increase in pressure" (according to his measurements). Further complications could arise from phase transitions in the upper mantle and their effect upon the conductivity, as demonstrated for the olivine-spinel transition by Akimoto and Fujisawa (1965). Little is known about the conduction in partially or completely molten mantle material.

Internal temperature gradients can be deduced with more confidence at the present state, since we avoid in this way the composition-dependent pre-exponential coefficient. Let ΔT and Δp be the temperature and pressure differences between two adjacent subsurface points. The corresponding difference in conductivity follows then from (1.13) as

$$\Delta\sigma = (T_0/T^2)\sigma\Delta T + (\partial\sigma/\partial p)\ \Delta p. \tag{1.14}$$

Inserting Hughes's values from above and measuring Δp in [kbar] gives for $T = 1250°$ C

$$\Delta\sigma/\sigma = 0.014\ \Delta T - 0.04\ \Delta p. \tag{1.15}$$

Thus, as already stated by Hughes, a downward temperature gradient of 1° C/km would be sufficient to compensate the opposing effect of pressure, increasing by roughly 0.35 kbar/km.

Since we expect a somewhat greater temperature gradient near the 1250° C isotherm, the conductivity should increase here downward under the dominating influence of temperature. Lahiri and Price's model "d", for instance, postulates a conductivity gradient of $(d\sigma/dr)/\sigma = -37/r$. Setting $r = 6200$ km gives in combination with Hughes's data a downward temperature gradient of 1.4° C/km. In the case of horizontal gradients we may disregard the pressure term and obtain a temperature-conductivity relation which is determined solely by the exponential coefficient T_0 for a given mean temperature $\overline{T}$ (cf. eq. 7.9).

2. INSTRUMENTS AND FIELD OPERATIONS

2.1 Askania Variograph

The survey was conducted with six Askania variographs, model Gv3. The variograph records continuously on 16 mm film the three components of the transient geomagnetic variations: D (positive magnetic eastward), H (positive magnetic northward), Z (positive downward). The film speed is 5 mm/hour, hence a 100-ft roll is sufficient for about eight months of record.

Providing that the optical system is occasionally readjusted the sharpness of the traces allows at least 12-fold magnification, thereby yielding a time resolution of 1 min/mm in Z. The variometers are of the classical type and employ suspended magnets in proper orientation. They are mounted inside a temperature insulated cylindrical container, and an intricate mirror system gives an effective optical lever of about three meters.

At field sites where AC power is available the variograph can be operated with thermostat control, requiring 50 watts. If the variograph has to be operated on batteries, requiring 6 ampere hours/day, temperature compensation and additional temperature protection of the instrument are essential when the evaluation of long periodic variation is desired.

Prior to the actual field operations the original sensitivities of the D-variometer were doubled to match those of the H-variometer. For that purpose a pair of compensation magnets were installed near the D-system to bias the horizontal magnetic field intensity. Since transient fluctuations in Z would be of particular importance during the survey, the sensitivity of the Z-variometer was also increased by adding a small coil of thin copper wire as trimmer weight to the system. This trimmer weight lifted the center of mass of the suspended Z-system closer to its axis of rotation, thereby making the system less stable.

2.2 Intercalibration of the Variographs

The detection and analysis of anomalous variations requires a precise intercomparison of magnetograms from different instruments at different sites. Therefore the six variographs were carefully intercalibrated by operating them side by side for about four months at Scripps Institution, La Jolla. This test has been conducted twice, at the beginning and in the middle of the program.

During these test runs recordings of disturbed and quiet days were scaled and intercompared among the six variographs. They were found to agree within ± 1 gamma when scale values according to the best possible fit were adopted. The linearity of the scale values, the orientation of the systems, and the interaction among the variometers for the three components were checked at the same time. The orientation proved to be correct within the limits specified in the Askania certificates. This brought the H-sensitivity of the D-system, the D-sensitivity of the H-system, and the D-sensitivity of the Z-system below 1 mm/100 gammas. Any nonlinearity of the scale values or any interaction between the variometers proved to be negligible.

During the subsequent field operations great care was taken at all times to keep the errors of the scale-value determinations within 1-2%. This required a regular check of the amperemeters of the calibration circuits against a standard amperemeter.

2.3 Temperature Coefficients of the Variometers

Temperature effects upon the variometers were thoroughly investigated. The H-systems have a built-in temperature compensation. Their suspension fibers consist of two different materials and their combined temperature effect nearly cancels the temperature effect of the magnet. The remaining temperature coefficient was determined to about +1.5 gammas/° C for all six H-variometers.

In order to temperature-compensate the Z-variometer the torsion ratio of its two suspension fibers has to be readjusted for the vertical intensity of the permanent field at each recording site. This adjustment requires lengthy temperature tests, extending over several weeks, since the Z-system usually starts to drift when the torsion of the fibers is changed.

These tests were conducted during the trial period at La Jolla and temperature compensation within ±3 gammas/° C was achieved in general. The small additional change in torsion at the actual field site was conducted in such a manner that the temperature coefficient remained unaffected. A detailed report on this subject has been prepared for the Instituto Geofisico del Peru, Apt. 3747, Lima; Ing. A. A. Giesecke, director.

It should be pointed out that subsequent temperature corrections on the basis of the recorded temperature variations inside the variograph are of limited value, since the temperature response of noncompensated Z-systems is not linear. This underlines the importance to achieve a high degree of temperature compensation with tests of sufficient length.

2.4 Time Signals and Synchronization of Records

Hourly time signals were provided from electric clocks driven by synchronous motors from the local mains. They proved to be accurate within seconds for any length of time due to precise cycle control of the mains in the United States. At battery-operated stations electrically wound chronometers were employed. In addition each day a programming device gave for five minutes an automatic calibration of 50 gammas in all components. This daily check of the scale values became quite important when the variograph came slowly out of level, for instance, after heavy rainfalls. This led eventually to friction in the vertically suspended D- and H-systems resulting in faulty records. However, such a malfunction could be recognized from erratic changes of the scale values.

Numerous difficulties arose from the electric clock drive for the 16 mm recording film. The transmission of this clock drive proved to be very delicate and required continuous attention. The film progress was irregular and jerky, varying often from hour signal to hour signal by 4%. This impaired the correct synchronization of records from different sites, and additional time marks, say, every ten minutes, would have been desirable.

2.5 Field Stations

The stations were normally set up in profiles. The distance between adjacent stations varied between 20 km and 100 km depending on the nature of the anomaly being encountered. Each profile of six stations was kept in operation until a sufficient number of disturbed and quiet days and numerous isolated events, such as bays, had been observed simultaneously at all stations. This required an average recording time of three months.

Observations were made at 49 sites between October 1959 and July 1962 (fig. 2). Table 4 gives a complete list of the field stations together with pertinent data.

Fig. 2.

At the field site the variographs were housed in aluminum shelters of 3 x 5 sq ft ground area standing 6 ft high. The shelter, made by the Cabana Co. of Los Angeles, consisted of five plates which were screwed together in situ with aluminum screws. The Askania control box, the clock, and the storage batteries were placed in a wooden box at some distance from the shelter.

The field stations were usually operated in cooperation with the science departments of local high schools, as requested in the NSF grant. The instruments were then installed on school grounds or at "magnetically quiet" places nearby, for instance, on rural airports.

Most stations were supplied from the main electrical net. Batteries were used only at very remote sites. After installation and a trial period of a few days the instruments were left in care of local operators, whenever possible, and inspected about once in four weeks.

2.6 Base-line Control

Absolute magnetic observations have not been made at the field sites and an absolute base-line control was therefore not possible. Instead a relative base-line control was maintained by comparing midnight differences of succeeding days among the field stations. We may safely assume that these differences should be about the same even at widely separated sites. Discrepancies from station to station were attributed to instrumental drift, uncontrolled temperature effects, or faulty operation of the variometers in general. In D and H midnight differences usually agreed within ±2 gammas; Z-systems tended to drift considerably at new installations, but stabilized after about two weeks, yielding midnight discrepancies of ±3 gammas.

2.7 Causes for Loss of Records

In the course of the field operations the variometers themselves failed very seldom. A few times the suspension fibers of the Z-system slipped out of their fittings, thereby blocking the variometer. After reglueing the fibers with epoxy resin and after adjusting the sag of the Z-system, recording normally could be resumed without any further complications.

The main causes for the loss of records were (a) accidental shutoff of the power supply, (b) slip in the transmission of the recording film drive, (c) breakdown of the thermostat. When all six variographs were in operation, simultaneous records from all stations could be expected for about two thirds of the time.

3. DATA REDUCTION

3.1 Basic Concepts

Already a visual inspection of magnetograms from a closely spaced net of stations can reveal characteristic differences of the traces from site to site, which may or may not be connected with local induction anomalies. It has to be left to a more refined analysis, to recognize anomalies of truly internal origin, and to present them as function of frequency and location in a condensed statistical form.

The theory for the internal induction process shows that inducing and induced fields above a conductive substratum supplement each other in the horizontal components, but oppose each other in the vertical components. Thus, we obtain a nearly tangential variation field under "normal" conditions, i.e., in the absence of lateral conductivity gradients, provided that the overall depth of the eddy currents is small in comparison to the dimensions of the primary field (cf. eq. 3.2).

Consequently, internal conductivity anomalies, which disturb locally this sensitive balance between external and internal Z-variations, are more obvious in Z than in H and D, where the anomalous parts are superimposed upon substantial normal parts. Nevertheless, we shall study the anomalous behavior in all three components, since this provides us with an effective control for the presumed internal origin of the anomalies.

The analysis of the magnetograms is directed toward a statistical correlation between anomalous and normal parts of outstanding magnetic disturbances, using events of the same general type (e.g., bays), but of different form and intensity. This postulated correlation is necessarily linear as is readily seen from the governing equations in section 1.2 which establish linear relations for the transient magnetic field vector $\mathbf{F}$.

We obtain in this way for each survey station a 3 x 3 matrix of transfer functions, connecting the components of the anomalous ($\mathbf{F}_a$) and normal ($\bar{\mathbf{F}}$) disturbance vector at that site in the frequency domain (eq. 3.11). These transfer functions give the proper statistical basis for the subsequent interpretation of the induction anomaly in terms of internal conductivity structures.

Strictly speaking, some regard should be given to the nature of the primary inducing field from above, i.e., to its spatial configuration. We may disregard, however, this complication when dealing with the smooth mid-latitude field of bays and similar events. Their depth of penetration into the earth is, as a rule, small in comparison to their spatial nonuniformity. As a consequence, the downward attenuation of $\bar{\mathbf{F}}$ and thereby the correlation between $\mathbf{F}_a$ and $\bar{\mathbf{F}}$ are independent of the "wave number" of the incident variation field as is evident from the pertinent relations of sections 5.2 and 5.3.

It remains to verify the truly internal origin of the induction anomaly which these transfer functions describe in a normalized form. To this end we apply separation methods to their spatial distribution for each resolved frequency component, thereby eliminating unwanted contaminations of external origin.

In summary, the successive steps of the data reduction are (a) digitalization of the magnetograms within selected time intervals, (b) separation of anomalous and normal parts of the observed variations, (c) cross correlation between the anomalous and normal parts in the frequency domain, (d) separation of external and internal parts of the thus normalized anomalous part.

3.2 Selection of Time Intervals for Analysis

Three months of field operations with six Askanias gave about sixty days of usable simultaneous records from all stations. From these eight quiet days were chosen for the study of the slow diurnal variations and about thirty hours of vigorous magnetic activity for the analysis of fast variations. We can choose here between isolated events of short duration and long-lasting disturbances or storms. Plates I and II show typical examples.

Single events, in particular so-called bays, provide an excellent signal which clearly stands out from the general background activity of quiet nights, even though it contains only few usable frequencies. Numerous events in various frequency groups can be evaluated without involving an unreasonable amount of scaling. Storms permit us to analyze a wide frequency range concurrently, but the overhead storm field is of greater complexity than the smooth field of bays in mid-latitudes. This impairs the proper identification and analysis of induction anomalies. Furthermore, suitable storms of moderate intensity are rare events and the chance to record one successfully at all survey stations is not very large.

In short, the forthcoming deductions are derived primarily from the anomalous behavior of single events. In one instance thus obtained results were checked against those from a magnetic storm and found to be comparable (fig. 23).

3.3 Scaling and Scaling Errors

The traces in D, H and Z have been scaled either on photographic prints, 12-fold enlarged from the 16 mm film, or with the aid of a Kodagraph microfilm reader with a 20-fold magnification. For prints the resulting time resolution was 1 min/mm and the scale values were roughly 3γ/mm in D and H, 1.5γ/mm in Z. Individual readings of the traces relative to the base line were made at fixed time intervals as described in sections 3.6 and 3.7.

We distinguish three types of scaling errors: Absolute scaling errors of about ±1 mm are due to the blurred images of the traces; relative scaling errors of about 2% reflect the uncertainty of the scale value determination; and timing errors of about ±1 min arise from faulty clock corrections and the irregular film transport between hour marks (sec. 2.4). Since timing errors impair severely the important synchronization of magnetograms from different sites, spikes in the D- and H-traces were used as additional time references. We may assume safely that they occurred simultaneously at all field stations.

3.4 Separation of Anomalous and Normal Parts

A precise distinction between the anomalous and normal parts of the observed variations is not possible, since it would require a detailed knowledge of the large-scale variation field outside of the surveyed area. The following method represents a reasonable compromise. It is simple enough to allow a straightforward application but it gives nevertheless some regard to the spatial nonuniformity of the primary field. It has been developed mainly in view of the mid-latitude field of bays and storm-time variations.

Suppose a line or net of temporary magnetic stations has recorded successfully a series of suitable magnetic disturbances and a pilot study (cf. sec. 3.13) were established, where local anomalies occur and which trend they have; considering first variations in H and D we can find their normal parts (a) by smoothing out spatial differences within the surveyed area, or (b) by declaring one station at a distance from marked anomalies as reference station. The horizontal variations as recorded at that site are considered to be "normal" for the area under consideration. Preference has been given to the second method.

Let the center of the surveyed area or the reference station be at the origin of rectangular coordinates, x toward magnetic north and y toward magnetic east. Using an expansion by Taylor's series the normal horizontal variations at the location P(x, y) are then derived from

$$\begin{aligned} \overline{H}(x, y) &= \overline{H}(0, 0) + \overline{H}_x x + \overline{H}_y y \\ \overline{D}(x, y) &= \overline{D}(0, 0) + \overline{D}_x x + \overline{D}_y y \end{aligned} \tag{3.1}$$

where $\overline{H}_x = \partial\overline{H}/\partial x \ldots$ denote the spatial gradients. These gradients are estimated with the aid of distant permanent observatories, say, 500 to 1000 km away from the survey. Notice that the gradients $\overline{H}_y$ and $\overline{D}_x$ are equal, since the variation field above the ground should be irrotational.

The associate normal part in Z is not arbitrary but given by the spatial nonuniformity of the primary field in relation to its depth of penetration. Hence, in the case of short-period variations they are relatively small and not easily recognized as such in the presence of substantial anomalies.

We shall use here the approximation

$$\overline{Z} = c \cdot (\overline{H}_x + \overline{D}_y) \tag{3.2}$$

from section 5.5, where c is a frequency-dependent, complex-valued measure for the mean depth of penetration of the incident field. Its numerical value has to be inferred on the basis of a preconceived normal conductivity distribution as function of depth. Notice that $\overline{Z}$ is treated as uniform within the surveyed area, since its spatial gradients would be proportional to the second derivatives of H and D.

The anomalous parts in H, D, and Z are obtained by subtracting the thus defined normal parts from the observed variations. Substantial changes of the compass deviation within the surveyed area may require that the observed horizontal variations are translated first to mean magnetic coordinates.

This separation method of anomalous and normal parts can be applied either to instant values of the variations or to their Fourier transforms and spectra (secs. 3.6 and 3.7). Both possibilities have their shortcomings. In the first case we have to adopt some average value for c in accordance with the expected frequency content of the analyzed disturbance, in the second case we have to assume that the same gradients prevail over the full length of the analyzed interval, a restrictive assumption during storms.

The observatory at Tucson, Arizona, was the only permanent observatory which could be used during the survey. Therefore, the spatial gradients of the analyzed events remained largely unknown except for some general features which are mentioned in section 7.1. It may suffice to remark that the normal part in Z is here small in comparison to the normal parts of the horizontal variations. The gradients of $\overline{H}$ and $\overline{D}$ in (3.1) could be disregarded, since the profiles of survey stations ran usually about east-west, i.e., perpendicular to the predominant north-south gradient of bays and similar disturbances.

3.5 Power and Cross Spectra

Suppose a time function Z(t) is linearly related to a second time function H(t), both being normalized to zero mean value for a given interval $-\frac{1}{2}T_0 \leq t \leq +\frac{1}{2}T_0$. Their relation shall be independent of time within this interval and therefore expressible by a linear transfer function $z_H(f)$ in the frequency domain, assuming that $T_0 \rightarrow \infty$. Denoting the Fourier transform of X(t) with

$$C_X(f) = \int_{-\infty}^{+\infty} X(t) e^{-2\pi i f t} dt \tag{3.3}$$

we may set

$$C_Z(f) = z_H(f) \cdot C_H(f). \tag{3.4}$$

The product of C_H with its complex conjugate transform C_H^* is real and represents, when divided by T_0, the power spectrum S_H of H(t), defined as limiting value for $T_0 \rightarrow \infty$. The product of C_Z with C_H^* yields in a similar way the cross spectrum between Z(t) and H(t):

$$\begin{aligned} S_H &= (C_H C_H^*)/T_o \\ S_{ZH} &= S_{HZ}^* = (C_Z \cdot C_H^*)/T_o \\ z_H &= S_{ZH}/S_H \,. \end{aligned} \qquad (3.5)$$

Notice that T_o drops out of the last equation which expresses the transfer function in terms of power and cross spectra.

Suppose $Z(t)$ contains some unrelated "noise" $\delta Z(t)$. Its power is given evidently by

$$S_{\delta Z} = S_Z - |S_{ZH}|^2/S_H$$

since $|z_H \cdot C_H|^2$ is the power of the related portion of $Z(t)$. The square root of the normalized related power $(S_Z - S_{\delta Z})/S_Z$ is commonly referred to as "coherence" Co(f) between $Z(t)$ and $H(t)$, while the square root of the normalized unrelated power $S_{\delta Z}/S_Z$ shall be denoted as "residual" $\epsilon(f)$:

$$C_o^2 = 1 - \epsilon^2 = |S_{ZH}|^2/(S_Z \cdot S_H) \,. \qquad (3.6)$$

The coherence varies between zero in the case of no correlation for a certain frequency component and unity in the case of a one-to-one relationship. Spectra of empirical time series are determined necessarily with some inaccuracy, since they have to be derived from digitized or analog records of finite length. This may simulate a nonexisting coherence which scatters around a mean value of $\sqrt{2/\nu}$ for unrelated records, ν denoting the degrees of freedom of the analysis. As a rule, Co(f) should exceed $\sqrt{4/\nu}$ to imply a significant dependence of $Z(t)$ from $H(t)$ for a given frequency.

There are two possibilities to derive spectral values with more than one degree of freedom: (a) by averaging the spectra of N short intervals, or (b) by smoothing the spectrum of one long interval T_o within frequency bands of the width Δf. In the first case we have $2(N - 1)$ degrees of freedom, in the second case $2\,\Delta f\, T_o$, since T_o^{-1} would be the ultimate frequency spacing of standard harmonic coefficients. The factor 2 reflects in either case the use of sine and cosine terms for the calculation of spectral values (cf. eq. 3.10).

3.6 Spectral Analysis of Single Events

Most conspicuous are bay-shaped deflections during the night hours, which occur a few times each month and last for about two hours (Pl. I). Similar events of shorter duration appear from time to time as "sudden impetus," "sudden storm commencement," or fast daytime fluctuations in general. Even though these events are nonperiodic time functions, we can use a standard harmonic analysis for their representation in the frequency domain.

At the outset a time interval of the length T_o is chosen equal to or a bit longer than the duration of the disturbance and the traces are scaled within this interval. After some preliminary tests it was decided to scale bays every five minutes over two hours and fast fluctuations every 1-1/4 minute over one-half hour, yielding in either case 25 values for each component and station.

The long-periodic trend is removed by subtracting from the scaled values H_j corresponding values of an analytic time function $H'(t)$ which resembles the smoothed trace before and after the chosen interval. Appendix I gives two appropriate trend functions. The traces shall coincide with $H'(t)$ at the beginning and end of the interval, yielding $H_j - H'(t) = 0$ for $j = 1$ and $j = 25$. The differences $H_j - H(t)$ are now harmonically analyzed up to the 4th subharmonic with $f_o = T_o^{-1}$ as fundamental frequency. It will be seen that the arbitrary choice of f_o is not prejudicial to the kind of correlation analysis intended here.

The single event is expressed in this way by a series of chopped-off harmonic oscillations

$$H(t) = H'(t) + \begin{cases} \frac{1}{2} H_o + \sum\limits_{n=1}^{4} \left[H_{n,u} + iH_{n,v}\right] \exp(i2\pi nt/T_o) & |t| \le \frac{1}{2} T_o \\ \\ 0 & |t| \ge \frac{1}{2} T_o \, . \end{cases} \tag{3.7}$$

By taking the real part of the right-hand side $H_{n,u}$ becomes the cosine coefficient and $H_{n,v}$ the negative sine coefficient of the n^{th} subharmonic. Their frequencies range from 0.5 to 2.0 cph in the case of bays and from 2 to 8 cph in the case of fast variations. The overlap at 2 cph provides an effective control for the consistency of any results in the two groups.

We apply a Fourier transformation to (3.7) and obtain

$$C_H(f) = C_{H'}(f) + T_o \sum_{-4}^{4} c_n \frac{\sin[(fT_o + n)\pi]}{(fT_o + n)\, 2\pi} \tag{3.8}$$

$$c_n = \begin{cases} H_{n,u} - iH_{n,v} & n > 0 \\ H_o & n = 0 \\ H_{n,u} + iH_{n,v} & n < 0 \end{cases}$$

with $C_{H'}$ as transform of the trend $H'(t)$. In particular, for those frequencies which are multiple of f_o we obtain

$$C_H(nf_o) = \frac{1}{2} T_o (H_{n,u} + iH_{n,v}) + C_{H'}(nf_o). \tag{3.9}$$

Hence, harmonic coefficients, multiplied by $T_o/2$ and corrected for the trend, are indeed fair estimates of the true cosine and sine transforms, provided that these transforms are not very rugged frequency functions within the bands $(nf_o \pm \frac{1}{2} f_o)$. Already the smooth appearance of single events leads us to expect that their transforms meet this requirement as demonstrated for a typical bay in figure 3.

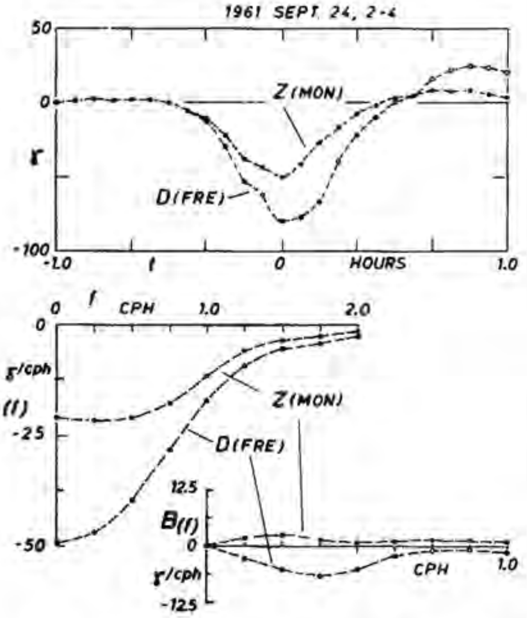

Fig. 3. Typical bay and its Fourier transforms, derived according to (3.8) from the first four harmonic coefficients of the shown time interval. A(f): cosine transform, B(f): negative sine transform. Remarkable smoothness of the transforms and consistent relation between the Z-transforms at the coastal station Monterey and the D-transforms at the inland station Fresno. Notice phase lead of Z(MON) relative to D(FRE) (cf. fig. 16 and tab. 8 Z).

The harmonics of the same frequency are combined to cross and power spectral values according to (3.5) and averaged (< >) over an assemblage of events. Omitting the corrections for the trend we obtain from (3.9)

$$
\begin{aligned}
S_{ZH}(nf_o) &= \frac{1}{4} T_o [< H_{n,u} Z_{n,u} + H_{n,v} Z_{n,v} > + i < H_{n,u} Z_{n,v} - H_{n,v} Z_{n,u} >] \\
S_H(nf_o) &= \frac{1}{4} T_o < H^2_{n,u} + H^2_{n,v} > . \qquad (3.10)
\end{aligned}
$$

3.7 Spectra of Storms

Corresponding spectral values of magnetic storms have been derived not from the original time functions, say, H(t) and Z(t), themselves, but from condensed lag functions to ensure an adequate smoothing of the spectra according to Tukey's method. The lag function for the cross spectrum S_{ZH}, for instance, is defined as the limiting value of

$$R_{ZH}(\tau) = \frac{1}{T_o} \int_{-T_o/2}^{T_o/2} Z(t)\, H(t-\tau)\, dt$$

for $T_o \to \infty$. Its Fourier transform would be the true spectrum S_{ZH} from

(3.5). Since the available interval T_o is always finite, we evaluate the integral only for a limited lag range $|\tau| \leq T_m \ll T_o$ and multiply the resulting lag function with a lag window which is zero for $|\tau| > T_m$. The transform of the product represents a smoothed estimate of the cross spectrum S_{ZH} with $\Delta f = T_m^{-1}$ as effective bandwidth in the case of Tukey's lag window (cf. Munk, Snodgrass, and Tucker, 1959; sec. 3.1).

A moderate storm, of which a section is shown in Pl. II, has been analyzed as follows: Readings were made every $\Delta t = 2\text{-}1/2$ minutes over $T_o = 12$ hours, yielding $N = 288$ individual values for each component and station. Auto and cross correlograms were determined with 24 discrete lags τ, ranging from zero to $T_m = 1$ hour. This maximum lag seemed to be a reasonable compromise between sufficient degrees of freedom ($\nu = 24$) and an adequate spacing of the spectral estimates, given by $(2T_m)^{-1} = 0.5$ cph.

Thus, spectral values were obtained for frequencies ranging from $f = 0$ to 12 cph and a coherence greater than $(4/24)^{1/2} = 0.41$ would be indicative of a meaningful relation between records. The lag functions have not been derived from the original series, say, H(t), themselves, but from the differences $H'(t) = H(t + \Delta t) - H(t)$, normalized to zero mean value. This favors the high-frequency portion of the spectra, since the power spectrum of H'(t) equals $2[1 - \cos(\omega \Delta t)]\, S_H$, i.e., $S_{H'}$ equals zero for $f = 0$ and $4 S_H$ for $f =$ 12 cph.

3.8 Correlation Analysis between Anomalous and Normal Parts (Transfer Functions)

Let $H_a(t)$, $D_a(t)$, $Z_a(t)$ be the anomalous parts of the observed H-, D-, and Z-variations during one particular event as observed at a certain site. After applying a Fourier transformation we express their linear relation to the normal parts $\overline{H}(t)$, $\overline{D}(t)$, $\overline{Z}(t)$ by a matrix of transfer functions (cf. eq. 3.5):

$$\begin{pmatrix} C_{H_a} \\ C_{D_a} \\ C_{Z_a} \end{pmatrix} = \begin{pmatrix} h_H & h_D & h_Z \\ d_H & d_D & d_Z \\ z_H & z_D & z_Z \end{pmatrix} \begin{pmatrix} C_{\overline{H}} \\ C_{\overline{D}} \\ C_{\overline{Z}} \end{pmatrix} + \begin{pmatrix} C_{\delta H} \\ C_{\delta D} \\ C_{\delta Z} \end{pmatrix} \tag{3.11}$$

The last column contains the transforms of the uncorrelated portions $\delta H(t)$, $\delta D(t)$, $\delta Z(t)$ for each component. The matrix of transfer functions has to be determined in such a way that the unrelated powers $S_{\delta H}(f)$ ... are at a minimum for each resolved frequency component, when averaged over an assemblage or a sequence of events.

We note that these transfer functions are complex-valued frequency functions of the form

$$z_H = z_H(u) + i z_H(v) \tag{3.12}$$

with $z_H(u)$ as in-phase transfer and $z_H(v)$ as out-of-phase transfer between

Z_a and $\overline{H}$. Since $\exp(+i\omega t)$ is time factor throughout this presentation, the phase lead of Z_a relative to $\overline{H}$ for a given frequency is $\tan^{-1}[z_H(v)/z_H(u)]$. Let us write (3.11) explicitly for the anomalous part of one particular component, say, for Z_a:

$$C_{Z_a} = z_H C_{\overline{H}} + z_D C_{\overline{D}} + z_Z C_{\overline{Z}} + C_{\delta Z}. \tag{3.13}$$

The minimum condition requires that the derivatives

$$\partial S_{\delta Z}/\partial z_H(u) = -[C_{\delta Z} C^*_{\overline{H}} + C^*_{\delta Z} C_{\overline{H}}]$$

$$\partial S_{\delta Z}/\partial z_H(v) = i\,[C_{\delta Z} C^*_{\overline{H}} - C^*_{\delta Z} C_{\overline{H}}],$$

etc., disappear. We see that the condition is satisfied when the cross spectra between $\delta Z(t)$ and the normal parts $\overline{H}(t)$ ... vanish:

$$S_{\delta Z\overline{H}} = S_{\delta Z\overline{D}} = S_{\delta Z\overline{Z}} = 0. \tag{3.14}$$

We substitute $C_{\delta Z}$ from (3.13), replace the resulting products of transforms by cross and power spectra in accordance with (3.5), and obtain after dropping the common time factor T_o the following system of linear equations:

$$\begin{aligned}
z_H S_{\overline{H}} + z_D S_{\overline{D}\overline{H}} + z_Z S_{\overline{Z}\overline{H}} &= S_{Z_a\overline{H}}\\
z_H S_{\overline{H}\overline{D}} + z_D S_{\overline{D}} + z_Z S_{\overline{Z}\overline{D}} &= S_{Z_a\overline{D}}\\
z_H S_{\overline{H}\overline{Z}} + z_D S_{\overline{D}\overline{Z}} + z_Z S_{\overline{Z}} &= S_{Z_a\overline{Z}}.
\end{aligned} \tag{3.15}$$

It remains to insert the averaged spectra of numerous isolated events or the smoothed spectra of a single storm and to determine the unknown transfer functions $z_H(f)$, $z_D(f)$, $z_Z(f)$ by matrix inversion. An explicit solution can be found in section 3.11, referring to the special case of unrelated small normal Z-variations.

The transfer functions h_H, h_D, h_Z and d_H, d_D, d_Z are obtained in a similar way by replacing in (3.15) the cross spectra containing Z_a by those containing H_a and D_a, respectively. We observe that these basic relations contain, as they should, the cross spectra between anomalous and normal parts in all possible combinations, but they involve also the cross spectra between the normal components alone to take their coherence into account. If $\overline{D}$, $\overline{H}$, and $\overline{Z}$ were completely unrelated, we could set in (3.15) their cross spectra, e.g., $S_{\overline{D}\overline{H}}$, to zero, yielding $z_H = S_{Z_a\overline{H}}/S_{\overline{H}}$, etc., as in (3.5).

3.9 Residuals

The statistical significance of the thus established correlation between anomalous and normal parts depends (a) on the relative amount of related power in each component, and (b) on the degrees of freedom with which the spectra have been obtained. Considering again first the anomalous part in Z we define

$$\epsilon_Z(f) = [S_{\delta Z}(f)/S_{Z_a}(f)]^{1/2} \tag{3.16}$$

as normalized residual in Z to indicate the percentage of unrelated anomalous power in that component. For $S_{\delta Z}$ we can write

$$C_{\delta Z}(C^*_{Z_a} - z^*_H C^*_{\bar{H}} - z^*_D C^*_{\bar{D}} - z_Z C^*_{\bar{Z}})$$

when the complex conjugate $C^*_{\delta Z}$ is deduced from (3.13). All products on the right-hand side are zero except the first one in virtue of the minimum conditions (3.14), yielding

$$S_{\delta Z} = C_{\delta Z} C^*_{Z_a}$$

Substituting $C_{\delta Z}$ from (3.13) and dividing both sides by the total power of Z_a gives

$$\epsilon_Z = [1 - (z_H S_{\bar{H}Z_a} + z_D S_{\bar{D}Z_a} + z_Z S_{\bar{Z}Z_a})/S_{Z_a}]^{1/2}. \tag{3.17}$$

The fraction under the square root is real and positive, being smaller than or equal to unity.

This formula and the corresponding relations for H_a and D_a permit us to derive the residuals ϵ_D, ϵ_H, ϵ_Z with the aid of the transfer functions without actual calculation of the unrelated power spectra. Suppose the spectra appearing in the basic equations (3.15) have been derived by averaging over the spectra of N isolated events, as is usually the case here. Evidently $N = 3$ events would determine the transfer functions uniquely with zero residuals, i.e., with zero degrees of freedom. Each additional event adds with its sine and cosine transforms two degrees of freedom, hence $\nu = 2(N - 3)$.

According to the rule cited in section 3.5 the residual should not exceed $\sqrt{1 - 4/\nu}$ as upper permissible limit to imply a meaningful coherence for one particular frequency. This establishes in analogy

$$[(N - 5)/(N - 3)]^{1/2} \tag{3.18}$$

as upper limit for the residuals. It is presumed of course that N is sufficiently large, in particular larger than 5.

3.10 Induction and Perturbation Arrows

Parkinson (1959) and Wiese (1962) introduced a convenient arrow presentation to indicate the magnitude of (anomalous) Z-variations in dependence of the strength and orientation of the horizontal disturbance vector at the same location. They did not distinguish between anomalous and normal parts in the strict sense and evaluated pronounced disturbances regardless of time lags between maximum deflections in the three components. Their approach proved to be very successful, in particular with regard to outlining the trend of induction anomalies and we shall introduce a similar arrow presentation for the transfer functions.

Let $\mathbf{i}$, $\mathbf{j}$ be Cartesian unit vectors toward magnetic north and magnetic east at a given survey station. Beginning with the transfer functions of Z_a we define as induction arrows for one particular frequency

$$\begin{aligned} \mathbf{c}_u &= -z_H(u)\,\mathbf{i} - z_D(u)\,\mathbf{j} \qquad &\text{(in-phase arrow)} \\ \mathbf{c}_v &= +z_H(v)\,\mathbf{i} + z_D(v)\,\mathbf{j} \qquad &\text{(out-of-phase arrow)} \end{aligned} \tag{3.19}$$

as shown in figure 4. Maximum in-phase and out-of-phase anomalous Z-variations (as far as they are related to $\overline{H}$ and $\overline{D}$) occur when the normal horizontal disturbance vector is linearly polarized in the direction of $-\mathbf{c}_u$, respectively $\mathbf{c}_v$. (The negative orientation of the in-phase arrow has been chosen in accordance with the orientation of Parkinson's arrow.) The degree of statistical significance can be indicated by a circle of confidence of the radius

$$\epsilon_Z[\,|c_u|^2 + |c_v|^2]^{1/2}, \tag{3.20}$$

representing the relative amplitude of unrelated anomalous Z-variations.

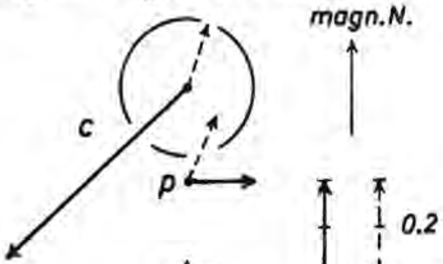

Fig. 4. Induction and perturbation arrows for the survey station Half Moon Bay south of San Francisco at 1 cph (cf. transfer values in tab. 8).

The visual display of these arrows in maps offers a comprehensive view of the changing anomalous behavior of Z-variations as function of frequency and location. In-phase arrows point toward zones of high and away from zones of low internal conductivity. Substantial out-of-phase arrows in the opposite direction suggest that near-surface conductivity anomalies are involved, since superficial eddy currents have a marked phase lead relative to $\overline{H}$ and $\overline{D}$ around 1 cph and the same would apply to any anomalies connected with them.

The transfer functions pertaining to H_a and D_a are combined columnwise to perturbation arrows (fig. 4),

$$\begin{aligned} \mathbf{p} &= h_H\mathbf{i} + d_H\mathbf{j} \\ \mathbf{q} &= h_D\mathbf{i} + d_D\mathbf{j} \end{aligned} \tag{3.21}$$

inserting again either the in-phase or the out-of-phase transfers. These arrows, when rotated counterclockwise by 90°, indicate strength and direction of the anomalous internal current field which is superimposed upon the westward ($\mathbf{p}$), respectively northward ($\mathbf{q}$), flow of unperturbed normal currents.

The transfer functions of the last column (h_Z, d_Z, z_Z) have been excluded from the arrow presentation. They refer to induction anomalies of the 2nd kind (sec. 6.2) due to local induction by $\overline{Z}$ within the anomalous zone and are of minor importance in mid-latitudes.

3.11 Special Case I: Unrelated Normal Z-variations

The mid-latitude bay field has relatively small Z-amplitudes under normal internal conditions and we may assume that negligible correlation exists between $\overline{Z}$ and the components of the anomalous disturbance vector $\mathbf{F}_a$ (exclusion of induction anomalies of the 2nd kind, sec. 6.2). Let us further assume that any normal part in Z has zero coherence with the normal parts in H and D, i.e., the lateral gradients of the primary field shall vary at random among the analyzed events (eq. 3.2).

Under these conditions all cross spectra containing $\overline{Z}$ vanish and the matrix inversion of (3.15) yields the simple relations

$$z_H = \frac{S_{Z\overline{H}}\, S_{\overline{D}} - S_{Z\overline{D}}\, S_{\overline{D}\overline{H}}}{S_{\overline{H}}\, S_{\overline{D}} - |S_{\overline{D}\overline{H}}|^2}$$

$$z_D = \frac{S_{Z\overline{D}}\, S_{\overline{H}} - S_{Z\overline{H}}\, S_{\overline{H}\overline{D}}}{S_{\overline{H}}\, S_{\overline{D}} - |S_{\overline{D}\overline{H}}|^2} \qquad (3.22)$$

with $z_Z = 0$ by definition. Notice that the cross spectra with the anomalous part Z_a may be replaced by those pertaining to the observed Z-variations, since $S_{Z_a\overline{H}}$ equals $S_{Z\overline{H}} - S_{\overline{Z}\overline{H}}$ and thereby $S_{Z\overline{H}}$.

If $\overline{H}$ and $\overline{D}$ have a one-to-one relationship (polarization of the normal disturbance vector in a fixed direction), then $S_{\overline{D}} \cdot S_{\overline{H}} = |S_{\overline{H}\overline{D}}|^2$ in virtue of (3.6) and the transfer functions z_H and z_D become infinite, as they should. Thus, a certain randomness of the D:H ratio should prevail among the analyzed events. The degrees of freedom are here $2(N - 2)$ in the case of N single events, which establishes

$$[(N - 4)/(N - 2)]^{1/2} \qquad (3.23)$$

as upper permissible residual in lieu of equation 3.18.

The remaining pairs of transfer functions, pertaining to $H_a(h_H, h_D)$ and $D_a(d_H, d_D)$ can be obtained from corresponding expressions, inserting in (3.22) the cross spectra with H_a and D_a, respectively.

3.12 Special Case II: Elongated Anomalies

Consider a 2-dimensional internal conductivity structure which strikes with an angle β against magnetic north, counting β positive from north over east.

The resulting induction anomaly of transient variations will be likewise 2-dimensional, i.e., the anomalous disturbance vector $\mathbf{F}_a$ will be confined to a vertical plane perpendicular to the trend of the conductivity structure. We project therefore the horizontal disturbance vector on the direction $(\pi/2 + \beta)$, denote the projection as

$$B = -H\sin\beta + D\cos\beta,$$

and write for (3.11)

$$\begin{pmatrix} C_{B_a} \\ C_{Z_a} \end{pmatrix} = \begin{pmatrix} b_B & b_Z \\ z_B & z_Z \end{pmatrix} \begin{pmatrix} C_{\overline{B}} \\ C_{\overline{Z}} \end{pmatrix} + \begin{pmatrix} C_{\delta B} \\ C_{\delta Z} \end{pmatrix}. \qquad (3.24)$$

Since $H_a\cos\beta + D_a\sin\beta = 0$, we have $h_H/d_H = h_D/d_D = z_H/z_D = -\tan\beta$, i.e., the induction and perturbation arrows of section 3.10 are oriented at right angles to the trend. It is readily verified that the 2-dimensional transfer functions in (3.24) are related to those in (3.11) according to

$$\begin{pmatrix} b_B & b_Z \\ z_B & z_Z \end{pmatrix} = \begin{pmatrix} h_H + d_D & -h_Z\sin\beta + d_Z\cos\beta \\ -z_H\sin\beta + z_D\cos\beta & z_Z \end{pmatrix}. \qquad (3.25)$$

In reality an internal conductivity structure might be an elongated feature, and the induction and perturbation arrows may scatter closely around a certain mean direction $(\pi/2 + \overline{\beta})$, as for instance in figure 19. In that case we project the horizontal disturbance vector and the transfer functions on this mean direction as in (3.24, 25), but give the resulting 2-dimensional transfer functions the index "p", e.g.,

$$z_P = -z_H\sin\overline{\beta} + z_D\cos\overline{\beta}. \qquad (3.26a)$$

Some precaution is needed in the case of the transfer function, connecting B_a and $\overline{B}$. Let

$$\delta = \tan^{-1}(d_H/h_H) - \tan^{-1}(d_D/h_D)$$

denote the angle, formed by the perturbation arrows **p** and **q**. By setting $\sin\delta \approx \delta$ and $\cos\delta \approx 1$ we obtain the conversion formula

$$h_P = (h_H + d_D)\,(1 + \frac{1}{2}\delta\,\sin 2\beta), \qquad (3.26b)$$

writing h_P in place of b_P. Profiles of z_P and h_P, when shown for various different frequencies as in figure 10, provide us with comprehensive cross sections through anomalous zones.

3.13 Special Case III: Pilot Study

The numerical evaluation of the basic equations (3.15) or (3.22) is quite elaborate, requires a large amount of well-prepared data, and has to be done with high-speed computers (cf. program GMV, App. IV). It is often desirable to begin the data reduction with a simple preliminary analysis while the field operations are still in progress. This may help to add new field stations in the most effective way within anomalous zones.

Parkinson (1959) and Wiese (1962) described suitable graphical methods to treat peak-value readings from numerous single events, yielding length and direction of the (in-phase) induction arrows. Untiedt's method (1964), which is now widely accepted, results in comparable arrows but employs continuous readings from a few outstanding disturbances. The method presented here is analytic on the basis of a least-square fit and follows directly from equation 3.22 in section 3.11. Let H, D, Z be the amplitudes of quasi-sinusoidal disturbances, observed simultaneously at one particular site. Maximum deflections in the three components may not coincide exactly in time, but such phase shifts are disregarded. Hence, the products

$$< H \cdot D > = \overline{HD}$$

when averaged over numerous events of the same quasi-period, shall represent the now real cross spectrum between H and D. We ignore the anomalous parts in H and D and rewrite equation 3.22 in the form

$$z_H = \frac{\overline{ZH}\,\overline{DD} - \overline{ZD}\,\overline{HD}}{\overline{DD}\,\overline{HH} - \overline{HD}^2}$$
$$z_D = \frac{\overline{ZD}\,\overline{HH} - \overline{ZH}\,\overline{HD}}{\overline{DD}\,\overline{HH} - \overline{HD}^2} \qquad (3.27)$$

with

$$\epsilon_Z = [\,1 - (z_H\,\overline{ZH} + z_D\,\overline{ZD})/\overline{ZZ}\,]^{1/2}$$

as residual of the correlation analysis (from eq. 3.17). Thus determined "peak-value" transfer functions can be put together to preliminary (in-phase) induction arrows (eq. 3.19) with a corresponding circle of confidence (eq. 3.20) for various quasi-periods.

3.14 Contribution of Scaling Errors to Residuals

Consistent scaling errors, arising for instance from calibration errors or from wrong clock corrections, are undetectable in the course of the data reduction and should be kept to a minimum. Random scaling errors, on the other hand, augment the residuals of the correlation analysis (cf. sec. 3.9). Their contributions are denoted as "error residuals" to distinguish them from those which reflect a genuine lack of correlation between the anomalous and normal parts.

Let α and β be estimates of the mean relative scaling error and the timing error, respectively, both varying at random within the assemblage or sequence of analyzed events (cf. sec. 3.3). In the frequency domain α becomes the proportional amplitude error of the transforms and β the phase error $\phi = 2\pi f\beta$ for each resolved frequency component f. Let $\tilde{C}_H$ be the true transform of H(t), for instance, and therefore

$$C_H = \tilde{C}_H(1 \pm \alpha) \exp(\pm i\phi)$$

its empirical value. Rewriting (3.13) in this form gives with $\exp(i\phi) \approx 1 + i\phi$ and $z_Z = 0$

$$\tilde{C}_{Z_a}(1 \pm \alpha \pm i\phi) = (z_H \cdot \tilde{C}_{\overline{H}} + z_D \cdot \tilde{C}_{\overline{D}})(1 \mp \alpha) + C_{\delta Z} \qquad (3.28)$$

when the sign of α is chosen so as to yield the worst possible error combination. The phase errors of $C_{\overline{H}}$ and $C_{\overline{D}}$ are omitted, since we assume that $\overline{H}$ and $\overline{D}$ have been scaled in perfect synchronization on the magnetogram of a reference station, leaving only the relative phase error of C_{Z_a} to be considered.

We presume that the unrelated portion δZ is entirely due to scaling errors, hence

$$\tilde{C}_{Z_a} = z_H \cdot \tilde{C}_{\overline{H}} + z_D \cdot \tilde{C}_{\overline{D}}$$

which when inserted in (3.28) yields in virtue of (3.16)

$$\epsilon_Z = 2 \cdot [\alpha^2 + (\pi f\beta)^2]^{1/2} \qquad (3.29)$$

as error residual in Z.

Turning to the corresponding error residuals in H and D we observe that H_a and D_a represent minor differences between the observed H- and D-variations and their normal parts as recorded at the pertinent reference station. In the case of the anomalous part in H, for instance, we have in place of (3.28) the more complicated expression

$$\tilde{C}_H(1 \pm \alpha \pm i\phi) - \tilde{C}_{\overline{H}}(1 \mp \alpha) = (h_H \cdot \tilde{C}_{\overline{H}} + h_D \cdot \tilde{C}_{\overline{D}})(1 \mp \alpha) + C_{\delta H}$$

which reduces in a similar way to

$$\epsilon_H = 2 \cdot \left\{[\alpha^2 + (\pi f\beta)^2] \cdot S_H/S_{H_a}\right\}^{1/2}. \qquad (3.30)$$

Since the total power in H and D is as a rule several times larger than the power of their anomalous parts, we have to expect substantial error residuals in H and D, even when the scaling errors are quite small.

Reasonable estimates for α and β are 0.02 and 1 min, respectively. The resulting error residuals in Z are given in table 1, illustrating the severe effect of timing errors. (α alone would have given only $\epsilon_Z = 0.04$ at all frequencies.) A comparison with the residuals of the actual data reduction in tables 5 to 10 shows that they are well within the range of the expected error residuals. Hence, the attainable degree of correlation between the anomalous and normal parts seems to be limited by timing errors and any improvements would require in the first place a better synchronization of scalings from different sites.

3.15 Examples for Correlated Z-variations

The residuals ϵ_D, ϵ_H, ϵ_Z of section 3.9 indicate the average degree of correlation between the anomalous and normal parts of the observed variations at a given site. Let us now examine their correlation in a few individual cases.

Once the matrix of transfer functions has been determined we should be able to "predict" the anomalous behavior of the three components when the normal parts in D, H, and Z are given. Let $C_{\overline{H}}$ and $C_{\overline{D}}$ be their transforms of one particular event, ignoring again the presence of normal Z-variations, and let z_H and z_D be the transfer functions for Z_a at a certain survey station. Then a Fourier transformation from the frequency into the time domain, applied to $(z_H \cdot C_{\overline{H}} + z_D \cdot C_{\overline{D}})$, should yield the anomalous part $Z_a(t)$ for that station.

Figure 5 shows a comparison between thus predicted and actually observed Z-variations for a line of survey stations, using transforms and transfer functions between f = 0.5 and 2 cph. The close agreement between observed and predicted curves is convincing, in particular when we take into account that the prediction cannot produce the background trend within the selected time interval.

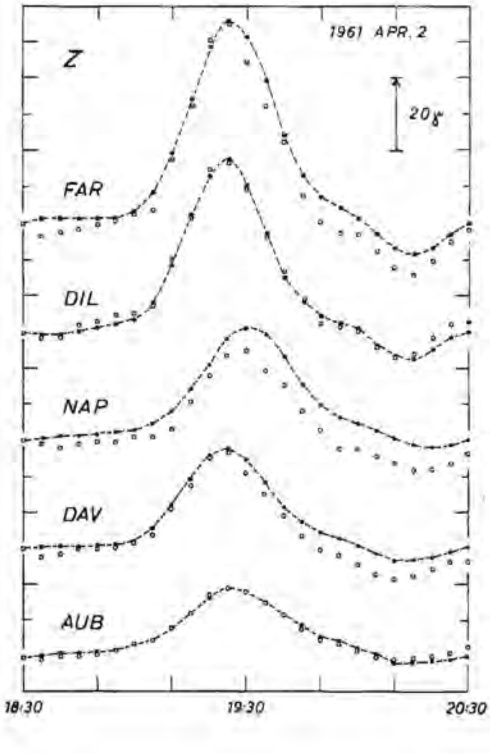

Fig. 5. Observed (dots) and calculated (open circles) Z-variations during bay for the profile Farallon Islands-Auburn in central California (see text).

A similar intercomparison for an assemblage of events (bays) is presented by the harmonic dials of figure 6. They contain as dots the complex ratio of predicted to observed Z_a-transforms for 1 cph. Their scatter is well described by circles of the radius ϵ_Z around the point of perfect correlation, even though there is a slight indication that the prediction in amplitude is better than the prediction in phase.

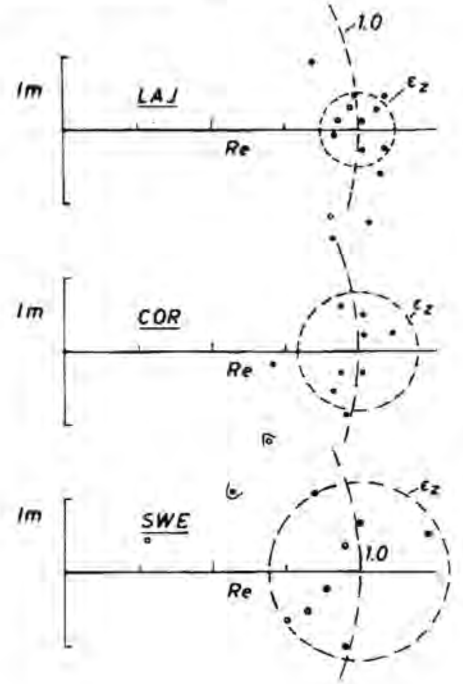

Fig. 6. Polar diagram showing the ratio of "predicted" to observed transforms of the anomalous part in Z at 1 cph. Each dot in the complex plane refers to one individual event (bay). The upper diagram represents a "good" correlation between Z_a and the normal parts in H and D ($\epsilon_Z = 0.13$, La Jolla), the central diagram an "average" degree of correlation ($\epsilon_Z = 0.21$, Comudas), and the lower diagram a "poor" correlation ($\epsilon_Z = 0.30$, Sweetwater).

3.16 Separation of Internal and External Parts

So far we have assumed tacitly that the transfer functions between anomalous and normal parts are free from inner relationships among themselves. This is not exactly true, since the magnetic field which they describe in a normalized form must be (a) curl-free and (b) of internal origin. Both requirements impose restrictions upon possible field configurations which enable us at the same time to eliminate from empirical transfer functions unrealistic and external contaminations.

In a previous publication (Schmucker, 1959) the required separation of internal and external parts of the anomalous variation field has been performed at the outset of the data reduction, using peak-value readings of single events. A corresponding separation of continuous scalings would be extremely elaborate and it is carried out preferably in the frequency domain after the completion of the correlation analysis. We may hope that the statistical treatment of numerous events minimizes random contributions of external origin to F_a.

Kertz developed a straightforward separation technique for 2-dimensional field distributions (Kertz, 1954; Siebert and Kertz, 1957; see also Price and Wilkens, 1963). Its numerical application has been thoroughly discussed by Hartmann (1963) together with an extension to 3-dimensional fields (see also Weaver, 1963). It is required of course that the anomalous field to be separated be given in its vertical and horizontal components over the full range of the anomaly.

Consider a 2-dimensional magnetic field (transient or stationary), given in the (x, z) plane of Cartesian coordinates, z down. It is presumed to be irrotational in the neighborhood of the level $z = 0$ (Earth's surface). Let $H(x)$ and $Z(x)$ be the horizontal and downward field components in that level and let K be an operator which when applied to a function $f(x)$ at the point $x = x_o$ performs the transformation

$$Kf = \frac{1}{\pi} \int_{-\infty}^{\infty} \frac{f(x)}{x_o - x}\, dx . \tag{3.31}$$

Then

$$H(x_o) = \pm KZ \text{ and } Z(x_o) = \mp KH \tag{3.32}$$

(Kertz's eq. 6, Price and Wilkens' eq. 3.31, 32). The upper signs refer to fields of external origin (sources above zero level) and the lower signs to fields of internal origin (sources below zero level). Two useful transformations in this context are

$$H(x) = I/(1 + x^2) \text{ and } KH = x_o H(x_o) \tag{3.33}$$

(line current at unit height or depth),

$$H(x) = C \exp(ikx) \text{ and } KH = - iH(x_o) \tag{3.34}$$

(sinusoidal field distribution); C may be complex and the real part is to be taken in the right-hand side of (3.34).

Let $H'(x)$ and $Z'(x)$ be a field distribution of partially external and partially internal origin. Its internal parts $H(x)$ and $Z(x)$ are readily separated, since

$$H = \frac{1}{2}(H' - KZ') \text{ and } Z = \frac{1}{2}(Z' + KH') \tag{3.35}$$

in virtue of (3.32) (Kertz's eqs. 7 and 8).

Consider a 2-dimensional induction anomaly $B_a(x, t)$, $Z_a(x, t)$ above an elongated internal conductivity structure (sec. 3.12). Because of its internal origin the relations

$$B_a = -KZ_a \qquad Z_a = +KB_a$$

must be satisfied at each instant in the time domain, and the relations

$$C_{B_a} = -KC_{Z_a} \qquad C_{Z_a} = +KC_{B_a}$$

for each frequency component in the frequency domain. If we disregard the nonuniformity of the normal part within the range of the anomaly, we may set

$$K(z_P \cdot C_{\overline{B}}) \approx C_{\overline{B}} \cdot Kz_P$$

and obtain

$$\begin{aligned} h_P &= -Kz_P \qquad & b_Z &= -Kz_Z \\ z_P &= Kh_P \qquad & z_Z &= Kb_Z \;. \end{aligned} \tag{3.36}$$

These relations express the above-mentioned interdependence of vertical and horizontal transfer functions.

Let $h'_P(x)$ and $z'_P(x)$ be the projection of empirical transfer functions on a direction which is perpendicular to the trend of an elongated anomaly. Then the truly internal parts of these projections follow from (3.35) as

$$h_P = \frac{1}{2}(h'_P - Kz'_P) \text{ and } z_P = \frac{1}{2}(z'_P + Kh'_P) \;. \tag{3.37}$$

The remaining differences $h'_P - h_P$ and $z'_P - z_P$ may be regarded as external contaminations which are removed in this way.

The numerical evaluation of the K-operator requires precaution near the singularity $x = x_o$. Hartmann (1963) was first to realize this, and his approach will be presented here in an extended form.

Let $f(x)$ be given by N discrete values, $f_1, f_2 \ldots f_N$, at the points $x = x_1$, $x_2 \ldots x_N$. These points are not necessarily equidistant and $f(x) = 0$ for $x \leq x_1$, $x \geq x_N$. We approximate $f(x)$ between adjacent values, say, f_{n+1} and f_n, by linear interpolation:

$$\begin{aligned} f(x) &= \overline{f}_n + f'_n (x - \overline{x}_n) \qquad & f'_n &= (f_{n+1} - f_n)/(x_{n+1} - x_n) \\ \overline{f}_n &= \frac{1}{2}(f_{n+1} + f_n) \qquad & \overline{x}_n &= \frac{1}{2}(x_{n+1} + x_n) \;. \end{aligned}$$

This allows us to evaluate the integral of (3.31) in closed form, if we exclude for x_o the points $x_1, x_2 \ldots x_N$.

The solution has a quite simple form when we evaluate the integral transforms at the center of each interval. Setting $x_o = \overline{x}_m$ $(m = 1, 2 \ldots N-1)$ we obtain for Kertz's operator the series

$$Kf = \frac{1}{\pi}\Big[f_m - f_{m+1} + \sum_{\substack{n=1 \\ n \neq m}}^{N-1} \Big\{ \lambda_n [\overline{f}_n + f'_n (\overline{x}_m - \overline{x}_n)] + f_n - f_{n+1} \Big\} \Big] \tag{3.38}$$

with

$$\lambda_n = \ell n \left| (\overline{x}_m - x_n)/(\overline{x}_m - x_{n+1}) \right| \;.$$

If we approximate λ_n by $(x_{n+1} - x_n)/\overline{x}_m - \overline{x}_n)$ we get Hartmann's equation 87,

$$Kf = \frac{1}{\pi}\left[f_m - f_{m+1} + \sum_{\substack{n=1 \\ n \neq m}}^{N-1} \overline{f}_n \frac{x_{n+1} - x_n}{\overline{x}_m - \overline{x}_n} \right] . \tag{3.39}$$

3.17 Analysis of Diurnal Variations and Pulsations

Hourly means, centered on the full hour, were derived from local midnight to local midnight on eight quiet days (if available) for each line of survey stations and then averaged over these days. After the removal of the noncyclic trend the resultant hourly values were harmonically analyzed in the usual manner (cf. chap. 16 in "Geomagnetism").

Temperature effects diminished the significance of the 1st harmonic, while the consistent behavior of the 2nd and 3rd harmonic showed that they are essentially free from such contaminations (see tabs. 11-15). No attempts have been made to separate or to correlate any anomalous part of the observed diurnal variations, even though local anomalies of internal origin were clearly recognized at many sites.

The time resolution of the records of about one minute did not allow a detailed analysis of pulsations, based on continuous scalings. Instead, peak-to-peak values were measured, separately for each survey station and regardless of time lags between peaks of the three components. This left in particular the horizontal orientation of the disturbance vector undetermined.

The peak values thus obtained were squared and averaged over about ten pulsations or pulsation trains of roughly the same period. Denoting these squared averages with s_D, s_H, s_Z, the mean ratio of vertical to horizontal pulsation amplitude equals

$$[s_Z/(s_D + s_H)]^{1/2} \tag{3.40}$$

for that particular period and survey station (tab. 16).

4. DESCRIPTION OF THE ANOMALIES

4.1 Introduction

The first six months of field operations (January to June 1960) were carried out on a 1000 km east-west profile through the southwestern states, crossing the Southern Rockies, the Rio Grande valley, and extending deep into West Texas (fig. 2). The second phase of the program (November 1960 to February 1962) was devoted to a detailed survey in southern and central California with inclusion of the eastern slope of the Sierra Nevada. The encountered anomalies of geomagnetic variations are now described in geographical order and each anomaly is illustrated by selected magnetograms. Their final interpretation follows in chapter 7. The results of the statistical data reduction are listed in tables 5 to 16.

4.2 Rio Grande Anomaly of Bays and Other Fast Disturbances

The survey was started near Tucson, Arizona, which is well-known for its small Z-variations during bays and magnetic storms (Bartels et al., 1939). This indicates a horizontally stratified conductivity distribution with high conductivities near the surface. Equally subdued Z-variations were found at several field stations around Tucson (NOG, SEL, RAY, COC).

The "Tucson-type" Z-variations end about 400 km east of Tucson. Between Las Cruces and Cornudas the Z-amplitude of bays and storms increases about threefold relative to Tucson. The Z-variations remain of this intensity as far east as Sweetwater, Texas, which was the most eastern survey station (fig. 7).

Already a visual inspection of the traces reveals that the increased Z-variations east of the Rio Grande resemble in their appearance those in D. This indicates that a north-south striking conductivity structure is the underlying cause for the anomalous behavior of Z, parallel to the Rocky Mountain front in New Mexico. The increased Z-amplitude does not seem to be restricted to a limited area, since no equivalent to the subdued "Tucson-type" Z-variations has been found in West Texas.

Hence, we have here a regional change of the internal part of bays. The increased Z-variations at Sweetwater as well as the reduced Z-variations at Tucson are both considered to be "normal" in the sense that these stations lie within regions of stratified but different internal structures with high mantle conductivities west and low mantle conductivities east of the Rio

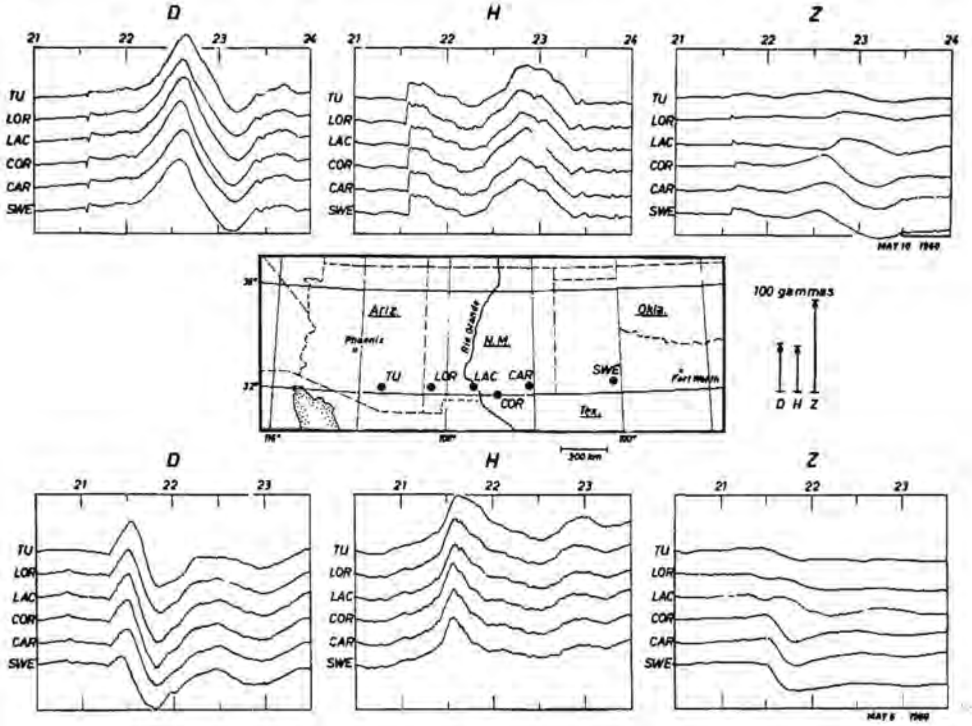

Fig. 7. Two bays as recorded on the profile Tucson-Sweetwater through southern Arizona, New Mexico, and West Texas. Distinct increase of Z-amplitude east of the Rio Grande, preceded by a reversal between Las Cruces and Cornudas.

Grande. Superficial eddy currents contribute in this area only negligibly to the internal part of bays and can be ruled out as a possible source of the anomaly (sec. 7.5).

Superimposed upon this regional change is the Z-reversal between Las Cruces and Cornudas, indicating a shallow concentration of eddy currents. Hence, we may assume that an additional uplift of highly conducting matter exists under the Rio Grande rift valley. Short-period fluctuations and storms show essentially the same anomalous behavior as bays, even though the complex Z-traces of the "ssc" in figure 8 reflect the increasing influence of near-surface conductivity contrasts in the case of fast variations. Striking is the smooth appearance of the Z-trace of Sweetwater, which indicates a rather undisturbed layering of Permian sediments near that site.

Consistent differences of the horizontal variations along the profile Tucson-Sweetwater are less conspicuous in the magnetograms and, in addition, they are overshadowed by inhomogeneities in the primary field from

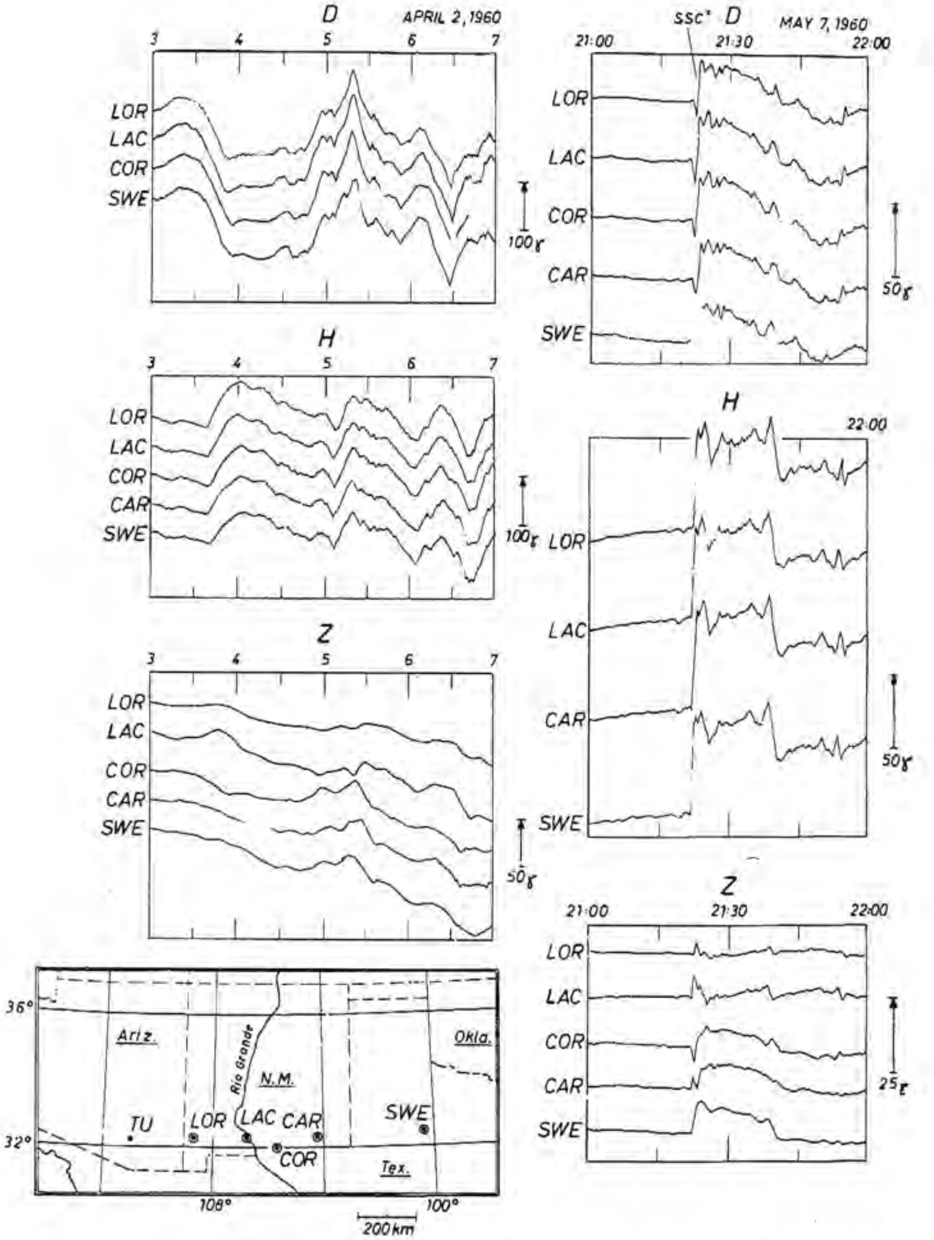

Fig. 8. Segment of magnetic storm and "sudden storm commencement," recorded between Lordsburg in western New Mexico and Sweetwater in West Texas. Reversal and increase of the storm-time Z-amplitude east of the Rio Grande as in the case of bays (cf. fig. 7). The anomalous behavior of fast Z-fluctuations during the "ssc" is complicated by the influence of near-surface conductivity variations. Notice the uniformity of the H and D-variations over 800 km in east-west direction (cf. fig. 27).

above. It has been clearly established, however, that D-variations are larger by about 20% at Las Cruces and Cornudas than elsewhere. This agrees well with the assumed current concentration beneath these stations.

The statistical evaluation of the differences in D and H led to the hp-profile in figure 9 (cf. eq. 3.26 for definition of hp and zp). It agrees fairly well with a calculated h_p-profile according to (3.36) which ensures (a) that the anomaly is indeed of internal origin, (b) that the field stations were spaced adequately to describe the anomaly in sufficient detail.

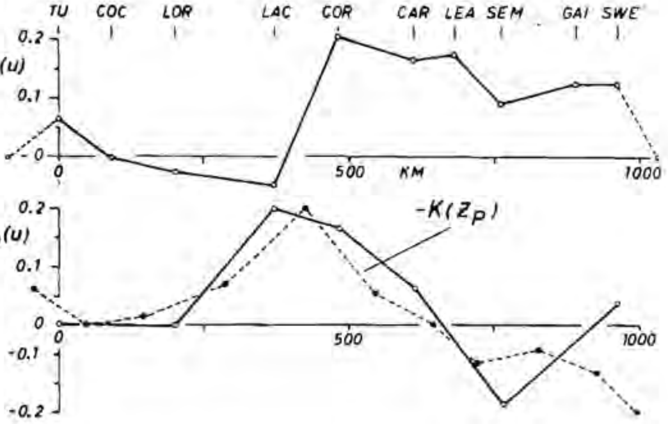

Fig. 9. Normalized anomalous behavior of vertical (z_p) and horizontal (h_p) variations for the profile Tucson-Sweetwater during bays (1 cph). Shown is the in-phase component of the pertinent projected transfer values. The dashed h_p-profile has been derived from the z_p-profile shown above by applying Kertz's operator to z_p (cf. equation. 3.36).

The east-west profiles in figure 10 and the displays of induction arrows in figure 11 summarize the results of the statistical data reduction. The zp-profiles show clearly the enhancement of the in-phase Z-component east of the Rio Grande, preceded by a reversal at Las Cruces. This reversal becomes more pronounced for fast variations. We observe that the in-phase and out-of-phase parts of zp preserve a fairly constant ratio, indicating a phase lead of Z_a relative to the normal parts in H and D. This phase lead is not constant but decreases from 45° at 0.5 cph to practically zero at 4 cph. The in-phase arrows point consistently toward the high conductivity zone between Las Cruces and Cornudas. The out-of-phase arrows are less consistent and we may not exclude the possibility that this is due to some near-surface irregularities.

4.3 Rio Grande Anomaly of Diurnal Variations

The analysis of four quiet days revealed that also the slow diurnal variations undergo a distinct change between Arizona and West Texas (tab. 11). Differences in D and H are insignificant, irregular, and they can be explained

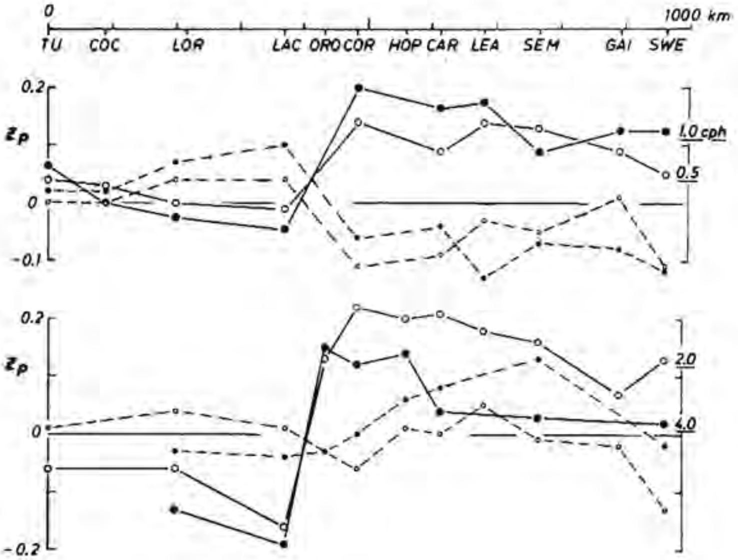

Fig. 10. Cross sections through the "Rio Grande anomaly" for various frequencies between 0.5 and 4 cph. Connected with solid lines: in-phase transfer values z_p (u) for the anomalous part in Z; connected with dashed lines: negative out-of-phase transfer values $-z_p(v)$.

by the local time dependence of Sq-variations. This is not so for the spatial differences in Z which seem to be significant and reproducible from day to day.

We observe that the center of the northern Sq-vortex passes during the equinoxes more or less overhead of the east-west line of survey stations which lie therefore in the range of maximum external Z-variations. Hence, the here observed diurnal Z-amplitude, normalized with the horizontal true-east Y-amplitude, is as the sum of external and internal Z-fields, a sensitive measure for the deep conductivity structure.

Very conspicuous in the harmonic dials of figure 12 is the systematic eastward increase of the Z/Y ratio of the 2^{nd} and 3^{rd} harmonic, which is at Sweetwater nearly twice as large as at Tucson. This conforms well with the anomalous behavior of faster variations and suggests that the postulated contrast in mantle conductivity between Arizona and West Texas extends downward to great depth.

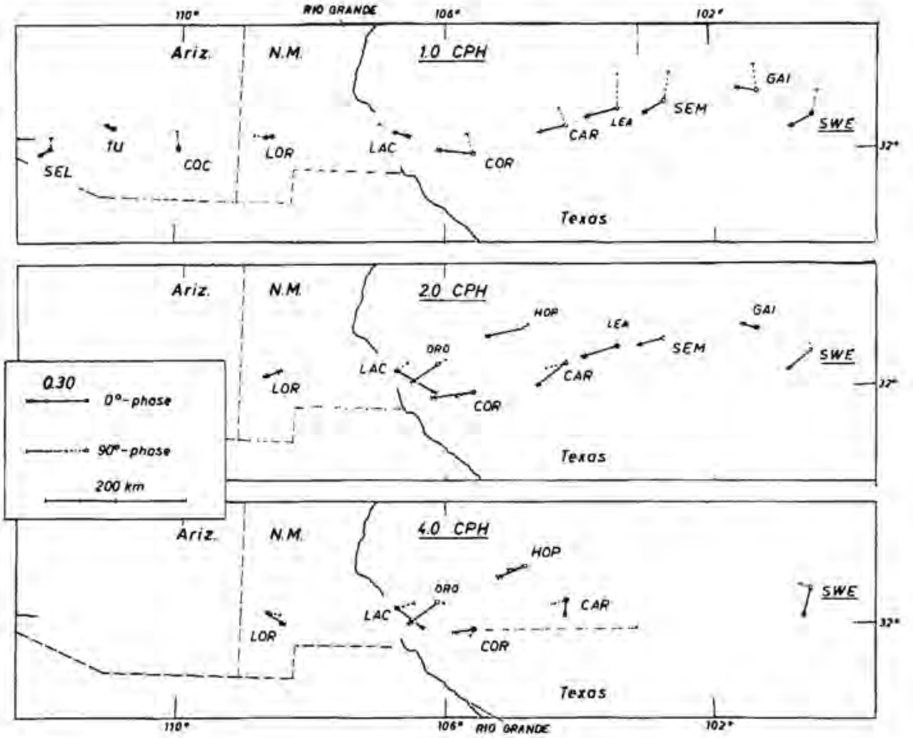

Fig. 11. Induction arrows in southern Arizona, New Mexico, and West Texas, illustrating the anomalous behavior of Z-variations between 1 and 4 cph. In-phase arrows point at 1 and 2 cph toward a high conductivity channel between Las Cruces and Cornudas and toward high internal conductivities west of the Rio Grande. Open circles: $\epsilon_Z < 0.25$; full circles: $\epsilon_Z > 0.25$. The pertinent transfer values z_H and z_D of table 1 have been recalculated for Sweetwater as common reference station for all sites.

4.4 Coastal Anomaly in California of Bays and Other Fast Disturbances

From Tucson westward the "Tucson-type" of reduced Z-variations prevails as far as Cameron, a field station 80 km from the coast in southern California. There is a local increase of the Z-amplitude at Yuma, Arizona, which is absent at the nearby stations of Tacna, Arizona, and El Centro, California.

From Cameron the Z-amplitude increases continuously toward the sea, reaching its maximum value at the shore (fig. 13). About 100 km offshore on the island of San Clemente the Z-variations are reduced again considerably. This island lies on the continental shelf within a rough ocean bottom topography with an average water depth of 1 km around it. The edge of the shelf is reached 150 km further seaward from San Clemente.

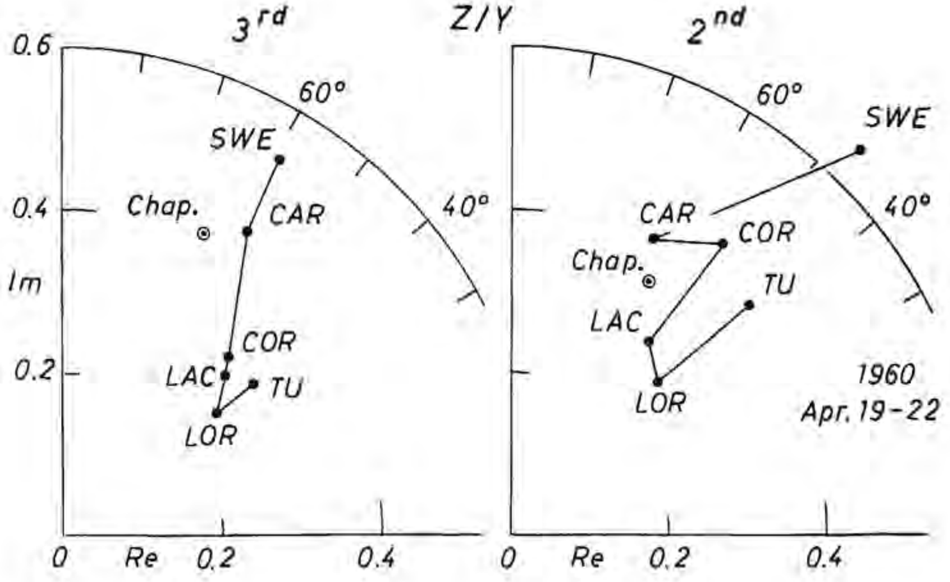

Fig. 12. Polar diagram showing the 2^{nd} and 3^{rd} harmonic of diurnal Z-variations, averaged over four quiet days and divided by the harmonics of the mean diurnal Y-variations of the same days as recorded at the same site. Distinct increase of the Z-amplitude from a minimum in western New Mexico (LOR) toward Sweetwater in West Texas, reflecting the unusually deep penetration of diurnal variations through low mantle conductivities east of the Rio Grande. Z leads relative to Y. The global average "CHAP" of the Z/Y ratio for this magnetic latitude has been derived from (5.14) for comparison, using Chapman's ratio of internal to external parts for the equinoxes 1902/05 (tab. 4 in chap. 20 of Geomagnetism) and setting $\theta = 50°$.

The enhanced Z-variations near the coast are clearly correlated to those in D and H when projected onto a direction perpendicular to the coastline. For instance, during the bay of August 30 D and H are roughly antiparallel and the resulting horizontal disturbance vector points more or less parallel to the coast. Consequently, the Z-variations at La Jolla are small and irregular. During the bay of August 29 D and H are parallel, yielding a disturbance vector perpendicular to the coast, and we observe strong Z-variations at La Jolla.

Coastal anomalies of this kind reflect an offshore concentration of eddy currents. They seem to be a common feature of continental margins. Parkinson (1959, 1962) showed that they exist at many places around the world. So far only one coast near a deep ocean has been found where this anomaly is clearly absent, namely, the coast of southern Peru (Schmucker et al., 1964).

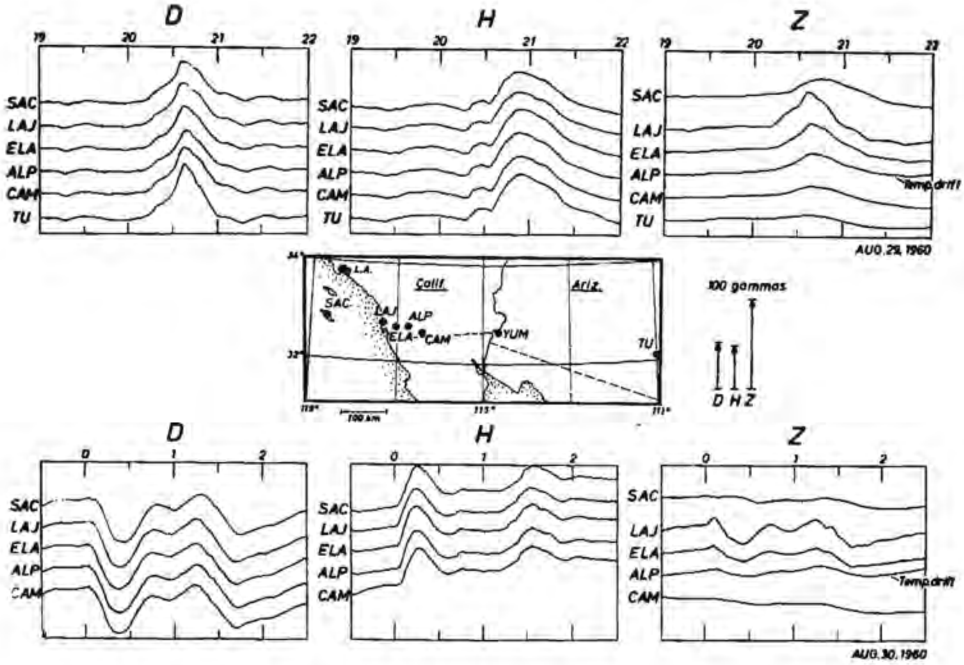

Fig. 13. Two bays as recorded on the profile San Clemente Island-Tucson through southern California. Prominent Z-variations at the coastal station La Jolla gradually diminish toward the open ocean and toward inland. Slight reduction of the D-amplitude near the coast in comparison to the D-amplitude at Tucson.

As already stated by Parkinson, coastal anomalies could arise from different mantle conductivities under continents and oceans. It would imply that a steep uplift of highly conductive material occurs along the continental slope, bringing deep induction currents near to the surface below the sea floor. On the other hand, these anomalies coincide with an outstanding superficial conductivity contrast and they could be "edge effects" of oceanic eddy currents which cannot penetrate into the less conducting continental surface layers and are forced to flow parallel to the coastlines.

Because of the complicated coastal structure in southern California it was decided to conduct similar observations in central California, where the continental shelf is just 100 km wide. The station on the Farallon Islands offshore San Francisco was even within 40 km of the continental slope. Three lines of field stations were set up perpendicular to the coast and extending about 400 km inland. These profiles crossed three geological structures, (a) the California coast range, (b) the San Joaquin valley, (c) the Sierra Nevada (fig. 21). It should be noted that the San Joaquin valley is a young embayment, filled with unconsolidated sediments of presumably high conductivity, in contrast to the poorly conducting granitic bloc of the Sierra

Nevada. To supplement these land-based recordings Cox and his collaborators at Scripps conducted at the same time observations at sea which are essential to reach definite conclusions about the actual strength and direction of eddy currents in the ocean itself. Their results will be published elsewhere.

Typical bays as observed on the three profiles are displayed in figures 14 to 17. We notice again strong Z-variations along the shoreline which disappear gradually inland. A reduction of the D- and H-amplitudes near the coast is also clearly visible. The anomalous behavior of short-period fluctuations resembles more or less that of bays (fig. 18), even though differences from station to station show many more details. This is probably due

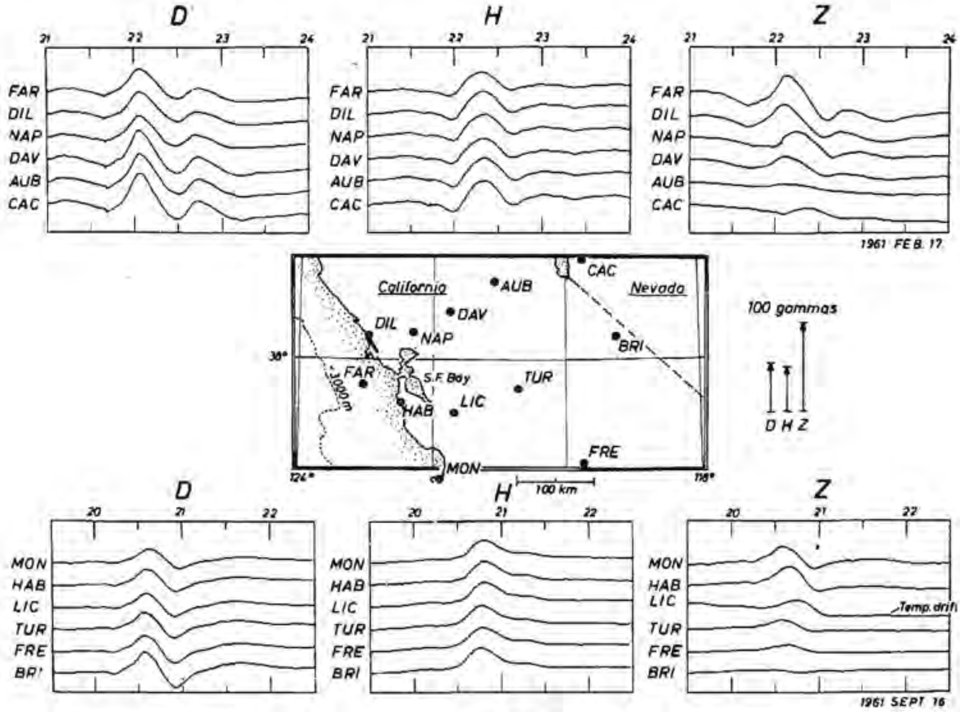

Fig. 14.. Two bays as recorded on the profiles Farallon Islands-Carson City and Monterey-Bridgeport through central California. Strong Z-variations and subdued H- and D-variations near the coast reflect the coastal anomaly of bays in central California where the continental shelf is narrow. Distinct phase lags of the gradually disappearing Z-variations at Napa and Lick Observatory characterize the "inland anomaly" of the San Joaquin valley, and reversed Z-variations at Carson City and Bridgeport the "inland anomaly" along the eastern slope of the Sierra Nevada.

to the irregular flow of very shallow induction currents. Striking are again the pronounced Z-amplitudes at the coast and the accompanying reduction in D and H. By intercomparison it might be noticed that the attenuation of Z toward inland occurs within a shorter distance from the coast than during bays.

The anomalous parts in D and H have been obtained by subtracting from the observed variations those of "reference stations" about 200 km inland (AUB, FRE, MOJ, CAM). It is now realized that these reference stations are still under the influence of the coastal anomaly and that their horizontal variations are roughly 10% below the normal level.

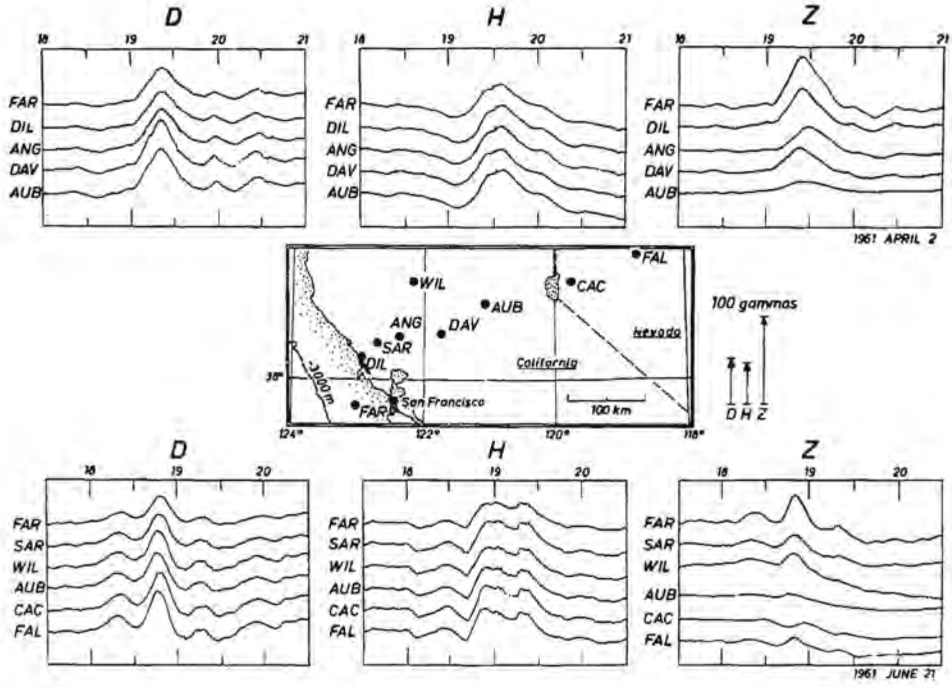

Fig. 15. Two bays as recorded on the profile Farallon Islands-Fallon, Nevada. The coastal anomaly is clearly visible in all three components (cf. legend of fig. 14) in addition to a distinct Z-reversal between Carson City and Fallon.

The results of the statistical correlation analysis between the observed Z-variations and the thus defined normal parts in H and D are shown in figures 19 to 21 by induction arrows. Cross sections through the anomaly can be found in section 7.2 in conjunction with model calculations. The in-phase arrows, even at some distance from the shoreline, point strictly toward the ocean, i.e., toward an offshore concentration of induced eddy currents.

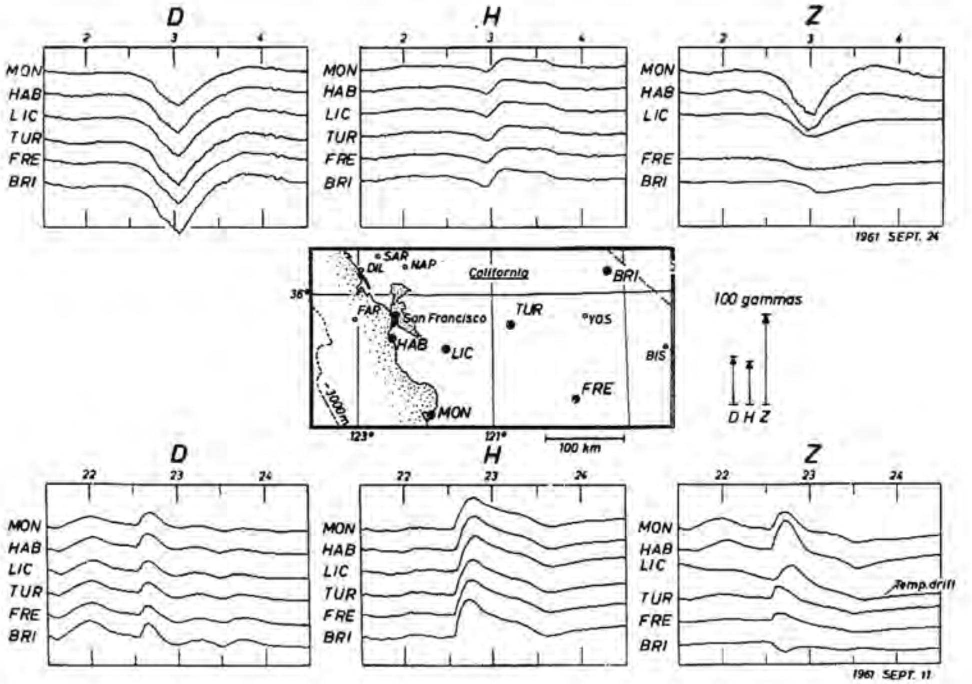

Fig. 16. Two bays as recorded on the profile Monterey-Bridgeport and their anomalous behavior near the coast (cf. legend of fig. 14). Clear reversal in Z between Fresno and Bridgeport during the Sept. 11 event.

We notice that the arrow of 1.0 cph at the southern coast (La Jolla) is about half as long as the corresponding arrows in central California, indicating that the in-phase Z-amplitude of La Jolla is about half as big as at the coast further north. In addition, the out-of-phase arrow at La Jolla points distinctly away from the coast which means that the (anomalous) Z-variations lead in phase relative to those in H and D by about 30°. This phase shift is negligible and irregular at the northern stations. All these observations can be related to the shallow water depth offshore the southern coast and to the resulting reduction of the integrated induction current in the ocean (when we interpret the anomaly as oceanic edge effect).

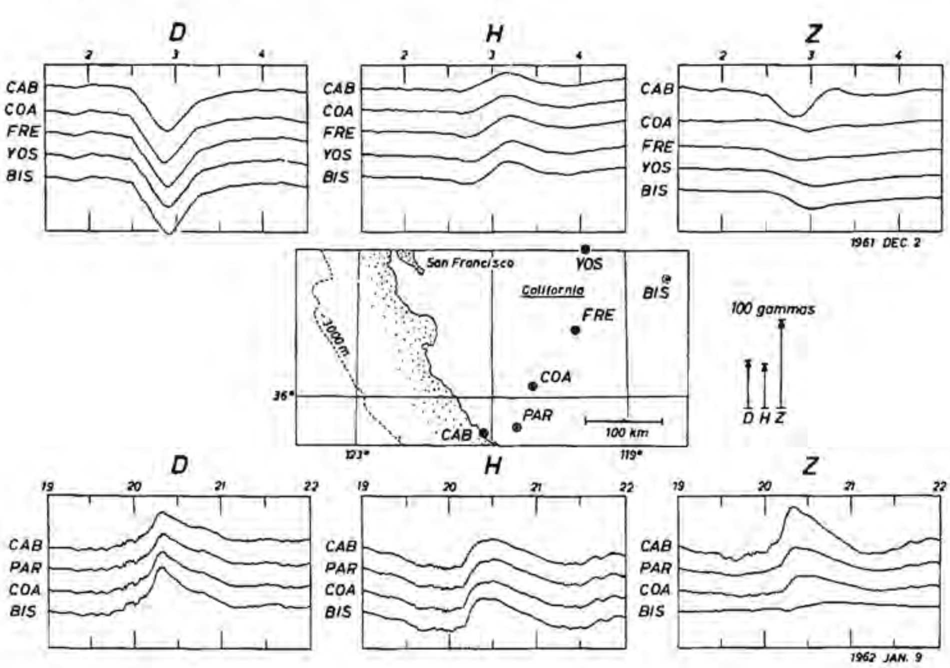

Fig. 17. Two bays, recorded on the coastal profile Cambria-Bishop halfway between San Francisco and San Diego. The anomalous Z-amplitude near the coast is here partially correlated with D and partially correlated with H, reflecting the bend in the California coastline at Point Conception (see induction arrow of CAB in fig.19.)

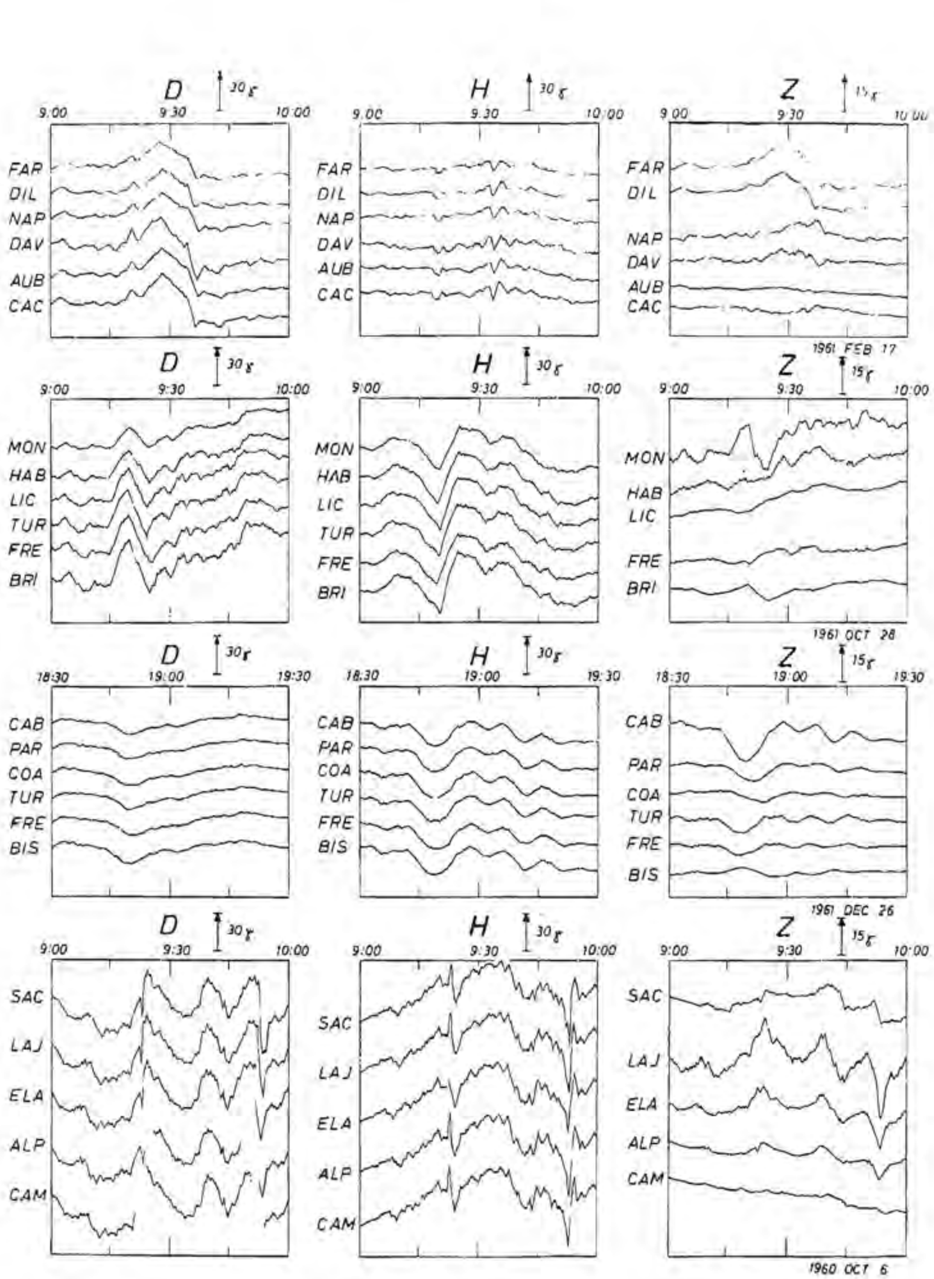

Fig. 18. Fast fluctuations, assembled for the four profiles through central and southern California. Their anomalous behavior near the coast is similar to the anomalous behavior of bays as shown in fig. 14. Notice the abrupt disappearance of the strong Z-fluctuations at the coast toward inland (FAR-NAP, MON-LIC, CAB-COA).

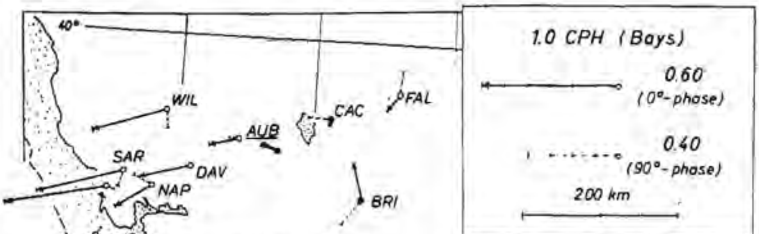

Fig. 19. Induction arrows (sec. 3.10) in central and southern California at 1 cph. In-phase arrows point toward a strong offshore concentration of internal, probably oceanic induction currents. A high conductivity spot is indicated by in-phase and out-of-phase arrows in the triangle Carson City-Fallon-Bridgeport (cf. figs. 20 and 21). Reference stations are underlined. Open circles: residuals ϵ_Z less than 0.25; full circles: residuals exceed 0.25.

4.5 Inland Anomalies in California and Nevada

In addition to this predominant feature of the coastal anomaly we observe also some minor anomalies further inland. They can be characterized as follows: (a) The Z-amplitudes reverse their sign on the eastern slope of the Sierra Nevada at CAC, BRI, BIS; (b) Z-variations show a distinct phase shift about 80 km inland near the margin of the San Joaquin valley at NAP (ANG), LIC, COA; (c) the Z-amplitude does not decrease considerably (as expected) between NAP and DAV, LIC and TUR, COA and FRE, even though the last-mentioned stations lie about twice as far inland as the first-mentioned ones.

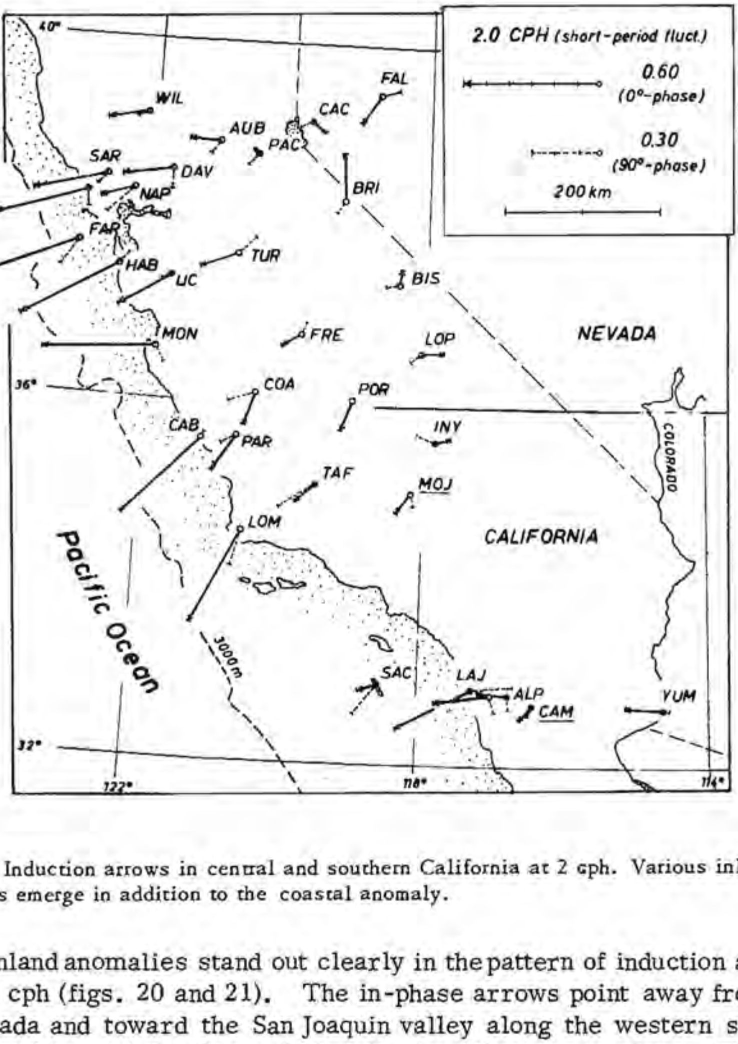

Fig. 20. Induction arrows in central and southern California at 2 cph. Various inland anomalies emerge in addition to the coastal anomaly.

These inland anomalies stand out clearly in the pattern of induction arrows for 2 and 4 cph (figs. 20 and 21). The in-phase arrows point away from the Sierra Nevada and toward the San Joaquin valley along the western slope of the Sierra and toward the State of Nevada along the eastern slope. The out-of-phase arrows point consistently in the opposite direction, which implies that the eddy currents involved lead in phase relative to the normal horizontal variations.

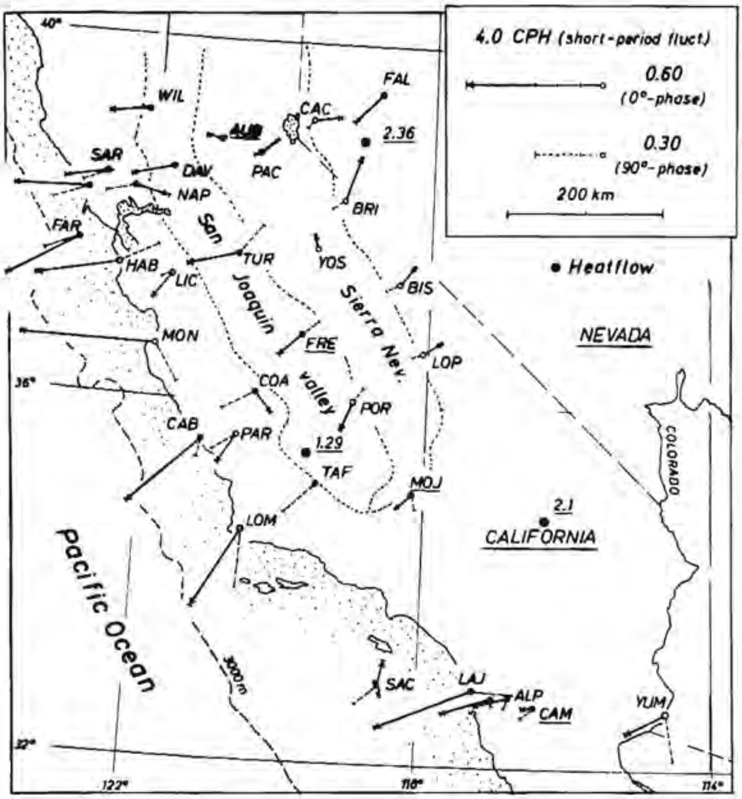

Fig. 21. Induction arrows in central and southern California at 4 cph. The coastal anomaly is confined now to a narrow strip parallel to the coast, about 100 km wide. Further inland, the in-phase arrows point (*a*) toward concentrated superficial induction currents in the sediments of the San Joaquin valley, and (*b*) toward a shallow concentration of deep induction currents parallel to the eastern slope of the Sierra Nevada. Notice the coincidence of high internal conductivities and high terrestrial heat flow in the triangle CAC-BRI-FAL (cf. fig. 47).

We conclude that in addition to the strong offshore concentration of eddy currents there must be smaller concentrations of surface or subsurface eddy currents in the San Joaquin valley and along the eastern slope of the Sierra Nevada.

4.6 Coastal Anomaly in California during Magnetic Storms

Various sections of magnetic storms have been assembled in figure 22. They reveal the same general increase of the Z-amplitude from inland toward the coast which we have found already during bays and other short-period events. Since the overhead current distribution is less uniform during storms than during bays, a concurrent analysis of their anomalous behavior could indicate how the nonuniformity of the primary field influences the correlation between anomalous and normal parts (source-field dependence of the transfer functions).

For that purpose a typical storm as recorded on the southern profile (Pl. II) has been analyzed according to the method outlined in section 3.7. Power spectra have been calculated for the horizontal variations at the reference station Cameron and for the Z-variations of all survey stations. Cross spectra were derived between Z (all stations) and D_{CAM} and between Z and H_{CAM}. The resulting spectral values for the frequencies 0, 1/2, 1 ... 12 cph were then inserted into the basic formulae of the correlation analysis (eqs. 3.22 and 3.17), yielding the transfer functions $z_H(f)$ and $z_D(f)$ together with the pertinent residual $\epsilon_Z(f)$. They are listed in table 6 z*. A comparison with corresponding values for single events (tab. 6 z) shows that both sets of transfer values agree within the statistical limits set by the residuals, a convincing demonstration that the analysis of storms and single events leads to comparable results.

A minor but consistent discrepancy deserves our attention. We infer from figure 23 that the in-phase transfers of La Jolla are at frequencies below 4 cph a bit smaller for the storm than for the single events, while the out-of-phase transfers agree fairly well. This implies that the subterranean eddy currents which are responsible for the anomaly are somewhat weaker during storms than during single events and a bit more out-of-phase with respect to the source field. Both observations are in perfect agreement with the increased nonuniformity of the large-scale storm field and the resulting reduction and phase shift of the internal induction.

Of particular interest is a comparison of the residuals, since the analysis of the storm involve about the same amount of independent information as the analysis of the single events. It turns out that the residuals are of comparable size. Only beyond 4 cph do the residuals of the storm correlation analysis seem to outweight those of single events.

The power spectra of Z in figure 24 summarize impressively the decrease of the coastal Z-amplitude toward inland and toward the open ocean as function of frequency. Notice in particular that the slope of the Z-spectra between 0.5 and 2 cph is clearly steeper at Cameron than at La Jolla. This verifies the statement above, namely, that the anomalous Z-amplitudes at the coast disappear for high frequencies more rapidly toward inland than for low frequencies. Above 6 cph the Z-spectra flatten out and merge into a general noise level. Lowest residuals and therefore maximum coherence between Z and the normal horizontal variations are found near 1 cph.

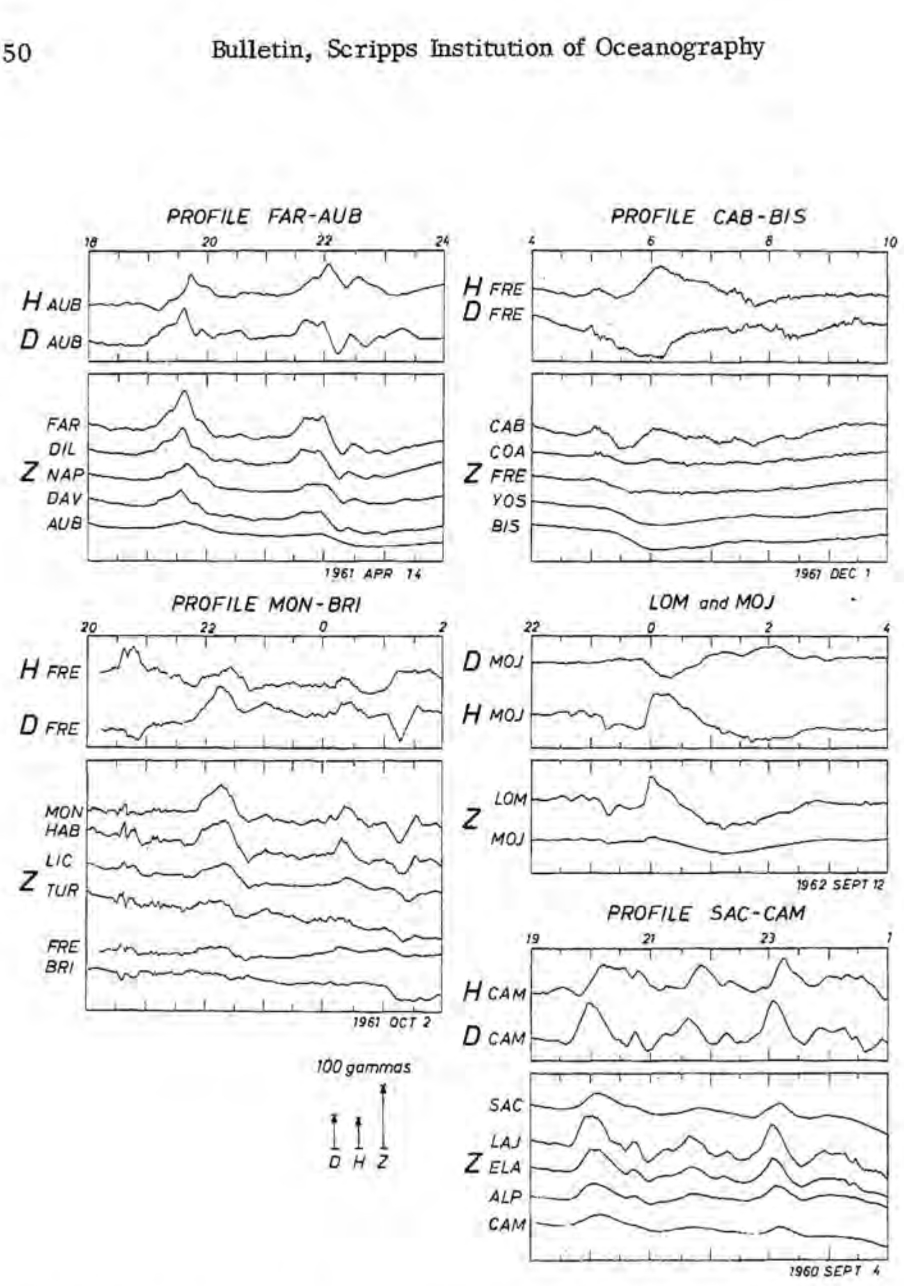

Fig. 22. Six-hour long segments with storm-time variations, assembled for the various profiles perpendicular to the California coast. Clear correlation between D at the inland reference stations AUB, FRE, CAM and Z at the coastal stations FAR+DIL, MON+HAB, LAJ, reflecting the predominant north-south trend of the coastline and of the coastal anomaly. The change into an east-west direction south of Point Conception (station Lompoc) is clearly evident from the correlation of Z at LOM and CAB with H at MOJ and FRE.

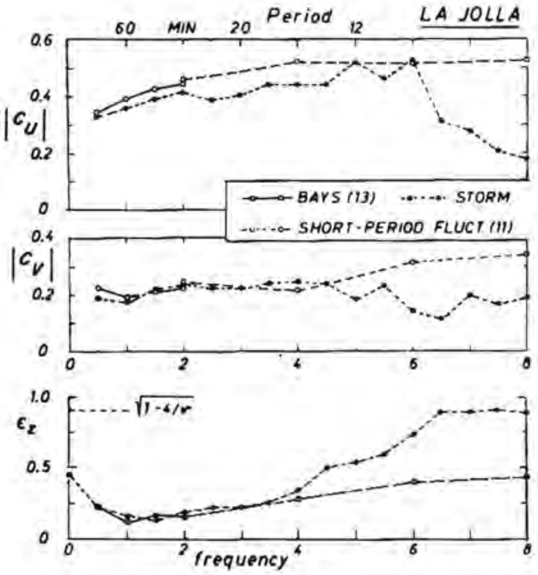

Fig. 23. Length of the induction arrow **c** at the coastal station La Jolla as function of frequency. $\mathbf{c}_u$: in-phase arrow; $\mathbf{c}_v$: out-of-phase arrow. The results from the analysis of a magnetic storm are compared with those from the analysis of 24 single events.

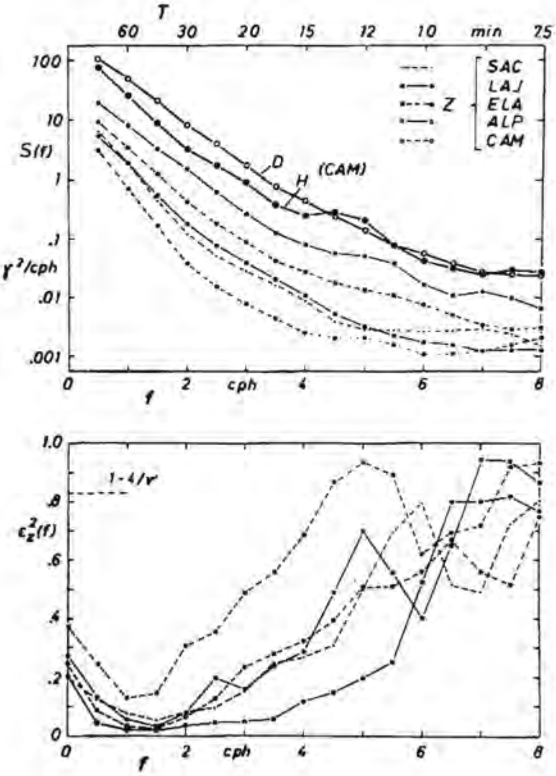

Fig. 24. Upper diagram: power spectra of storm-time variations in D, H, and Z as observed on the profile San Clemente Island-Cameron in southern California (see sec. 4.6). Lower diagram: power spectra of the unrelated portions of the Z-records, normalized with the total power in Z, after correlating Z with the horizontal variations of the reference station Cameron (cf. text).

4.7 Anomalies of Diurnal Variations in California

Coastal anomalies of diurnal variations have been reported from Japan (Rikitake, 1959) and from the edge of the continental shelf offshore from the British Isles, where Hill and Mason (1962) recorded the total-field variations in a floating buoy. They found a strong enhancement of the diurnal variations, in particular of their semidiurnal component, relative to observations at a land-based station.

We infer from the hourly means in figure 25 and from the harmonic coefficients in tables 12 to 15 that the diurnal Z-amplitude is nearly doubled at the California coast relative to inland, while the horizontal amplitudes hardly vary along the three profiles. The harmonic dial of figure 26 summarizes this coastal anomaly for the 3^{rd} harmonic in Z.

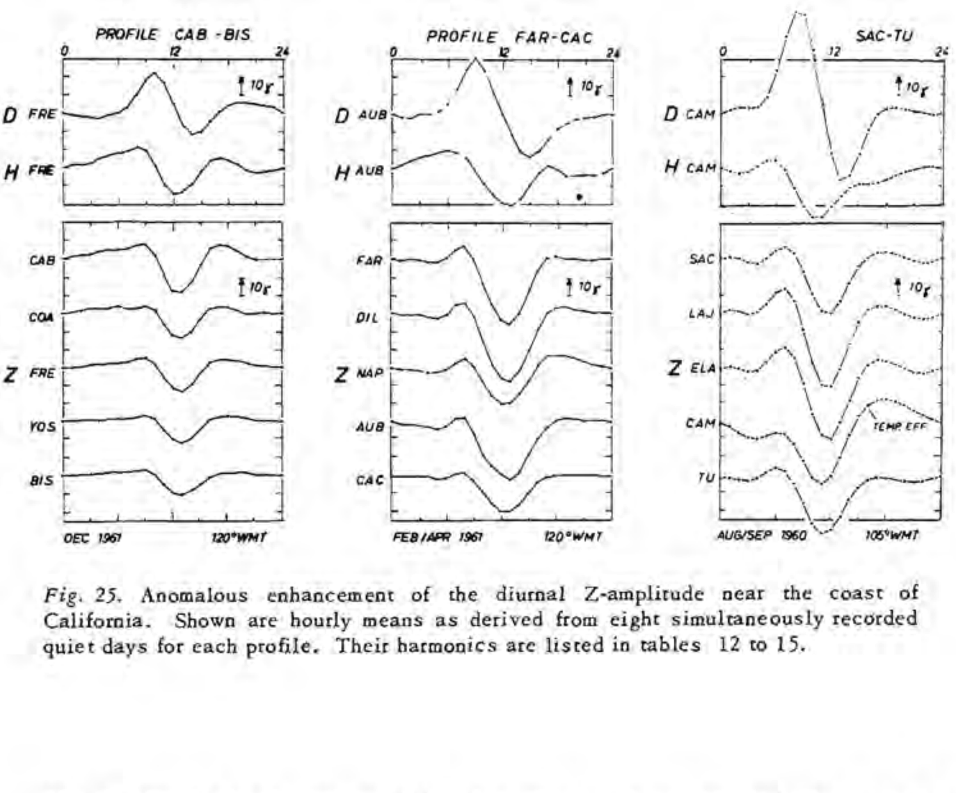

Fig. 25. Anomalous enhancement of the diurnal Z-amplitude near the coast of California. Shown are hourly means as derived from eight simultaneously recorded quiet days for each profile. Their harmonics are listed in tables 12 to 15.

The Z-amplitude decreases sharply between the coast and stations about 100 km inland, but it remains constant then until it drops off again eastward of the San Joaquin valley. Roden's calculations (1964) suggest that an anomaly of this kind should exist in connection with diurnal induction currents in the ocean, but the observed anomaly turns out to be much more narrow and complicated than anticipated from the anomalous behavior of bays.

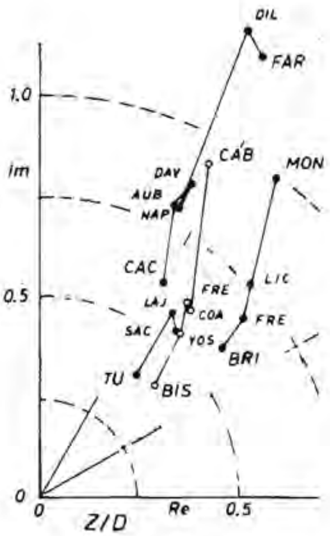

Fig. 26. Polar diagram showing the Z/D ratio of the 3^{rd} diurnal harmonic, averaged over eight quiet days on the four profiles (cf. tabs. 12-15). Amplitude reduction of the Z-harmonic from the coast toward inland (cf. fig. 25), accompanied by a small but consistent reduction of the phase lead of Z relative to D.

4.8 Anomalies of Pulsations in California

The induced eddy currents of rapid pulsations flow mainly in geological surface strata, where they are channeled into sedimentary basins and similar zones of high conductivity. We may expect therefore pronounced Z-pulsations at the edges of such zones as they appear indeed along the San Joaquin valley at Turlock Lake, Fresno, and Davis (tab. 16). They are conspicuously absent at stations like Lick Observatory and Yosemite, indicating here a smooth flow of eddy currents.

Some coastal stations (MON, HAB) show strong Z-pulsations, others do not (DIL, CAB). Hence, oceanic eddy currents of pulsations diffuse at some place into the continental surface layers without producing an edge effect.

Subsequent to this survey Warren (1964) studied the Z-amplitude of pulsations in central California in great detail to test their qualification as a "geological mapping tool" for sedimentary deposits of variable thickness. He made observations at 24 sites between Monterey and Yosemite, spaced 5 to 20 km apart, and found a distinct reversal of the Z-pulsations when crossing the San Joaquin valley and two other basins of smaller dimensions.

4.9 IGY Network in the Midwestern United States

The U. S. Coast and Geodetic Survey established during the IGY 1957-58 a net of seven magnetic field stations in the midwestern states (cf. Matsushita, 1960). The distance between stations was too large to allow definite conclusions about any anomalous behavior of geomagnetic variations in that area. Nevertheless, the stations Leadville (Colorado) and Espanola (New Mexico) show the "Tucson-type" of reduced Z-amplitudes, while stations further to the east, namely, Burlington (Colorado), Beliot (Kansas), and Carrolton (Missouri), display substantial Z-variations during bays and similar events (fig. 27).

This corresponds well to the change of the Z-amplitude further south as reported in section 4.2. Recent investigations by Reitzel (1967) confirmed the existence of a Rio Grande-type anomaly at the Rocky Mountain front in Colorado. Striking are the large Z-amplitudes at Price, Utah, which are correlated with those in D. Hence, we have to expect a north-south striking zone of high internal conductivity along the western edge of the Colorado Plateau. This anomaly deserves further attention.

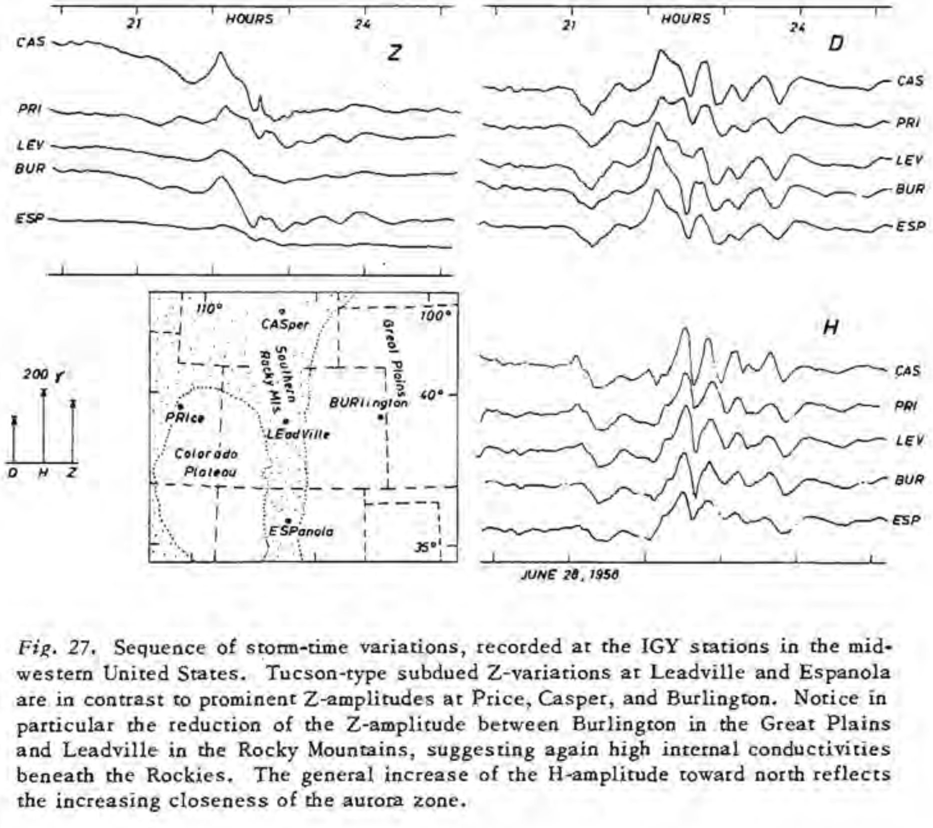

Fig. 27. Sequence of storm-time variations, recorded at the IGY stations in the mid-western United States. Tucson-type subdued Z-variations at Leadville and Espanola are in contrast to prominent Z-amplitudes at Price, Casper, and Burlington. Notice in particular the reduction of the Z-amplitude between Burlington in the Great Plains and Leadville in the Rocky Mountains, suggesting again high internal conductivities beneath the Rockies. The general increase of the H-amplitude toward north reflects the increasing closeness of the aurora zone.

5. ELECTROMAGNETIC INDUCTION IN STRATIFIED CONDUCTORS

5.1 Introduction and References

This chapter considers the various properties of the normal part of geomagnetic variations above and within a layered earth. Outstanding reference with regard to the induction in spherical conductors is chapter 22 in Chapman and Bartels' (1940) treatise. It summarizes the previous work of various authors including that of Lahiri and Price (1939). The conductive half-space with a plane boundary has been the subject of a subsequent paper by Price (1950).

We consider here multilayered conductors in which the conductivity changes discontinuously at plane or spherical interfaces. Analytic solutions take then the form of recurrence formulae that satisfy step by step the continuity condition of the field at each interface. Their formulation is due to Wait (1953) and Srivastava (1966). A different approach, suitable for numerical integration, has been proposed by Eckhardt (1963).

The decisive frequency-conductivity parameter is the skin-depth value

$$p = (2\pi\omega\sigma\mu)^{-1/2} \tag{5.1}$$

($\mu = 1$). It gives the depth beneath the surface of a uniform conductor, where the amplitude of an incident variation field is reduced to $1/e$ of its surface value when $p \ll L/2\pi$ (see below). Rewriting (5.1) in more convenient units, namely, in cph for ω and in $(\Omega m)^{-1}$ for σ, gives

$$p = 30.2 \cdot (f\sigma)^{-1/2}\ [\mathrm{km}]\,.$$

The spatial configuration of the surface field will be expressed by a series of spherical functions P_n^m or by a spectrum of plane waves. Considering a single term P_n^m or a single wave component of the wave number k we characterize its spatial nonuniformity by its wave length

$$L = 2\pi/k = 2\pi a/n \tag{5.2}$$

with a as the radius of spherical conductors.

The notations S_n^m and S(k) shall be used to designate the ratio of internal to external tangential variations at the surface of the conductor for one particular wave component. This ratio varies between zero for no induction and $S_n^m = n/(n+1)$, respectively $S(k) = 1$, as upper inductive limit. Due to the opposing effect of self-induction the internal part cannot increase beyond this limit, since the incident variation field is shielded now completely from the interior of the conductor by eddy currents in the outermost layers.

Let

$$T(k) = [1 - S(k)] / [1 + S(k)] \; . \tag{5.3}$$

Then the surface ratio of vertical to horizontal variations and the surface impedance (ratio of tangential electric to orthogonal magnetic field variations) become simply

$$Z/H = iT(k) \qquad \mathcal{E}/H = i\,\omega T(k)/k \, . \tag{5.4}$$

Corresponding relations for spherical conductors are a bit more complicated (cf. eqs. 5.14 and 17).

Hence, a general relation of the form

$$k\,\mathcal{E} = \omega\, Z \tag{5.5}$$

connects tangential electric with vertical magnetic variations independently of the internal conductivity distribution (which of course must be stratified). This allows an effective control for the compatibility of electric and magnetic observations which was first utilized by Chapman and Whitehead (1923).

Vertical Z-variations disappear when the internal part approaches its upper inductive limit, yielding $S(k) = 1$. The impedance, on the other hand, remains finite, since the ratio $T(k)/k$ has a limiting value $c \neq 0$ for $T(k) \to 0$, where c is a complex valued measure for the mean depth of the internal eddy currents and for the skin-depth value at that depth (sec. 5.5). The impedance becomes thereby independent of k and solely determined by the internal conductivity distribution which is the basis of Cagniard's magnetotelluric method.

5.2 Spherical Conductors

Consider a conductive sphere of radius a, surrounded by nonconducting matter and consisting of N - 1 concentric shells of different conductivity plus an inner core (fig. 28). The sphere is exposed to a transient electromagnetic

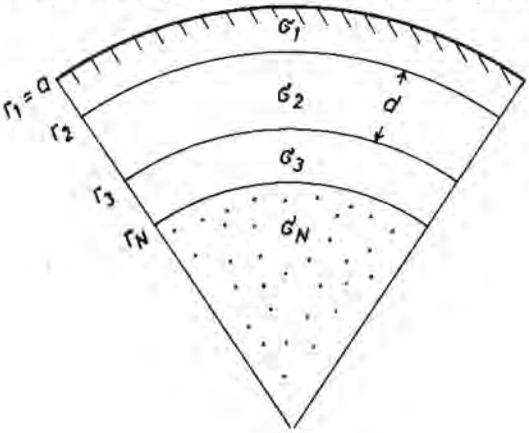

Fig. 28.

field of external origin. It is considered to be irrotational in the neighborhood of the sphere and expressible for $r \geq a$ as gradient of a scalar potential function

$$U(t, r, \theta, \phi) = a \sum_{n=1}^{\infty} \sum_{m=0}^{n} [(r/a)^n \cdot E_n^m(t) + (a/r)^{n+1} \cdot I_n^m(t)] P_n^m(\cos\theta) \exp(im\phi) \tag{5.6}$$

with the usual notations for spherical coordinates and spherical surface harmonics. $E_n^m(t)$ and $I_n^m(t)$ are complex-valued coefficients in reference to the external and internal part of the outside field. Their time dependence shall be harmonic, taking the real part of

$$E_n^m(t) \cdot \exp(im\phi) = (E_u + iE_v) \cdot \exp(i\omega t + im\phi) \tag{5.7}$$

and of a corresponding expression for $I_n^m(t)$.

Each term P_n^m has on the surface $r = a$ the orthogonal field components

$$\left.\begin{aligned} H_\theta &= -a^{-1}\, \partial U/\partial\theta = -[E_n^m + I_n^m] dP_n^m/d\theta \\ H_\phi &= -(a \sin\theta)^{-1}\, \partial U/\partial\phi = -[E_n^m + I_n^m] imP_n^m/\sin\theta \\ H_r &= -\partial U/\partial r = [-nE_n^m + (n+1) I_n^m] P_n^m \end{aligned}\right\} \exp(im\phi) \tag{5.8}$$

as readily seen by differentiation of (5.6). The attenuated field within the ν^{th} shell may be written in the form

$$\left.\begin{aligned} H_\theta &= f'_\nu(t, r)\, dP_n^m/d\theta \\ H_\phi &= f'_\nu(t, r)\, imP_n^m/\sin\theta \\ H_r &= f_\nu(t, r)\, n(n+1) P_n^m \end{aligned}\right\} [i\omega r]^{-1} \exp(im\phi) \tag{5.9}$$

with

$$f'_\nu = \frac{d}{dr}(rf_\nu)$$

and $f_\nu(t, r)$ being a solution of the differential equation

$$r^2 \frac{d^2 f_\nu}{dr^2} + 2r \frac{df_\nu}{dr} - [n(n+1) + 4\pi i \omega \sigma_\nu r^2] f_\nu = 0. \tag{5.10}$$

This renders the inside field distribution nondivergent and makes it a solution of the diffusion equation (1.5).

The general solution of (5.10) is

$$f_\nu(t, r) = A_\nu(t) \cdot j_n(iK_\nu r) + B_\nu(t)\eta_n(iK_\nu r) \tag{5.11}$$

with

$$K_\nu = + \sqrt{4\pi i \omega \sigma_\nu} = (1+i)/p_\nu$$

as propagation constant and p_ν as skin-depth value of the ν^{th} shell; j_n and η_n denote spherical Bessel functions of the first and second kind of the order n (for the source field term P_n^m). Their definition in terms of modified Bessel functions and other useful relations can be found in Appendix II. The time functions A and B (the subscript n and the affix m are omitted for the sake of simplicity) correspond to E_n^m and I_n^m of the outside field with $\exp(i\omega t)$ as common time factor. We apply the differentiation formula of spherical Bessel functions and obtain

$$f'_\nu(t, r) = f_\nu(t, r) \cdot [rK_\nu G_\nu(r) - n] \tag{5.12}$$

with

$$G_\nu(r) = i \frac{A_\nu j_{n-1} + B_\nu \eta_{n-1}}{A_\nu j_n + B_\nu \eta_n} \tag{5.13}$$

and $(iK_\nu r)$ as common argument of the Bessel functions.

The surface ratio of internal to external parts is I_n^m/E_n^m for the tangential field components H_ϕ and H_θ and $-(n+1)\, I_n^m/(nE_n^m)$ for the radial component H_r, as readily inferred from (5.8). Setting

$$S_n^m = I_n^m/E_n^m \quad \text{and} \quad T_n^m = \frac{1 - S_n^m(n+1)/n}{1 + S_n^m}$$

yields in a similar way

$$H_r/H_\theta = \frac{nP_n^m}{dP_n^m/d\theta} \cdot T_n^m \quad \text{and} \quad H_r/H_\phi = \frac{n \sin\theta}{im} T_n^m \tag{5.14}$$

as surface ratio of radial to tangential variations.

Outside and inside field have to match at the surface of the conductor. Thus, by equating (5.8) and (5.9) for r = a we obtain in virtue of (5.12)

$$\begin{aligned} S_n^m &= \frac{n}{n+1}\left[1 - \frac{2n+1}{K_1 a G_1(a)}\right] \\ T_n^m &= (n+1)/[K_1 a G_1(a) - n] \end{aligned} \tag{5.15}$$

and express thereby these basic ratios in terms of the surface value of G(r).

The electric field vector in the ν^{th} shell which is responsible for the toroidal current mode has the tangential components

$$\left.\begin{aligned} \mathcal{E}_\theta &= - f_\nu(r,\ t)\ imP_n^m/\sin\theta \\ \mathcal{E}_\phi &= + f_\nu(r,\ t)\ dP_n^m/d\theta \end{aligned}\right\} \quad \exp(im\phi) \tag{5.16}$$

in accordance with the quasi-stationary approximation curl $\mathbf{F} = 4\pi\sigma\,\mathcal{E}$. This gives

$$\mathcal{E}_\phi/H_\theta = -\,\mathcal{E}_\theta/H_\phi = i\omega T_n^m \cdot \frac{a}{n+1} \tag{5.17}$$

as surface impedance of the incident field and

$$\begin{aligned} \frac{n+1}{a}\,\mathcal{E}_\phi &= \omega\,\frac{i dP_n^m/d\theta}{nP_n^m}\,H_r \\ \frac{n+1}{a}\,\mathcal{E}_\theta &= \omega\,\frac{m}{n\sin\theta}\,H_r \end{aligned} \tag{5.18}$$

as spherical version of (5.5).

It remains now to determine the radial function $G_\nu(r)$, in particular its surface value $G_1(a)$. The boundary condition at the inner surface of the ν^{th} layer requires that

$$K_\nu G_\nu(r_{\nu+1}) = K_{\nu+1} G_{\nu+1}(r_{\nu+1}).$$

This ensures that the ratio of radial to tangential field components passes without change from the ν^{th} into the underlying $(\nu+1)^{\text{th}}$ shell, thereby satisfying the continuity condition for the transient magnetic field vector.

From the definition of $G_\nu(r)$ in (5.13) it follows that we can express $G_\nu(r_{\nu+1})$ in terms of $G_\nu(r_\nu)$ at the outer surface of the same shell by eliminating the constant ratio B_ν/A_ν as given in equation 5.23. This leads to the basic recurrence formula for spherical conductors

$$G_\nu(r_\nu) = i\,\frac{P\eta_{n-1}(\nu,\nu) - Qj_{n-1}(\nu,\ \nu)}{P\eta_n(\nu,\ \nu) - Qj_n(\nu,\ \nu)} \tag{5.19}$$

$$P = K_\nu j_{n-1}(\nu,\ \nu+1) + ic_{\nu+1} j_n(\nu,\ \nu+1)$$

$$Q = K_\nu \eta_{n-1}(\nu,\ \nu+1) + ic_{\nu+1}\,\eta_n(\nu,\ \nu+1)$$

$$c_{\nu+1} = K_{\nu+1}\,G_{\nu+1}\,(r_{\nu+1})$$

with (a, b) as code for the argument $(iK_a r_b)$ of the Bessel functions. This is a condensed and simplified formulation of Srivastava's equation 18 (1966).

The general solution for the inner core does not contain spherical Bessel functions of the 2nd kind which would become infinite at $r = 0$. Hence, as readily seen from (5.13),

$$G_N(r) = i\,\frac{j_{n-1}(iK_N r)}{j_n(iK_N r)} \tag{5.20}$$

for $r \leq r_N$. The thus derived value $G_N(r_N)$ yields, when substituted in (5.19), $G_{N-1}(r_{N-1})$ and after $(N - 1)$ substitutions of this kind the desired surface value $G_1(a)$.

The following approximations can facilitate the numerical calculations. Suppose the skin-depth value of the ν^{th} shell is small in comparison to its inner radius, hence $|K_\nu r_{\nu+1}| \gg 1$. Using the pertinent approximations for spherical Bessel functions with large arguments gives

$$G_\nu(r_\nu) = 1 + 2 \cdot \frac{c_{\nu+1} - K_\nu}{c_{\nu+1} + K_\nu} \exp(-2K_\nu d) \tag{5.21}$$

when $d = r_\nu - r_{\nu+1}$ denotes the thickness of this highly conducting shell. If to the contrary, p_ν of a poorly conducting shell is much larger than its outer radius r_ν, then

$$G_\nu(r_\nu) = \frac{(2n+1)\,[K_\nu^2 r_{\nu+1}(1 - \rho^{2n-1}) + (2n-1)\,c_{\nu+1}]}{(2n-1)\,K_\nu[\rho^{2n}(2n+1) + r_\nu(1 - \rho^{2n+1})\,c_{\nu+1}]} \approx \frac{K_\nu^2 d + c_{\nu+1}}{K_\nu(1 + dc_{\nu+1})} \tag{5.22}$$

with $\rho = r_{\nu+1}/r_\nu$. The approximation applies to thin shells, when $d \ll r_\nu$. Equation 5.22 follows from the approximation for Bessel functions with small arguments.

Let us consider in conclusion the downward attenuation of the incident field by expressing the inside field components in terms of their surface values. It is then unnecessary to determine the inside coefficients $A_\nu(t)$ and $B_\nu(t)$ themselves, since only their ratio

$$B_\nu/A_\nu = \frac{G_\nu(r_\nu)\,j_n(\nu,\ \nu) - ij_{n-1}(\nu,\ \nu)}{i\eta_{n-1}(\nu,\ \nu) - G_\nu(r_\nu)\,\eta_n(\nu,\ \nu)} \tag{5.23}$$

enters into the following relation. Equation 5.23 follows readily from the definition of $G_\nu(r)$ in (5.13). We assume that $G(r)$ is known at all interfaces from the determination of its surface value $G_1(a)$ by successive substitution.

The radial magnetic component within the ν^{th} shell is readily expressed in terms of its value at the overlying interface, since

$$H_r(r)/H_r(r_\nu) = \frac{r_\nu\,[A_\nu j_n(iK_\nu r) + B_\nu \eta_n(iK_\nu r)]}{r[A_\nu j_n(\nu,\nu) + B_\nu \eta_n(\nu,\nu)]} \tag{5.24}$$

in virtue of (5.9) and (5.11). A corresponding relation applies to the tangential components of the electric field vector. Equation 5.24 can be evaluated with the aid of (5.23) and a repeated application of this formula, while moving upwards from interface to interface, yields the desired ratio according to

$$\frac{H_r(r)}{H_r(a)} = \frac{H_r(r)}{H_r(r_\nu)} \cdot \frac{H_r(r_\nu)}{H_r(r_{\nu-1})} \cdot \;\cdots\; \frac{H(r_2)}{H(a)}\,. \tag{5.25}$$

The corresponding relation for the tangential magnetic field components is readily found to be

$$\frac{H_\theta(r)}{H_\theta(a)} = \frac{H_\phi(r)}{H_\phi(a)} = \frac{H_r(r)}{H_r(a)} \cdot \frac{K_\nu G_\nu(r)\cdot r - n}{K_1 G_1(a)\cdot a - n} \tag{5.26}$$

in virtue of (5.12), where $G_\nu(r)$ can be derived from (5.13) in conjunction with (5.23).

5.3 Plane Conductors

Let a stratified conducting substratum occupy the lower half-space of rectangular coordinates, z down. It consists of N-plane layers of different conductivity, the last layer extending to infinity (fig. 29). A transient field shall be incident from above, passing through a nonconducting medium above the surface z = 0.

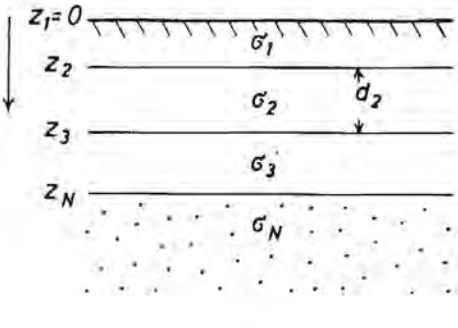

Fig. 29.

We may regard the conducting half-space as a sphere of infinite radius when we assume that the degree of the spherical functions P_n^m, describing the source field, tends likewise toward infinity. The ratio n/a remains finite and becomes the wave number k of the source field (eq. 5.2). Keeping this identity in mind the following relations agree closely with those for spherical conductors. To emphasize their correspondence we employ here similar notations as in section 5.2.

The transient magnetic field above the lower half-space is expressed as a continuous spectrum of plane waves, derivable as gradient from the scalar potential function

$$U(t,\ x,\ y,\ z) = \int_{-\infty}^{+\infty}\int_{-\infty}^{+\infty} \Big\{ E(\mathbf{k},\ t) \cdot \exp\left[i(\mathbf{k} \cdot \mathbf{r}) - kz \right] + I(\mathbf{k},\ t) \cdot \exp\left[i(\mathbf{k} \cdot \mathbf{r}) + kz \right] \Big\}\, dk_x dk_y \tag{5.27}$$

with

$$(\mathbf{k} \cdot \mathbf{r}) = k_x x + k_y y$$
$$k = +\sqrt{k_x^2 + k_y^2}.$$

The external and internal coefficients E and I are here continuous functions of the wave number k with $\exp(i\omega t)$ as time factor.

Considering a single wave component its rectangular field components at the surface of the substratum are given by

$$\left.\begin{aligned} X &= -ik_x(E + I) \\ Y &= -ik_y(E + I) \\ Z &= k(E - I) \end{aligned}\right\} \quad \exp\left[i(\mathbf{k} \cdot \bar{\mathbf{r}}) \right]. \tag{5.28}$$

For the field inside the ν^{th} layer we use in analogy to (5.9) the formulation

$$\left.\begin{aligned} X &= -ik_x f'_\nu(k,\ t,\ z) \\ Y &= -ik_y f'_\nu(k,\ t,\ z) \\ Z &= +k f_\nu(k,\ t,\ z) \end{aligned}\right\} \quad i/\omega \cdot \exp\left[i(\mathbf{k} \cdot \mathbf{r}) \right] \tag{5.29}$$

with

$$f'_\nu = -k^{-1} df_\nu / dz$$

and $f_\nu(k,\ t,\ z)$ being a solution of

$$\frac{d^2 f_\nu}{dz^2} - (k^2 + 4\pi i \omega \sigma_\nu) f_\nu = 0 \tag{5.30}$$

in lieu of (5.10). After introducing

$$K_\nu = +\sqrt{k^2 + 4\pi i \omega \sigma_\nu} = \sqrt{\frac{r + k^2}{2}} + i\sqrt{\frac{r - k^2}{2}} \tag{5.31}$$
$$r^2 = k^4 + (4\pi\omega\sigma_\nu)^2$$

as propagation constant of the downward diffusing field in the ν^{th} layer we obtain

$$f_\nu(k,\ t,\ z) = A_\nu(k,\ t) \cdot \exp(-K_\nu z) + B_\nu(k,\ t) \cdot \exp(K_\nu z) \tag{5.32}$$

as general solution of (5.30), yielding

$$f'_\nu = f_\nu K_\nu G_\nu(z)/k \tag{5.33}$$

with

$$G_\nu(z) = \frac{A_\nu e^{-K_\nu z} - B_\nu e^{K_\nu z}}{A_\nu e^{-K_\nu z} + B_\nu e^{K_\nu z}} \quad . \tag{5.34}$$

Let us consider two limiting cases. When the skin-depth value of the ν^{th} layer is large in comparison to the wave length of the source field, yielding $p_\nu k \gg 1$, then

$$K_\nu \approx k \tag{5.35}$$

and the incident field penetrates through this layer as if it were nonconducting. When, to the contrary, $p_\nu k \ll 1$, then

$$K_\nu = (1+i)/p_\nu \, , \tag{5.36}$$

i.e., the attenuation of the incident field within this layer is determined solely by its skin-depth value and is independent of k.

The surface ratio of internal to external parts is the same for vertical and horizontal variations and given by

$$S(k) = I(k,t)/E(k,t) = \frac{K_1 G_1(0) - k}{K_1 G_1(0) + k} \tag{5.37}$$

as is readily inferred from the continuity condition for the horizontal plane $z = 0$. We consider X and Y as components of a horizontal variation vector **H**, setting

$$X = k_x/k \cdot H \qquad\qquad Y = k_y/k \cdot H \, . \tag{5.38}$$

The ratio of vertical to horizontal variations follows then from (5.28) as

$$Z/H = iT(k) \tag{5.39}$$

with

$$T(k) = \frac{1 - S(k)}{1 + S(k)} = \frac{k}{K_1 G_1(0)} \quad .$$

The internal electric field vector of the associate toroidal current mode has the components

$$\begin{aligned} \mathcal{E}_x &= k_y/k \cdot \mathcal{E} \qquad\qquad \mathcal{E}_y = -k_x/k \cdot \mathcal{E} \\ \mathcal{E} &= if_\nu(k,\ t,\ z)\ \exp[i(k \cdot r)] \end{aligned} \tag{5.40}$$

for the quasi-stationary approximation. It is orthogonal to $\bar{H}$ and yields in combination with (5.29) and (5.32)

$$\mathcal{E}/H = i\omega T(k)/k = \frac{i\omega}{K_1 G_1(0)} \tag{5.41}$$

as surface impedance for $z = 0$.

The spatial gradients of the horizontal variation field are for $z = +0$

$$\frac{\partial X}{\partial x} + \frac{\partial Y}{\partial y} = ikH \qquad \frac{\partial H}{\partial z} = -\frac{K_1}{G_1(0)} \cdot H$$

as seen from (5.28) and (5.38). This leads in conjunction with (5.39) and (5.41) to the useful relations

$$\frac{\partial X}{\partial x} + \frac{\partial Y}{\partial y} = K_1 G_1(0) \cdot Z \text{ and } \frac{\partial H}{\partial z} = K_1^2 \mathcal{E} \cdot \frac{i}{\omega} . \tag{5.42}$$

In order to determine the yet unknown vertical function $G(z)$ we proceed similarly as in section 5.2 The continuity condition for the transient magnetic field vector at the interface $z = z_{\nu+1}$ is satisfied when

$$K_\nu G_\nu(z_{\nu+1}) = K_{\nu+1} G_{\nu+1}(z_{\nu+1}) .$$

We have here the advantage that exponential functions with positive and negative arguments can be combined to hyperbolic functions and it is readily verified from (5.34) that

$$G_\nu(z) = \frac{G_\nu(z_\nu) - \tanh\left[K_\nu(z - z_\nu)\right]}{1 - G_\nu(z_\nu)\tanh\left[K_\nu(z - z_\nu)\right]} \tag{5.43}$$

for $z_\nu \le z \le z_{\nu+1}$. Setting $z = z_{\nu+1}$ yields $G_\nu(z_{\nu+1})$ in terms of $G_\nu(z_\nu)$ which when inserted above leads to the basic recurrence formula for plane conductors

$$G_\nu(z_\nu) = \frac{c_{\nu+1} + K_\nu \tanh(K_\nu d_\nu)}{K_\nu + c_{\nu+1} \tanh(K_\nu d_\nu)} ; \tag{5.44}$$

$d_\nu = z_{\nu+1} - z_\nu$ denotes the thickness of the νth layer and

$$c_{\nu+1} = K_{\nu+1} G_{\nu+1}(z_{\nu+1}) .$$

Equation 5.44 corresponds to equation 9 in Wait's publication (1953).

Since the incident field disappears at great depth, the general solution (5.32) for the ultimate layer, extending to infinity, cannot contain the B-term. Thus,

$$G_N(z) = 1 \tag{5.45}$$

for $z \geq z_N$. We can solve now equation 5.44 by successive substitution, beginning with $G_N(z_N) = 1$ and ending with $G_1(0)$ at the surface.

When the skin-depth value of the ν^{th} layer is small in comparison to its thickness, yielding $|K_\nu d| \gg 1$, we may set

$$G_\nu(z_\nu) = 1 + 2 \cdot \frac{c_{\nu+1} - K_\nu}{c_{\nu+1} + K_\nu} \exp(-2K_\nu d_\nu) \tag{5.46a}$$

since $\tanh(x) \approx 1 - 2 \cdot \exp(-2x)$ for large arguments. This implies that the incident field hardly penetrates through this layer at all. If, on the other hand, $d \ll p \ll k^{-1}$, we may set $\tanh(x) \approx x$ and obtain

$$G_\nu(z_\nu) = \frac{c_{\nu+1} + K_\nu^2 d_\nu}{K_\nu(1 + c_{\nu+1} d_\nu)} \; . \tag{5.46b}$$

Notice that these approximations are the same as in the case of spherical shells.

We consider now the downward attenuation of the incident field and have here in analogy to (5.24)

$$Z(z)/Z(z_\nu) = \frac{A_\nu \exp(-K_\nu z) + B_\nu \exp(K_\nu z)}{A_\nu \exp(-K_\nu z_\nu) + B_\nu \exp(K_\nu z_\nu)}$$

for point in the ν^{th} layer. From (5.34) it follows that

$$B_\nu / A_\nu = \frac{1 - G_\nu(z_\nu)}{1 + G_\nu(z_\nu)} \exp(-2K_\nu z_\nu)$$

which when inserted above yields for $z_\nu \leq z \leq z_{\nu+1}$

$$\frac{Z(z)}{Z(z_\nu)} = \cosh[K_\nu(z - z_\nu)] - G_\nu(z_\nu) \sinh[K_\nu(z - z_\nu)] . \tag{5.47}$$

A repeated evaluation of this formula allows us to derive the inside field components in terms of their surface values according to

$$\frac{Z(z)}{Z(o)} = \frac{Z(z)}{Z(z_\nu)} \cdot \frac{Z(z_\nu)}{Z(z_{\nu-1})} \cdot \cdots \frac{Z(z_2)}{Z(o)}$$

$$\frac{\mathcal{E}(z)}{\mathcal{E}(o)} = \frac{Z(z)}{Z(o)} \quad \text{and} \quad \frac{H(z)}{H(o)} = \frac{Z(z)}{Z(o)} \cdot \frac{K_\nu}{K_1} \frac{G_\nu(z)}{G_1(o)} \; . \tag{5.48}$$

The last relation follows directly from (5.33) and $G_\nu(z)$ can be inferred from (5.43). Figures 1 and 49 give examples for the thus determined attenuation of an incident variation field within multilayered conductors.

5.4 Special Case I: Uniform Conductor

Consider as the most simple case a uniform sphere of radius a and conductivity σ. Setting $G_1 = G_N$ in equation 5.15 yields in conjunction with (5.20)

$$S_n^m = \frac{n}{n+1}\left[1 - \frac{(2n+1)\cdot j_n(iKa)}{iaK \cdot j_{n-1}(iKa)}\right] \qquad (5.49)$$

$$K = (1+i)\sqrt{2\pi\omega\sigma}$$

(eqs. 36 and 57 in chap. 22 of Geomagnetism) as ratio of the internal to external part for the source field term P_n^m. If $|K \cdot a| \gg 1$ and therefore $j_n \approx i \cdot j_{n-1}$ (App. II), we obtain

$$S_n^m = \frac{n}{n+1}\left[1 - \frac{1-i}{\eta_n}\right] \qquad (5.50)$$

with

$$\eta_n = \frac{2a}{2n+1}\sqrt{2\pi\omega\sigma}$$

as induction parameter for uniform spheres. This is a very useful approximation of S_n^m near the inductive limit, when the wave length L of the incident field is large in comparison to the skin-depth value of the sphere (cf. eqs. 5.1 and 5.2).

The attenuation of the incident field within the sphere is governed by

$$j_n(iKr)/j_n(iKa) \approx a/r \cdot \exp[K(r-a)]$$

as seen from (5.24). The approximation applies again near the inductive limit, when the modulus of the argument of the Bessel functions is large against unity (App. II).

Turning to a uniform plane conductor we get with $G_1 = 1$ from (5.37)

$$S(k) = 1 - 2k/(K+k) \qquad (5.51)$$

$$K^2 = 4\pi i\omega\sigma + k^2$$

(eq. 9.8 in Price, 1950) or

$$S(k) = 1 - 2/\left[1 + i\eta(k) + \sqrt{1+\eta^2(k)}\right]$$

with

$$\eta(k) = \sqrt{(|K|^2 - k^2)/2k^2}$$

as induction parameter for the half-space. This reduces near the inductive limit, when $k \cdot p \ll 1$, to

$$S(k) = 1 - \frac{1 - i}{\eta(k)}$$
$$\eta(k) = \sqrt{2\pi\omega\sigma}/k \; . \qquad (5.51a)$$

The downward diffusing field disappears with $\exp(-Kz)$ as in the case of spheres.

The inductive response of uniform conductors is most readily inferred from induction curves (Kertz, 1960), i.e., from plots of S_n^m or S(k) versus the induction parameters η_n and $\eta(k)$ as shown in figure 30. Notice that these parameters represent the ratio of spatial wave length to skin-depth value. The resulting curves merge for $\eta > 3$ into the above approximations, i.e., we may relinquish the distinction between spherical and plane conductors near the inductive limit. We observe that the internal part ascends from zero to its upper inductive limit within roughly one order of magnitude of η.

A numerical example may illustrate the induction by geomagnetic bays (a = 6400 km, f = 1 cph, n = 4). Inserting these values in (5.50) and measuring σ in $[\Omega \cdot m]^{-1}$ gives $\eta = 47 \cdot \sqrt{\sigma}$. Hence, the internal part of the "normal" bay field would be close to its upper inductive limit, when σ exceeds 0.004 as is certainly the case within the upper 200 km of the earth's interior.

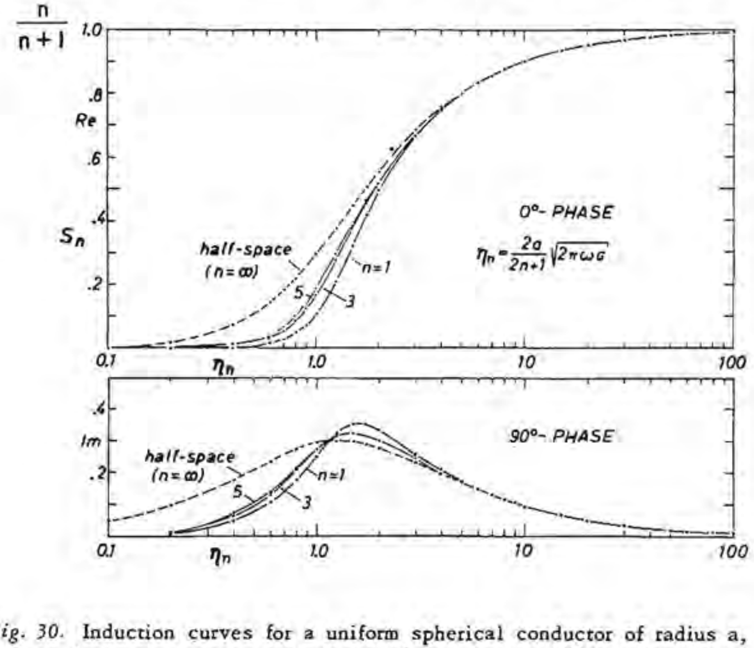

Fig. 30. Induction curves for a uniform spherical conductor of radius a, shown for various degrees n, when a spherical surface harmonic P_n^m describes the source field configuration.

5.5 Special Case II: 2-layer Model

Suppose a uniform plane substratum of the conductivity σ_c is covered by a poorly conducting top layer, extending from $z_1 = 0$ to $z_2 = h$. We assume that the incident variation field penetrates through this layer with negligible attenuation for the frequencies considered here, while its depth of penetration in the underlying substratum shall be small in comparison to its spatial wave length $2\pi/k$. Using the pertinent approximations from (5.35/6) we set

$$K_1 = k \qquad kh \ll 1 \text{ and } K_2 = (1+i)/p_c \qquad p_c = [2\pi\omega\sigma_c]^{-1/2},$$

which when inserted in (5.46b) yield with $c_2 = K_2$

$$G_1(o) = \frac{K_2}{k(1+K_2h)} = \frac{1}{kc} \ . \qquad (5.52)$$

The thus defined complex-valued parameter

$$c = h + \frac{1}{2}p_c - i\,\frac{1}{2}p_c \qquad (5.53)$$

(a length) determines as function of frequency surface impedance and relative magnitude of vertical variations. Since T(k) from (5.39) becomes simply $(k \cdot c)$, we obtain from (5.39, 41, 42)

$$\begin{aligned} \mathcal{E}/H &= i\omega c \\ Z/H &= ikc \\ Z &= c[\,\partial X/\partial x + \partial Y/\partial y] \ . \end{aligned} \qquad (5.54)$$

Reversely, when any of these ratios has been observed for a permissible frequency, depth and conductivity of the substratum are determined uniquely; for example,

$$\begin{aligned} h &= \omega^{-1}[\mathrm{Im}(\mathcal{E}/H) - \mathrm{Re}(\mathcal{E}/H)] \\ \rho_c &= \omega^{-1} \cdot 2\,\mathrm{Re}(\mathcal{E}/H) \ . \end{aligned} \qquad (5.55)$$

Notice that the arguments of the ratios $\mathcal{E}/H$ and Z/H vary between $\frac{1}{4}\pi$ above a uniform conductor at zero depth and $\frac{1}{2}\pi$ above a perfect conductor at any permissible depth.

The real part of c as inferred from the out-of-phase components of $\mathcal{E}/H$ or Z/H reflects the mean depth of the internal eddy currents, while the imaginary part of c as inferred from the in-phase components of $\mathcal{E}/H$ or Z/H indicates with p_c the ambient conductivity at that depth. We shall refer henceforth to

$$h^* = h + \frac{1}{2}\,p_c \qquad (5.56)$$

as "depth of a perfect substitute conductor."

5.6 Direct Inversion of Surface Observations

The inversion of the previous section can be generalized as follows. Suppose the impedance or the Z/H ratio above a multilayered substratum has been observed or calculated. We apply (5.55) to these ratios and obtain for each resolved frequency component depth and conductivity of a uniform substitute conductor. This substitution is meaningful only when the arguments of the ratios lie between $\frac{1}{4}\pi$ and $\frac{1}{2}\pi$, thereby yielding a positive depth h. A multilayered substratum is in that case indistinguishable from and therefore replaceable by a uniform conductor at the depth h, as far as its response to a single frequency component of the incident variation field is concerned. It is presumed, of course, that $(h + p_C)$ is small against the wave length of the source field. Cf. p. 108 for an extension to spherical conductors.

The depth h^* from (5.56), however, is always positive or zero, since the arguments of $\mathcal{E}/H$ and Z/H cannot be smaller than zero. Hence, we can interpret the out-of-phase component of any given ratio $\mathcal{E}/H$ or Z/H in terms of a perfect substitute conductor at the depth

$$h^* = \omega^{-1}\,\mathrm{Im}(\mathcal{E}/H) \qquad (5.57a)$$

while the in-phase component yields in p_c the apparent conductivity

$$\sigma_c = \omega\left\{8\pi[\mathrm{Re}(\mathcal{E}/H)]^2\right\}^{-1} \qquad (5.57b)$$

at that depth. Plots of h^* versus σ_c for a number of different frequencies represent good approximations of the true conductivity distribution as demonstrated in figure 31.

Cagniard's (1953) definition of the "apparent resistivity" which is commonly used in this context is based on the modulus of the impedance. It would yield as apparent skin-depth value the modulus of $c\sqrt{2}$, while the parameters h^* and σ_c as defined above give proper regard to the in-phase and out-of-phase component of the impedance.

5.7 Special Case III: Limitations of Price's Method

Repeated use will be made of Price's method when dealing with the induction in thin sheets or shells (cf. sec. 1.2). This method becomes inadequate (a) when the skin-depth value of the sheet is equal to or even smaller than its thickness, and (b) when the sheet is underlain at shallow depth by a good conductor. In both cases the tangential electric field is distinctly attenuated within the sheet and the integration of equation 1.8 cannot be carried out with $\mathcal{E}$ as a constant. Since the terrestrial surface layers, to which this method will be applied, are indeed underlain at some depth by highly conductive mantle material, such limitations for Price's method deserve careful consideration.

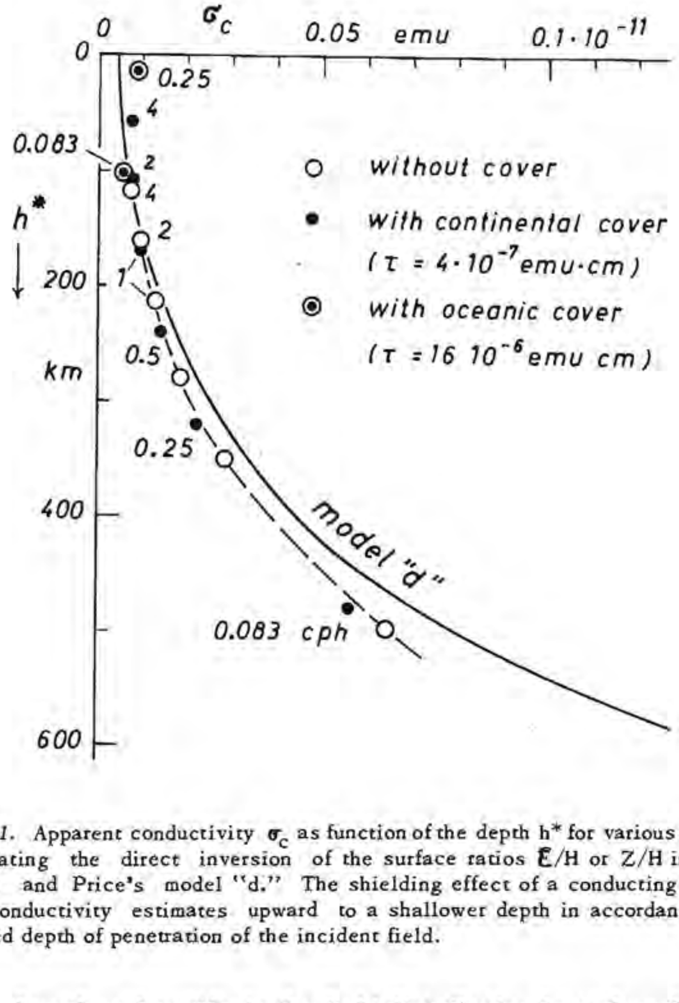

Fig. 31. Apparent conductivity σ_c as function of the depth h^* for various frequencies, illustrating the direct inversion of the surface ratios $\mathcal{E}/H$ or Z/H in the case of Lahiri and Price's model "d." The shielding effect of a conducting cover moves the conductivity estimates upward to a shallower depth in accordance with the reduced depth of penetration of the incident field.

Let us therefore investigate the field distribution in a plane 3-layer model, consisting of a top layer of the thickness d (terrestrial surface layers), a poorly conducting intermediate layer of the thickness h (high resistivity zone of the crust and uppermost mantle), and a highly conducting substratum from $z = h + d$ downward to infinity (fig. 32). The attenuated electric field at the bottom of the top layer is, in virtue of (5.47/48),

$$\mathcal{E}(d)/\mathcal{E}(0) = \cosh(K_1 d) - G_1(0)\sinh(K_1 d) .$$

Let us use the following approximations:

$$K_1 \approx (1+i)/p_1, \;\; K_2 \approx k, \;\; K_3 \approx (1+i)/p_3 .$$

Furthermore, h shall be small compared to the wave length of the source field, yielding $k \cdot h \ll 1$, but large in comparison to the skin-depth value p_3 of the substratum. This ensures that the wave number k of the incident field drops out of the following relations.

The application of the recurrence formula (5.44) gives

$$G_2(d) \approx (kh)^{-1}$$

$$G_1(0) = \frac{1 + K_1 h \tanh(K_1 d)}{K_1 h + \tanh(K_1 d)}$$

which when substituted above yields

$$\frac{\mathcal{E}(d)}{\mathcal{E}(0)} = \frac{K_1 h}{K_1 h \cosh(K_1 d) + \sinh(K_1 d)} \approx 1 - \frac{d}{h + d} . \qquad (5.58)$$

The approximation becomes valid when p_1 is about three times the thickness d as seen from the asymptotic behavior of the curves in figure 32. Hence, a finite ratio d/h limits the uniformity of $\mathcal{E}$ in the top layer even for those frequencies, for which $p_1 \gg d$. We infer from (5.58) and figure 32 that $\mathcal{E}$ remains uniform within d/(h + d) percent as long as $p_1 > 3d$, thereby setting limits for Price's method.

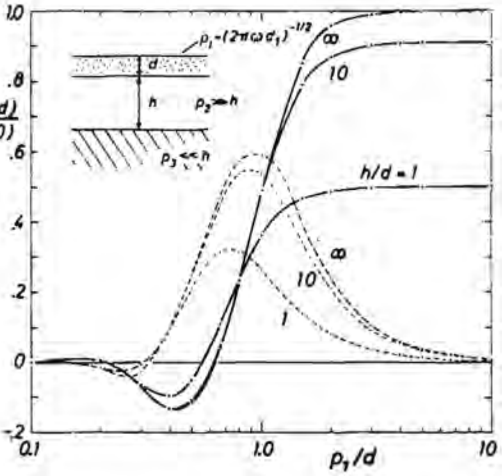

Fig. 32. Attenuation of tangential electric field variations $\mathcal{E}(z)$ within the top layer of a special 3-layer model, shown as function of skin-depth value to thickness of the top layer. Solid curves: real part of $\mathcal{E}(d)/\mathcal{E}(0)$; dashed curves: imaginary part.

Consider, for instance, the induction in a 4 km deep ocean ($\sigma_1 = 4 \cdot 10^{-11}$ emu) above a highly conducting mantle at 100 km depth. The attenuation of $\mathcal{E}$ within this ocean would be 4% as long as p_1 is greater than 12 km, yielding 1.6 cph as upper permissible frequency for Price's method.

Let us consider in conclusion the attenuation of the magnetic variation field in the top layer and the impedance values for $z = 0$ and $z = d$. If we insert $G_1(0)$ from above in (5.48) and (5.47) we obtain (cf. fig. 33)

$$H(d)/H(0) = [\cosh(K_1 d) + K_1 h \cdot \sinh(K_1 d)]^{-1} \approx (1 + i\eta_s)^{-1}$$

$$\mathcal{E}(0)/H(0) = i\omega/[K_1 G_1(0)] \approx i\omega(h+d)/(1+i\eta_s) \qquad (5.58a)$$

$$\mathcal{E}(d)/H(d) = i\omega/[kG_2(d)] = i\omega h$$

with

$$\eta_s = 4\pi\,\omega\,\sigma_1 dh\,.$$

The approximations refer again to the case of a poorly conducting top layer, so that $p_1 > 3 \cdot d$; η_s will return in the next section as induction parameter for shell-core models.

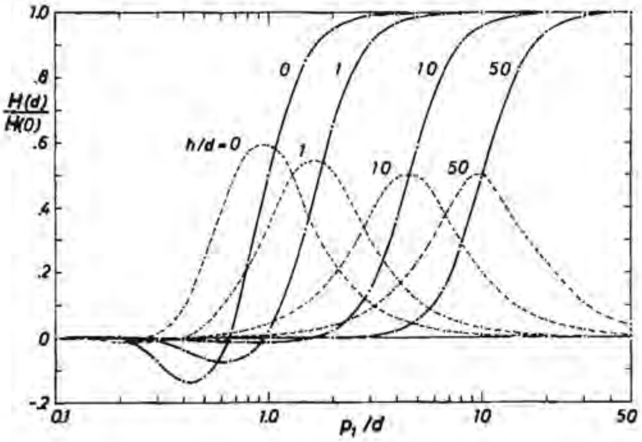

Fig. 33. Attenuation of tangential magnetic field variations H(z) within the top layer of the 3-layermodel of figure 32. Notice the range of p_1/d and $d \ll h$ for which the attenuation of H(z) is almost complete, while $\mathcal{E}(z)$ is still unattenuated (cf. legend of fig. 32).

5.8 Shell-core and Sheet-substratum Models

Let the spherical conductor consist of a thin outermost shell of radius A and with $\tau = d \cdot \sigma_s$ as total conductivity, a layered conducting core of radius a, and a nonconducting intermediate layer between shell and core (fig. 34). The classical treatment of this model is due to Chapman and Whitehead (1923) who wanted to estimate the possible effect of oceans upon the internal part of transient geomagnetic variations. They found that a uniform ocean of moderate depth, say, 1 km, would have a marked effect upon the internal part even of relatively slow variations. In reality, of course, the large-scale flow of oceanic induction currents is broken up by the continents and therefore less effective. The following calculations have been carried out on the basis of Price's method. Hence, attention should be given to the limitations, which were stated in the previous section.

The magnetic variation field of the source field term P_n^m above the shell $(r \geq A)$ may be expressed as gradient of

$$U^+ = A \left\{ E \cdot (r/A)^n + (I_s + I_c)(A/r)^{n+1} \right\} P_n^m(\cos\theta) \exp(im\phi) \qquad (5.59a)$$

in analogy to equation 5.6. The two internal coefficients I_s and I_c (the subscript n and the affix m have been omitted) refer to fields from induction currents in shell (I_s) and core (I_c). Let

$$U^- = A \left\{ (E - \frac{n+1}{n} I_s) \cdot (r/A)^n + I_c(A/r)^{n+1} \right\} P_n^m(\cos\theta) \exp(im\phi) \qquad (5.59b)$$

be the potential of the variation field in the nonconducting intermediate layer $(a \leq r \leq A)$. This formulation ensures (a) the required continuity of the radial field component at $r = A$ and (b) the downward decrease of the internal field associated with shell-induction currents.

Price's boundary condition (1.11) for $r = A$ requires that

$$\nabla^2(U^+ - U^-) = -4\pi i\,\omega\tau \cdot \partial U/\partial r$$

where the left-hand side reduces to

$$-A^{-1}(2n+1)(n+1) I_s P_n^m(\cos\theta)\exp(im\phi)$$

in virtue of the pertinent properties of spherical functions. Primary field and induced field from the shell form jointly the "external" incident field for the core. Hence, the ratio of external to internal parts on the surface of the core $(r = a)$ is given by

$$S_c = I_c \cdot \rho^{-2n-1}/(E - \frac{n+1}{n} I_s)$$

with $\rho = a/A$. Combining the boundary conditions of $r = A$ and $r = a$ leads to

$$I_s/E = \frac{n}{n+1} \; \frac{i\eta_s}{1 + i\eta_s}$$
$$I_c/E = S_c \cdot \frac{\rho^{2n+1}}{1 + i\eta_s} \qquad (5.60)$$

as basic formulae for the shell-core induction with

$$\eta_s = \frac{4\pi\omega\tau A}{2n+1}\,(1 - \frac{n+1}{n} S_c \cdot \rho^{2n+1})$$

as pertinent induction parameter. The still undetermined ratio S_c has to be found separately from (5.15) for a given distribution of conductivity in the core.

When $|\eta_s| \ll 1$, the incident field penetrates through the shell with negligible attenuation and the internal part (if any) arises from induction currents in the core. If to the contrary $|\eta_s| \gg 1$, the incident field is effectively shielded from the core by eddy currents in the shell. Notice that the expression in parenthesis controls the inductive couple between shell and core, approaching unity in the case of negligible coupling with a poorly conducting or small core.

Suppose the induction in the core is close to its inductive limit, so that the core can be represented by a uniform conductor (sec. 5.6) at a certain depth $h = A - a'$. Inserting for S_c the approximation (5.50) and developing $(a'/A)^{2n+1}$ into a series yields

$$\eta_s = 4\pi\omega\tau\left[h\left(1 - \frac{nh}{A} \pm \cdots\right) + \frac{p_c}{1+i}\left(1 - \frac{[2n+1]\cdot h}{A} \pm \cdots\right)\right] \qquad (5.61)$$

or when we disregard the "source field terms" nh/A

$$\eta_s = 4\pi\omega\tau(h + p_c/2 - ip_c/2) = 4\pi\omega\tau c \qquad (5.62)$$

with c as complex-valued length from (5.53).

The integrated current density in the shell is proportional to $I_s(2n+1)$ as seen from (5.59) in conjunction with (1.9). The normalized current density which is here of particular interest follows as

$$\frac{4\pi j}{H} = \frac{i\eta_s}{i\eta_s + \frac{n+1}{2n+1}(1 + S_c\rho^{2n+1})} \qquad (5.63)$$

where $H = H^+$ denotes the tangential magnetic variations at the outer surface of the shell, **H** being orthogonal to **j**. In the case of a highly conducting core at shallow depth ($S_c \approx n/(n+1)$ and $\rho \approx 1$) we obtain

$$\frac{4\pi j}{H} = \frac{i\eta_s}{1 + i\eta_s} \qquad (5.64)$$

as source-field free approximation of (5.63), using η_s from (5.62). This demonstrates that the relative strength and phase of the shell currents is controlled by the inductive couple with the core which is contained in the factor c of η_s.

Consider, for instance, as primary field the 2nd time harmonic of diurnal variations during the equinoxes, sweeping with $P_3^2(\cos\theta)$ as colatitude dependence over a uniform ocean of 4 km depth, which is underlain at 600 km depth by a perfectly conducting mantle ($A = 6400$ km, $f = 1/12$ cph, $n = 3$, $\tau = 16 \cdot 10^{-6}$ emu · cm, $S_c = 3/4$, $\rho = 58/64$). Inserting this in (5.60) gives $\eta_s = 1.33$ which means that the surface field of oceanic eddy currents would outweigh slightly the field from deep induction currents in the mantle. Without the dampening effect of a core ($\rho = 0$) we would have obtained $\eta_s = 2.67$.

We infer from (5.60) that the internal shell term I_s leads in phase relative to the external term E by $\tan^{-1}[1/\eta_s]$, while the corresponding core term I_c lags in phase by $\tan^{-1}\eta_s$, when S_c is close to its upper real limit. Thus, induction anomalies which originate from nonuniformities in the shell will lead in phase relative to those of deep origin (cf. fig. 35).

Figure 34 illustrates the complexity of the mutual dependence of shell and core induction. The induction curves for $\eta_n = 0$ refer to a shell without core. With increasing conductivity of the core the curves are shifted toward higher values of the shell-induction parameter, which implies that higher conductivities in the shell are needed to produce the same induced field from the shell (= dampening effect of the core). For $\eta_n = \infty$ the ultimate curves for a perfect conductor at the indicated depth are reached. We see that the core induction is suppressed at the same rate as the shell induction is built up (= shielding effect of the shell); I_s and I_c preserve their characteristic opposite arguments except for small values of η_n and $4\pi\omega\tau A$.

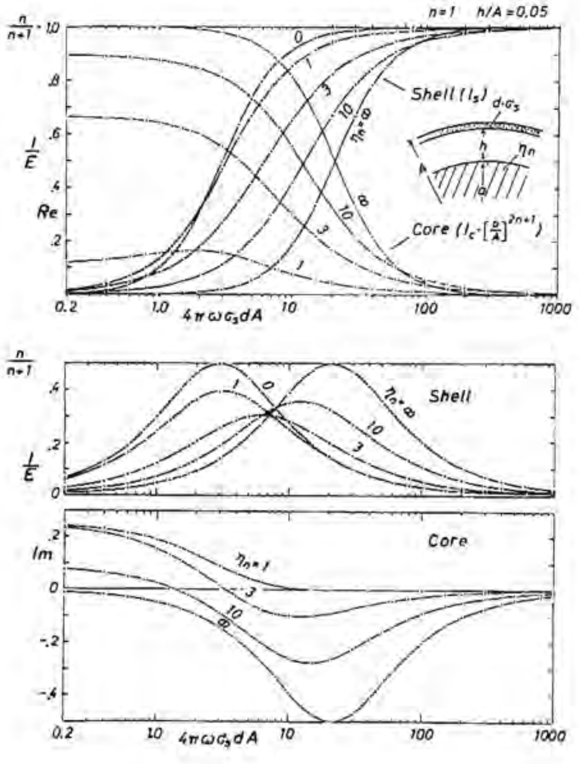

Fig. 34. Induction curves for a special shell-core model, shown for various induction parameters η_n of the uniform core. Upper diagram: in-phase components of the internal part, shown separately for shell and core induction in accordance with equation 5.60. Lower diagram: out-of-phase components of the internal part.

The induction in a plane sheet-substratum model is governed by very similar relations. Considering a wave component with the wave number k we have in analogy to (5.60)

$$I_s/E = i\eta_t/(1 + i\eta_t) \qquad I_c/E = S_c(k)/(1 + i\eta_t)$$
$$\eta_t = \frac{2\pi\omega\tau}{k}[1 - S_c(k) \cdot \exp(-2kh)] \tag{5.65}$$

where h denotes the depth of the substratum and η_t the pertinent induction parameter. In the case of a highly conducting substratum at shallow depth $(k \cdot h \ll 1)$ we may insert for $S_c(k)$ the approximation (5.52) and obtain for η_t the same approximation (5.62) as for the spherical parameter η_s.

6. ELECTROMAGNETIC INDUCTION IN NONUNIFORM CONDUCTORS

6.1 Introduction

This chapter deals with the effect of lateral nonuniformities upon the induced surface field of geomagnetic variations. The arising induction problem has been considered by various authors, beginning with Ertel's (1932) and Price's (1949) basic articles on this subject. Further references can be found in Rikitake's (1966) monograph.

The following treatment is restricted to 2-dimensional nonuniformities and the curvature of the earth's surface is neglected within the range of the anomaly of geomagnetic variations. Let this surface be the horizontal plane $z = 0$ of Cartesian coordinates, z down and y perpendicular to grad σ. The x- and z-component of the internal eddy currents will not contribute to the induction anomaly of the poloidal magnetic mode (cf. sec. 1.2). Hence, no anomalous behavior will be associated with the y-component of the normal variation field.

Denoting the horizontal x-component of the transient magnetic field vector with H and its vertical component with Z we express their anomalous parts throughout this chapter in the standard form

$$\begin{aligned} H_a &= h_H \cdot \overline{H} + h_Z \cdot \overline{Z} \\ Z_a &= z_H \cdot \overline{H} + z_Z \cdot \overline{Z} \end{aligned} \qquad (6.1)$$

with $\exp(i\omega t)$ as time factor on both sides. Each frequency component of the induction anomaly will be considered separately.

We distinguish three types of anomalies as shown schematically in figure 35. Surface anomalies are due to superficial conductivity variations above the crystalline basement, including the outstanding conductivity contrast of seawater and rock formations on land. Deep anomalies reflect conductivity imbalances in the upper mantle, and intermediate anomalies are connected with insulated conductors in the high-resistivity zone of the earth's crust and uppermost mantle.

Intermediate anomalies are the most unlikely type to occur as shown in section 6.4. Hence, those anomalies which are not explicable as surface effects on the basis of a probable near-surface conductivity distribution are presumably of deep origin.

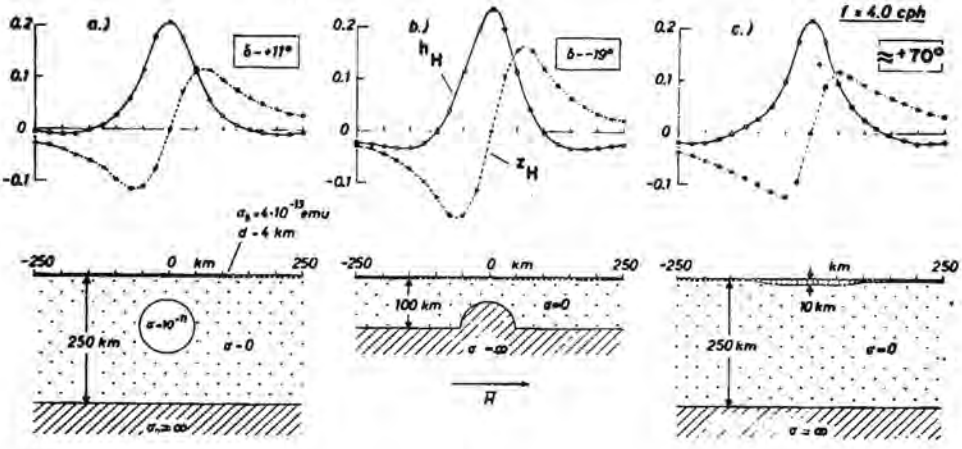

Fig. 35. Induction anomalies (a) above a conducting cylinder in the nonconducting intermediate zone, (b) above a semicylindrical elevation in the surface of a perfectly conducting plane substratum, (c) above a slab of increased total conductivity at the surface. The parameters of the three models have been chosen so as to yield comparable amplitudes of the anomalous parts in Z and H for f = 4 cph, when a continental surface cover is used. The surface anomaly (c) is distinguished by the large phase lead δ of Z_a and H_a relative to $\bar{H}$, reflecting the large phase lead of superficial induction currents in these models. For method of calculations see sec. 6.4 (a), equation 6.28 (b), sec. 6.3 (c).

6.2 Surface Anomalies

Consider a nonuniform thin sheet of the variable total conductivity

$$\tau(x) = \bar{\tau} + \tau_a(x) \tag{6.2}$$

in the z = 0 plane and a stratified conductivity distribution beneath it (fig. 36). Surface sheet and substratum are separated by an insulating layer, so that no current can enter or leave the sheet. Sheet and substratum are exposed to a time-varying source field from above and Price's boundary condition for the anomalous part of the variation field just above (+) and below (-) the sheet requires that

$$\frac{d}{dx}(H_a^+ - H_a^-) - (H^+ - H^-)\cdot\frac{1}{\tau}\frac{d\tau}{dx} = 4\pi i\omega[\bar{\tau} Z_a + \tau_a Z] \ . \tag{6.3}$$

This is the 2-dimensional version of equation 1.12 in section 1.2.

Let $\bar{j}$ be the y-component of the normally induced sheet-current density for $\tau_a = 0$. It will be denoted henceforth in the normalized form

$$Q = 2\pi\bar{j}/\bar{H}^+ = \frac{1}{2}(\bar{H}^+ - \bar{H}^-) \tag{6.4}$$

for which we know already from (5.64) the convenient approximation

$$2Q = i\eta_s/(1 + i\eta_s) \tag{6.5}$$

in terms of the pertinent induction parameter η_s.

The superimposed anomalous part of the induced sheet-current density is given by $j_a = (H_a^+ - H_a^-)/4\pi$. It will be expressed in terms of two linear transfer functions as

$$2\pi j_a = q_H \cdot \overline{H} + q_Z \cdot \overline{Z} . \tag{6.6}$$

We observe that q_H and the associate transfer functions h_H, z_H reflect the rearrangement of the normally induced sheet current $\overline{J}$ within nonuniform zones $\tau_a \neq 0$: anomalies of the 1st kind. Anomalies of the 2nd kind arise from a superimposed anomalous induction with $\overline{Z}$ as driving force and they are described by q_Z, respectively h_Z and z_Z.

Price's boundary condition from above becomes with the notations of (6.1) and (6.6)

$$\begin{aligned} \frac{d}{dx}\left([Q + q_H]/\tau\right) &= 2\pi i\omega z_H \\ \frac{d}{dx}(q_Z/\tau) &= 2\pi i\omega (z_Z + \tau_a/\tau) \end{aligned} \tag{6.7}$$

when written separately for anomalous variations of the 1st and 2nd kind.

6.3 Relaxation Method for Surface Anomalies

Suppose an anomaly of geomagnetic variations has been observed in an area where the conductivity distribution near the surface is well-known, for example from magnetotelluric observations or resistivity measurements. To be determined is the induced field above these layers. The stratified deep conductivity structure enters into the calculations as free parameter which can be adjusted so as to yield the best possible fit with the observed anomaly if such a fit is possible at all without assuming an unequal deep conductivity distribution.

Price (1949; secs. 12 and 13) suggested two approximation methods to solve the arising induction problem. First approximations are obtained by neglecting either self-inductance or Ohm's resistance. Both methods are complementary, i.e., when the first method does not lead to converging approximations, then the second will.

The relaxation process will be carried out separately for anomalous variations of the 1st and 2nd kind. The pertinent boundary conditions (6.7) can be integrated in closed form and yield

$$\begin{aligned} q_H(x) &= Q \cdot \tau_a(x)/\overline{\tau} + 2\pi i\omega\tau(x)\int_{x_0}^{x} z_H(\xi)\,d\xi \\ q_Z(x) &= 2\pi i\omega\tau(x)\int_{x_0}^{x} [z_Z(\xi) + \tau_a(\xi)/\tau(\xi)]\,d\xi \end{aligned} \tag{6.8}$$

where x_0 denotes some distant point on the negative x-axis, $Z_a(x)$ being zero for $x \leq x_0$.

We have to establish now relations between the transfer functions of the anomalous current distribution and the transfer functions of the anomalous surface field. In the case of no inductive coupling with the substratum the anomalous surface field would be simply the field of these sheet currents. Thus, $H_a^+ = 2\pi j_a$ or

$$h_H = q_H \quad \text{and} \quad h_Z = q_Z \; . \tag{6.9}$$

It implies that the substratum is effectively nonconducting down to a depth which is comparable to the half-width of the anomaly.

If this is not so, H_a and Z_a will be attenuated by the inductive couple with the substratum. To account for this effect we superimpose the field of image currents $j_a(x)$ which flow at the level $z = 2h^*$ in the opposite direction. This is equivalent to placing a perfect conductor at the depth h^*. Subtracting in (6.9) the surface field of these image currents gives

$$h_H(x) = q_H(x) - 2h^*/\pi \cdot \int_{-\infty}^{+\infty} \frac{q_H(\xi)\, d\xi}{(2h^*)^2 + (x - \xi)^2} \tag{6.10}$$

according to Biot-Savart's formula in electromagnetic units. A corresponding relation applies to $h_Z(x)$ and the associate transfer functions for the vertical component are found by applying Kertz's operator to the thus obtained functions $h_H(x)$ and $h_Z(x)$. Since the anomalous field which they describe is necessarily of internal origin, we have in virtue of (3.36)

$$z_H = Kh_H \quad \text{and} \quad z_Z = Kh_Z \; . \tag{6.11}$$

We begin the first cycle of the relaxation by ignoring in (6.8) the integrals over z_H and z_Z, i.e., by ignoring the effect of self-inductance upon the anomalous current distribution. This gives

$$q_H(x) = Q \cdot \tau_a(x)/\bar{\tau} \quad \text{and} \quad q_Z(x) = 2\pi i \omega \tau(x) \cdot \int_{x_o}^{x} \tau_a(\xi)/\tau(\xi)\, d\xi \tag{6.12}$$

as first approximation for the component of q_H which is in-phase with $\bar{j}$ and for the component of q_Z which is out-of-phase with regard to $\bar{Z}$. Corresponding "steady-state" approximations for elongated elliptic anomalies can be found in Appendix III. The associated transfer functions z_H and z_Z are derived readily from (6.10) and (6.11).

We return to (6.8) and, after a numerical integration over the thus derived $z_H(x)$ and $z_Z(x)$, obtain the first out-of-phase approximation for q_H and the first in-phase approximation for q_Z, which are inserted again in (6.10, 11). This completes the first cycle of the relaxation.

To begin the second cycle the integrals in (6.8) are evaluated with the first out-of-phase (in-phase) approximation for $z_H(z_Z)$, yielding the second in-phase (out-of-phase) approximation for $q_H(q_Z)$, and so on. The distant anomalous field is preferably simulated by suitable analytic "tails" for which the integrations can be carried out in closed form.

The relaxation will lead to converging approximation, when the effect of self-inductance is small, i.e., when

$$\beta = \omega \bar{\tau} L_a \tag{6.13}$$

(Price, 1949; eq. 107) is small against unity, L_a being the half-width of the anomaly. Convergence is preserved also for $\beta \gg 1$, provided that the inductive coupling with the substratum limits the amplitude of the anomalous surface field. Hence, it is required that $L_a > 4\pi h^*$. Otherwise the approximations tend to diverge and the relaxation must be started differently.

We observe that the "normal" induction parameter from (5.62), $\eta_s = 4\pi\omega\bar{\tau}h^*$, is necessarily large against unity when $\beta > 1$ and $L_a < 4\pi h^*$. This implies that the sheet is nearly impermeable for the incident variation field except for regions of lower than normal total conductivity. We may then ignore the vertical component of the normal variation field $\bar{Z}$ and thereby anomalies of the 2nd kind. A suitable first approximation for those of the 1st kind is obtained by treating low conductivity sections of the sheet as nonconducting holes in an otherwise perfectly conducting sheet (fig. 37).

Appropriate field and current distributions can be found by conformal mapping methods (sec. 6.7). They render $z_H = 0$ above all perfectly conducting parts of the sheet and $q_H = -Q$ in the nonconducting holes. To avoid the edge singularity of z_H (cf. fig. 37) the first cycle of the relaxation is confined to the central parts of the low conductivity sections, where an improved current function q_H is derived with the aid of (6.8). In due course the range of the relaxation is extended over the entire sheet, thereby smoothing out the z_H-singularity of the first approximation.

6.4 Intermediate Anomalies

Let

$$Q^* = 1 - 2Q = \bar{H}^- / \bar{H}^+ \tag{6.14}$$

denote the portion of the tangential normal variations which penetrates through conducting surface layers into the high-resistivity zone of the earth's interior. Any good conductor in this zone is exposed to $Q^*\bar{H}^+$ and $\bar{Z}$ as inducing field. In the case of spherical or cylindrical bodies the pertinent induction parameter is

$$\eta_i = 4\pi\omega\sigma_i R^2 \tag{6.15}$$

with σ_i as conductivity and R as radius. The induction in these bodies is negligible when either Q^* or η_i are small against unity.

It is readily verified from (6.5) that

$$Q^* = (1 + i\eta_s)^{-1}. \tag{6.16}$$

Thus, insulated good conductors of this type do not produce a significant anomaly of the internal part at the earth's surface for any frequency component of the source field unless $\eta_i \gg \eta_s$, i.e., unless

$$\sigma_i R^2 \gg \sigma_s d\,|c|\,; \tag{6.17}$$

$\sigma_s \cdot d$ denotes the total conductivity of the surface layers and $|c|$ the mean depth of the internal eddy currents in the upper mantle. If, for instance, $d = 5$ km and $c = 200$ km, then an insulated conductor of the radius $R = 10$ km should be a hundred times better conducting than the surface layers. In short, only large and very good conductors of this type are detectable by geomagnetic depth sounding.

These considerations do not include yet the additional shielding effect of the surface cover upon the anomalous part of the variations. However, in areas where the normal variation field penetrates through this cover to any extent, the anomalous field will do the same with even less attenuation because of its small spatial wave length.

The anomaly above the embedded cylinder of figure 35 has been derived with the formulas of the 2-dimensional dipole with $R^2Q^*S_c$ as normalized dipole moment (cf. eq. 6.28); S_c denotes the ratio of internal to external parts on the cylinder surface, derived from Kertz's induction curves (1960, fig. 2). The inductive couple with a perfectly conducting mantle at the depth h^* has been taken into account by subtracting the surface field of an image dipole at the depth $2h^*$.

6.5 Deep Anomalies: 1st Interpretation

We assume that the anomaly of the internal part originates from a thin nonuniform layer at a certain level beneath the surface, extending from $z = z_1$ to $z = z_2$ (fig. 36). It is part of a multilayered substratum of known conductivity distribution and separated by insulating matter from the other layers which shall be uniform. This allows us to calculate the downward attenuation of the normal variation field, yielding in

$$\overline{H}(z_1) - \overline{H}(z_2) = 4\pi\overline{j}$$

the normal part of the integrated current per unit width in the nonuniform layer (cf. eq. 5.47, 48).

The superimposed perturbation

$$H_a(z_1) - H_a(z_2) = 4\pi j_a$$

shall be derived with the aid of the relaxation procedure of section 6.3 for a given conductivity distribution, representing the underlying layers by a perfect conductor at the level $(z_2 + h^*)$. The thus obtained anomalous field diffuses upward through the overlying layers with amplitude reduction and phase rotation. We express its x-dependence as spectrum of sinusoidal waves with

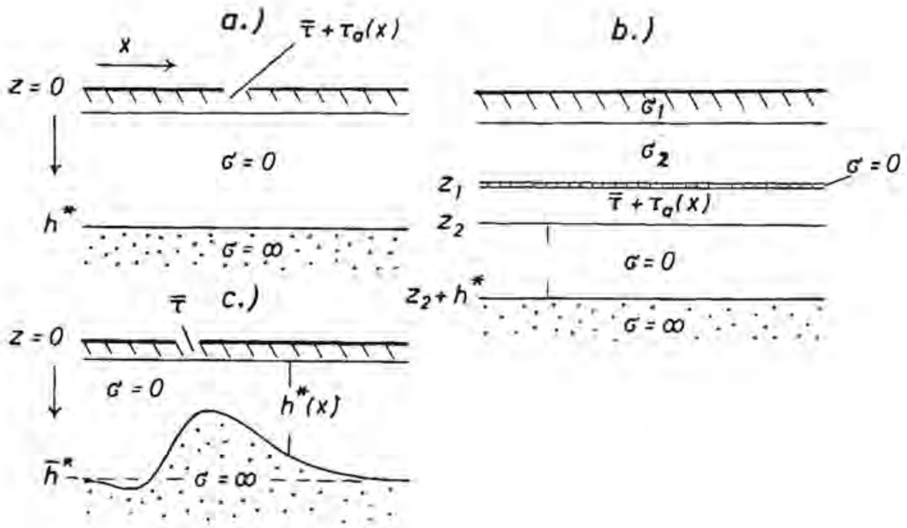

Fig. 36. Schematic conductivity models, illustrating (a) surface anomalies, (b) deep anomalies of the 1st kind, (c) deep anomalies of the 2nd kind.

$\exp(ik_a x)$ as wave number. The diffusion of one particular wave component is controlled by the propagation constant

$$(k_a^2 + 4\pi i \omega \sigma)^{-1/2}$$

with $G_a(z)$ as characteristic vertical function as introduced in (5.34). Since the anomalous field is of internal origin, $G_a(+0) = -1$. Starting with this value we can derive $G_a(z)$ for all interfaces between the surface and $z = z_1$, using the recurrence formula (5.44). This allows us at the same time to derive the anomalous surface field for $z = 0$ according to (5.47) and (5.48), where it can be compared with an observed anomaly.

6.6 Deep Anomalies: 2nd Interpretation

The mean stratified conductivity distribution within the range of an observed anomaly is represented by a perfect substitute conductor at the level $z = \overline{h}^*$ (sec. 5.6). It is derived from the normal ratio of vertical to horizontal variations in that region or from the "normal" surface impedance of the incident field. We recall that $\overline{h}^*$ is not the same for all frequencies and that it is greater for slow than for fast variations, reflecting the increasing depth of penetration of the normal variation field.

Lateral nonuniformities in the deep conductivity distribution cause a variable depth of penetration from place to place for a given frequency. The arising perturbation of the induced variation field is considered here to result from an undulatory depth

$$h^*(x) = \overline{h}^* + h_a(x) \tag{6.18}$$

of the perfect substitute conductor (fig. 36). The boundary condition requires that the transient magnetic vector above this conductor is tangential to its surface, hence

$$dh^*/dx = (\overline{Z} + Z_a)/(\overline{H} + H_a) . \tag{6.19}$$

The undulations $h_a(x)$ can be found by constructing the internal field-line pattern beneath an observed anomaly. Each field line which does not intersect the earth's surface $z = 0$ is one possible interface between nonconducting and perfectly conducting matter, since it satisfies the boundary condition (6.19). From the family of field lines we choose that which merges at a distance from the anomaly into a preconceived normal level $\overline{h}^*$.

The required downward extension of the variation field will be carried out separately for its normal and anomalous parts. We observe that the normal horizontal component $\overline{H}$ may be attenuated while passing through a thin sheet of conducting surface layers, and we shall use again the notation $\overline{H}^- = Q^* \cdot \overline{H}$ from equation 6.14 ($\overline{H} = \overline{H}^+$) to designate the normal variation field beneath these layers. For $h^* > z > 0$ we may regard $\overline{H}^-$ as uniform, since the downward decrease of its "external" part is compensated by a concurrent increase of its "internal" part.

The normal vertical component $\overline{Z}$ passes without change through the surface layers and decreases steadily on the way down, so that $\overline{Z} = 0$ for $z = \overline{h}^*$. We shall use here the approximation from (5.54), stating that

$$\overline{Z}(x,\ z) \approx (\overline{h}^* - z) \cdot \partial\overline{H}/\partial x \ ;$$

the horizontal gradient of $\overline{H}$ will be ignored otherwise.

The downward continuation of the anomalous part is a straightforward matter when it is of truly internal origin. We can develop, for instance, the field at the level $z = 0$ into a series of spatial harmonics and obtain for any interior point (cf. eq. 3.34).

$$\left.\begin{aligned} H_a &= \sum_n c_n \\ Z_a &= \sum_n -ic_n \end{aligned}\right\} \exp[\ nk_a(ix + z)] \tag{6.20}$$

when we disregard any attenuation by conducting surface layers. This is permissible when their shielding effect upon $\overline{H}$ is small.

The slope of the field line $z(x) = h^*(x)$, passing through the point $(x,\ z)$ follows then from (6.19) as

$$dh^*/dx = \frac{Z_a(x,\ h^*) - h_a(x) \cdot \partial\overline{H}/\partial x}{H_a(x,\ h^*) + Q^*\overline{H}} \ . \tag{6.19a}$$

The entire field lines are put together by numerical or by graphical methods, starting with $h^*(x) = \bar{h}^*$ at some distance from the anomaly. Obviously, this procedure is meaningful only when the time functions in (6.19a) are roughly of the same phase. The argument of Q^*, given by $\tan^{-1}(-\eta_s)$, is small against unity when the shielding effect is small as required. Hence, this kind of interpretation pertains to those components of H_a and Z_a which are in-phase with $\bar{H}$.

Consider, for instance, the sinusoidal induction anomaly

$$H_a(x, 0) = c \cdot \sin(k_a x)\bar{H}$$

$$Z_a(x, 0) = -c \cdot \cos(k_a x)\bar{H} \quad \text{with} \quad \partial\bar{H}/\partial x \approx 0.$$

The resulting differential equation for field lines

$$dz/dx = \frac{-c\cos(k_a x) \cdot \exp(k_a z)}{Q^* + c\sin(k_a x) \cdot \exp(k_a z)}$$

can be solved analytically by making the substitution $v = \exp(-k_a z)$, yielding

$$z(x) = z(0) - \frac{c}{Q^* k_a} \sin(k_a x) \cdot \exp(k_a z) \tag{6.21}$$

as "field-line equation." The corresponding equation for the orthogonal potential lines is readily found to be

$$x(z) = x(-\infty) + \frac{c}{Q^* k_a} \cos(k_a x) \cdot \exp(k_a z)\,.$$

Each field line oscillates non-symmetrically around $z(0)$. These oscillations are nearly sinusoidal when $k_a z \ll 1$, degenerating into deformed square waves for $k_a z > 1$. By equating $z(x)$ with $h^*(x)$ (6.21) becomes a non-algebraic expression for the undulating surface of a perfect substitute conductor beneath the sinusoidal anomaly. It is presumed of course that $z(x)$ is positive for all values of x.

Equation 6.21 can be useful to obtain a first interpretation of empirical induction anomalies which are considered to be of deep origin. The Rio Grande anomaly of bays, for example, could be approximated for 1 cph by

$$Z_a(x, 0) = -0.125 \cdot \bar{H} \cdot \cos(k_a x)$$

with $2\pi/k_a = 800$ km as spatial wave length and $x = 0$ at Lordsburg (fig. 10). We ignore the shielding effect of the surface cover and set $Q^* = 1$. Inserting $h^*(0) = 138$ km we obtain from (6.21) $h^* = 102$ km as highest elevation of the perfectly conducting interface under the Rio Grande ($x = 200$ km) and $h^* = 260$ km as its deepest depression under the Texas Foreland ($x = 600$ km). This agrees well with the finally adopted interface, based on a downward extension of the actually observed anomaly (fig. 48).

6.7 Conformal Mapping Methods

We assume again that a 2-dimensional interface separates an upper nonconducting from a lower perfectly conducting half-space, being exposed to a time-varying source field incident from above. The field distribution above the interface can be found by conformal mapping, a method first proposed by Cox (personal communication) for the interpretation of induction anomalies.

Let U(x, y) be a magnetic scalar potential, given in the upper half-plane of rectangular (x, y) coordinates, y up. (The letter z is reserved in this section for the complex variable x + iy.) The potential function shall be harmonic, $\nabla^2 U = 0$, and $\partial U/\partial y = 0$ for $y = 0$. Hence, the magnetic field vector $\mathbf{F} = -\,\mathrm{grad}\, U$ is tangential to the x-axis and it shall represent the normal variation field $\overline{\mathbf{F}}$ in a nonconducting region above a perfectly conducting substratum with plane boundary.

Consider an analytic function

$$w(z) = u(x,\ y) + i \cdot v(x,\ y)$$

with the derivative $u_x + i \cdot v_x \neq 0$ ($u_x = \partial u/\partial x$, $v_x = \partial v/\partial x$) which maps the point P(x, y) of the z-plane into the image point P*(u, v) of the w-plane. The mapped potential function U*(u, v) remains harmonic and preserves in particular the property that its derivative perpendicular to the mapped x-axis vanishes. By choosing an analytic function that transforms the x-axis into the postulated interface of nonconducting and perfectly conducting matter the boundary condition on that interface is satisfied and U*(u, v) becomes the potential function of the anomalous plus normal variation field above the interface.

The field vector $\mathbf{F}^* = -\,\mathrm{grad}\, U^*$ at the image point P* is stretched by the factor $1/r$ relative to $\mathbf{F}$ at P and rotated counterclockwise by the angle ϕ, where

$$r^2 = u_x^2 + u_y^2, \quad \cos\phi = u_x/r, \quad \sin\phi = u_y/r\ .$$

Thus,

$$F^* = F/r \quad \text{and} \quad I^* = I + \phi$$

where I and I* denote the upward inclination angle of the field vectors against the positive x-axis, respectively u-axis. After equating $\mathbf{F}$ with $\overline{\mathbf{F}}$ and $\mathbf{F}^*$ with the vectorial sum $(\overline{\mathbf{F}} + \mathbf{F}_a)$ we obtain for the transfer functions between $\mathbf{F}_a$ and $\overline{\mathbf{F}}$ (cf. eq. 6.1)

$$\begin{aligned} h_H &= z_Z = (\cos\phi)/r - 1 \\ h_Z &= -\,z_H = (\sin\phi)/r \end{aligned} \tag{6.22}$$

We discuss now a number of mapping functions which are of particular interest in this context. Suppose a highly conductive surface sheet, containing a nonconducting strip of the width 2L, is underlain at the depth h^* by a perfect plane conductor (fig. 37). This strip could represent, for instance, an elongated island in a large ocean which is impermeable for the incident variation field for the frequencies considered here ($\eta_s \gg 1$).

The appropriate mapping function

$$w(z) = h^*/\pi \cdot [z + \ell n(\frac{z+a}{z-a}) + i\pi]$$

$$L = h^*/\pi \cdot [\sqrt{a^2 + 2a} + \ell n(a + 1 + \sqrt{a^2 + 2a})] \tag{6.23}$$

transforms the x-axis between - a and + a into the surface of the underlying conductor, while the sections $|x| > a$ become inner and outer surfaces of the sheet. The positive y-axis transforms into the v-axis with a slight expansion in its lower part. The mapping of a rectangular grid from the z-plane into the w-plane is shown in figure 37 for $L = 0.97 \cdot h^*$ or $a = 1$.

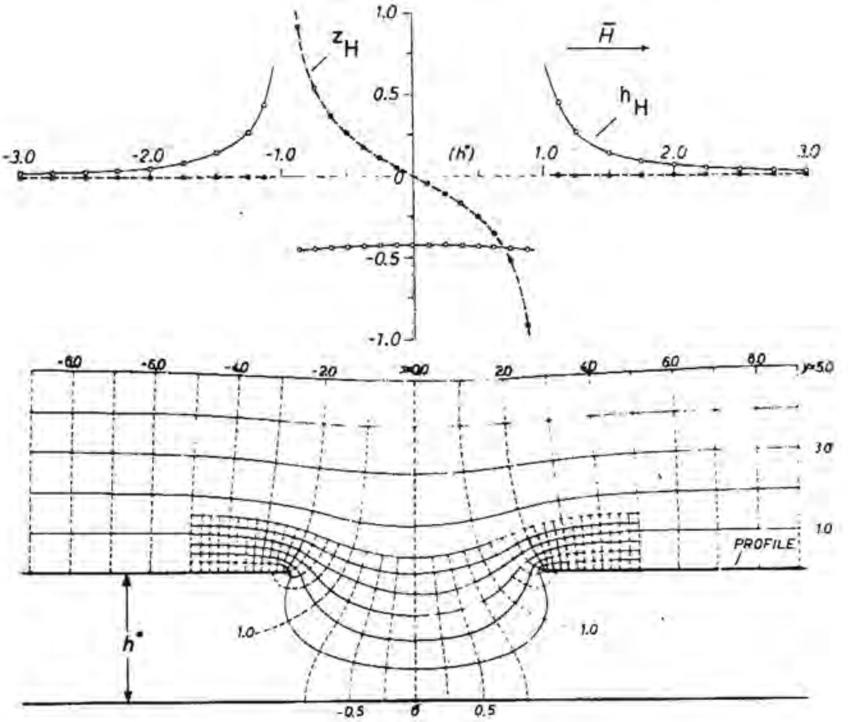

Fig. 37. Transfer functions for the anomalous (in-phase) part of transient variations above a perfectly conducting sheet with a nonconducting gap, underlain by a plane conductor of infinite conductivity. The lower graph shows the deformation of a rectangular grid, representing the distorted field distribution of an otherwise uniform horizontal field $\tilde{H}$ near the gap. Lines y = const. are field lines and those of x = const. are potential lines of the distorted field.

Evaluating (6.22) with (6.23) yields for $y = 0$, i.e., for the surface of perfectly conducting matter

$$h_H = 2a/(x^2 - a^2 - 2a) \quad \text{and} \quad z_H = 0 .$$

Thus, $Z_a = 0$ as required and H_a disappears as $1/x^2$ on the outer surface of the sheet. On the inner surface h_H approaches -1 with increasing distance from the hole when $x \to a$, yielding $\overline{H} + H_a = 0$ as required below the perfect conductor.

The concentration of induced sheet currents at the edges of the sheet $(x^2 = a^2 + 2a)$ is evident from $h_H = \infty$ and the appearance of anomalous currents in the substratum below the hole from $h_H = -2/(2 + a)$ for $x = 0$. The depression of H in the center of the hole ("island effect" upon the horizontal component) for $u = 0$ and $v = h$ is found to be

$$h_H = -2a/(a^2 + 2a + y_c^2)$$

where y_c is the solution of the nonalgebraic expression

$$\pi = y_c + 2 \cdot \tan^{-1}(y_c/a)$$

($y_c = 1.31$ for $a = 1$). Profiles of z_H and h_H show as a predominant feature the sharp edge singularity of z_H.

If the width of the nonconducting strip becomes large in comparison to the depth of the substratum ($L \gg h^*$), the mapping function (6.23) reduces to

$$w(z) = h^*/\pi \cdot [z + 1 + \ell n\, z] \qquad (6.24)$$

when the right-hand edge is moved to infinity. This transformation has been used by Cox (1960) to describe the anomalous behavior of magnetic variations near coastlines. Ashour (1965) solved the corresponding problem for a hemispherical oceanic shell, even though the coupling with conducting matter in the mantle is not included in his rigorous solution.

The negative y-axis transforms now into the inner and outer surface of the sheet, while the positive x-axis becomes the surface of the underlying perfect conductor. The edge of the sheet is the image of P(- 1, 0). Along the mapped x-axis we obtain here

$$h_H = -1/(1 + x) \quad \text{and} \quad z_H = 0 .$$

The concentration of sheet currents near the edge can be approximated by

$$4\pi j/\overline{H} = (1 + x_-)^{-1} - (1 + x_+)^{-1} \approx \sqrt{2h^*/(\pi s)} \; ; \qquad (6.25)$$

x_+ and x_- denote points on the x-axis which map into image points on the outer and inner side of the sheet, having the same distance s from the edge. The approximation holds for $s \ll h^*/\pi$.

The resulting anomaly on the nonconducting side of the edge is characterized by a smooth negative anomaly in H and a sharply peaked positive anomaly in Z (fig. 38). Near the edge h_H approaches - 1/3 while z_H becomes infinite. The horizontal scale for the anomalous variation field is given by the depth to the underlying perfect conductor.

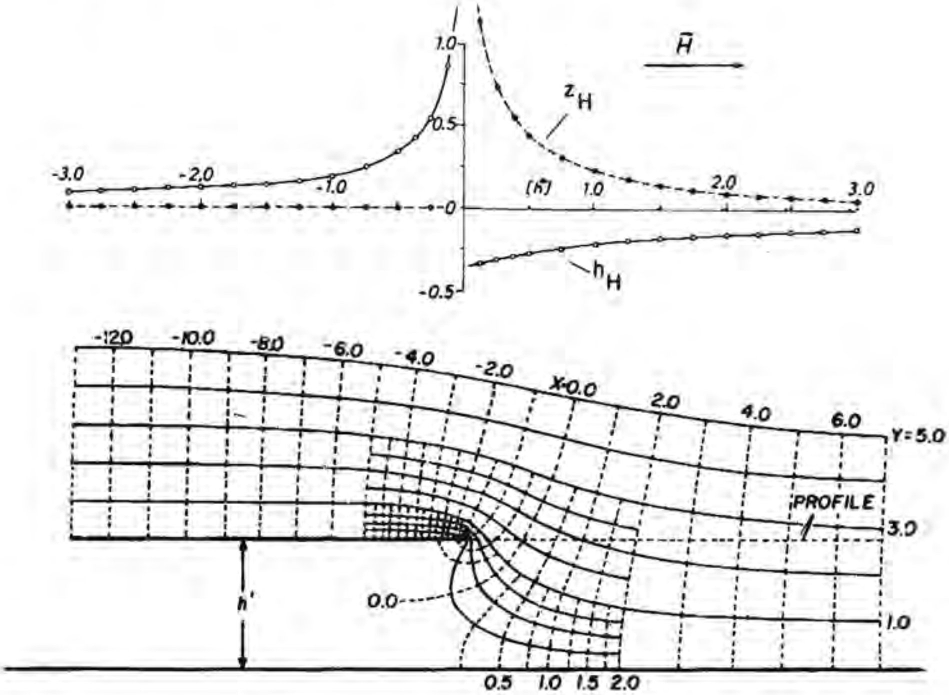

Fig. 38. Transfer functions for the anomalous (in-phase) part of transient variations above the edge of a semi-infinite perfectly conducting sheet, underlain by a plane conductor of infinite conductivity. Cox's model for the coastal anomaly of fast variations near large and deep oceans (cf. legend of fig. 37).

We consider now two mapping functions relevant to induction anomalies of deep origin. Figure 39 shows a perfectly conducting substratum with a step in its surface. The pertinent analytic function is

$$w(z) = s/\pi \cdot (\sqrt{z^2 - 1} + \cosh^{-1} z) . \qquad (6.26)$$

It transforms the x-axis from - ∞ to - 1 into the upper and from + 1 to + ∞ into the lower horizontal interface, while the piece between - 1 and + 1 becomes the vertical wall of the height s.

The anomalous field above the step is quite similar to that above the semi-infinite sheet (fig. 39). In particular the z_H-profiles are almost indistinguishable, while a slight difference in the h_H-profiles can be noticed. The induction anomaly is smoothed out rapidly with height as seen from the profile in the level $v = 2s$. The z_H-maximum is displaced thereby slightly to the right, reflecting the shift of maximal inclination of the field lines above the step. The varying density of potential lines $x = \text{const.}$ along the interface shows the concentration of induction currents near the upper corner and their dilution at the bottom of the step.

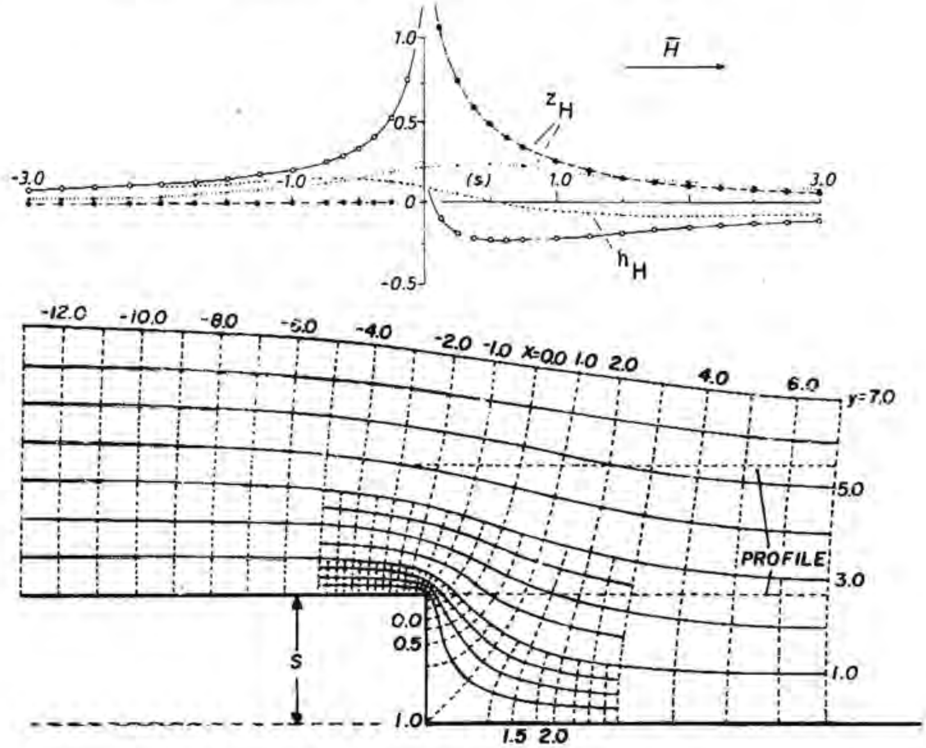

Fig. 39. Transfer functions for the anomalous (in-phase) part of transient variations above a step in the otherwise plane surface of a perfect conductor, shown for two different levels above the step. Basic model for the interpretation of the Rio Grande anomaly (cf. legend of fig. 37).

Consider in conclusion the transformation by

$$w(z) = R/2 \cdot (z + \sqrt{z^2 - 4}) . \tag{6.27}$$

The x-axis maps here for $|x| \geq 2R$ into the u-axis and for $|x| < 2R$ into a semicircle of the radius R around P(0, 0). The distorted field above this semicircular elevation is that of a 2-dimensional dipole, superimposed upon a uniform horizontal field, when the field distribution in the z-plane is uniform and horizontal. Thus,

$$\begin{aligned} h_H(u,v) &= (R/r)^2 \cos 2\theta \\ z_H(u,v) &= (R/r)^2 \sin 2\theta \end{aligned} \tag{6.28}$$

with $\cos\theta = u/r$ and $r^2 = u^2 + v^2$.

The anomalous field of model "b" in figure 35 has been derived from these formulae. Similar profiles above elevations of semielliptic and triangular cross section can be found in Rikitake and Witham's article (1964, pp. 40, 41).

7. INTERPRETATION OF THE ANOMALIES

7.1 Primary Source Field and Mean Conductivity Distribution

There are two ionospheric current systems that we have to consider as sources for the large-scale induction process, the Sq-system of the slow diurnal variations and the D-system of fast storm-time variations (cf. chaps. 7 and 9 of Geomagnetism). Bay-type disturbances represent "polar elementary storms" (Fukushima, 1953) of short duration. Their overhead currents form a strongly concentrated auroral "jet" with widespread return currents in mid-latitudes (Silsbee and Vestine, 1942).

Sq-variations occur at a site according to local time and their field may be visualized as a progressive wave that follows the sun around the earth. Hence, latitude and longitude dependence of the mth time harmonic can be expressed by a series of spherical surface harmonics of the rank m and of the degree $n = m, m+1 \ldots$ (eq. 5.8). During the equinoxes, when the Sq-vortices in the northern and southern hemispheres are of equal strength, the vertical Sq-component $H_r \sim P_n^m$ is antisymmetric to the equator. The series contains then only the terms $P_{m+1}^m\ P_{m+3}^m \ldots$ and for a first approximation we may drop all terms except the first one.

Bays, on the other hand, occur more or less simultaneously over great distances and their source field may be regarded as a spectrum of standing waves. These waves are polarized predominantly in a north-south direction, since mid-latitude bays show a remarkable uniformity on east-west profiles (fig. 7) in contrast to a distinct reduction of the H-amplitude toward south (fig. 27). This reduction amounts to roughly 4% per hundred kilometers between 40 and 30 degrees latitude, yielding

$$k = (\partial H/\partial x)/H = 0.0004\ [\mathrm{km}]^{-1} \qquad (7.1)$$

as effective wave number of the bay field in the southwestern United States. It may be added that the auroral jet produces substantial external Z-amplitudes in mid-latitudes (Fleischer, 1954, fig. 8), which are nearly compensated by the opposing Z-field of internal eddy currents. Their mean depth h^* could hardly exceed therefore 250 km which would give a Z/H amplitude ratio of $kh^* = 0.1$ (eq. 5.54) under normal conditions.

The interpretation of the various anomalies from chapter 4 requires certain assumptions concerning the prevailing mean conductivity as function of depth. We are faced here with the superficial contrast of continents and oceans which we shall treat separately by using

$$\tau_{\phi} = 16 \cdot 10^{-6} \text{ emu} \cdot \text{cm} \tag{7.2a}$$

as mean total conductivity of the surface cover at sea and

$$\tau_{L} = 0.4 \cdot 10^{-6} \text{ emu} \cdot \text{cm} \tag{7.2b}$$

on land. These values correspond to 4000 m and 100 m of seawater, respectively. The land value is also equivalent to 4000 m of rock formations with a resistivity of 10 $\Omega \cdot$ m, which seems to be a reasonable continental average.

Deep conductivities in the upper mantle are represented by a perfect substitute conductor at the frequency-dependent depth h^* as introduced in section 5.5, 6. The evaluation of the coastal anomaly led to estimates for h^* in California as listed in table 2 for various frequencies. They are compared with corresponding values obtained from Lahiri and Price's model "d" and other distributions in table 3.

7.2 Coastal Anomaly in California

This anomaly has been studied in great detail on land, but its continuation toward the open ocean remained largely unknown. The illustrations in figures 40 to 45 summarize the results of the interpretation attempted here for frequencies between 0.5 and 4.0 cph. The empirical z_P and h_P-profiles have been obtained by projecting the transfer values between anomalous and normal parts (tabs. 6-10) upon the direction of the various profiles perpendicular to the coast (eq. 3.26). Hence, z_P represents the complex ratio $Z_a/\overline{B}$ where $\overline{B}$ refers to the normal part of the horizontal disturbance vector which is perpendicular to the coast. The presence of a minute normal part in Z has been ignored throughout the data reduction (cf. sec. 3.11).

Details about the model calculations which led to the computed curves will be discussed separately in section 7.3. It may suffice to state that the models are 2-dimensional and that they consist of a thin surface cover of variable total conductivity above nonconducting matter and a perfectly conducting substratum at the depth h^*. The total conductivity merges into τ_{ϕ} at sea and into τ_L on land (eq. 7.2). Near the coast τ is chosen according to the change in water depth and two inland anomalies have been added to account for the effect of the San Joaquin valley and of the Sierra Nevada on the distribution of superficial eddy currents.

We infer from the extreme edge model in figure 38 that the slope of the z_P-profiles from the coastal peak toward inland is determined by the depth to the underlying perfect conductor. Hence, h^* as the only free parameter of the models is also a very critical one which can be adjusted by trial and error to yield the best possible fit between the observed and the computed z_P-profiles. This has been done, and the resulting h^*-values are listed in table 2 together with the corresponding Q-ratios of equation 6.5 in reference to the relative strength of superficial eddy currents on land and at sea.

As one might have expected from the increasing depth of penetration of the incident variation field, h* increases from 80 km at 4 cph to 200 km at 0.5 cph. This corresponds to the observation that fast Z-variations disappear within a shorter distance from the coast than slow Z-variations (fig. 24). We infer from the Q-ratios that superficial eddy currents are insignificant on land for the frequencies considered here but of considerable strength at sea, so that the bay field hardly penetrates into the deeper earth's interior beneath the ocean.

Let us examine the three northern profiles Farallon Islands-Fallon, Monterey-Bridgeport, Cambria-Bishop (figs. 40-42) in detail. The theoretical in-phase anomalies in Z are bell-shaped and centered on the continental

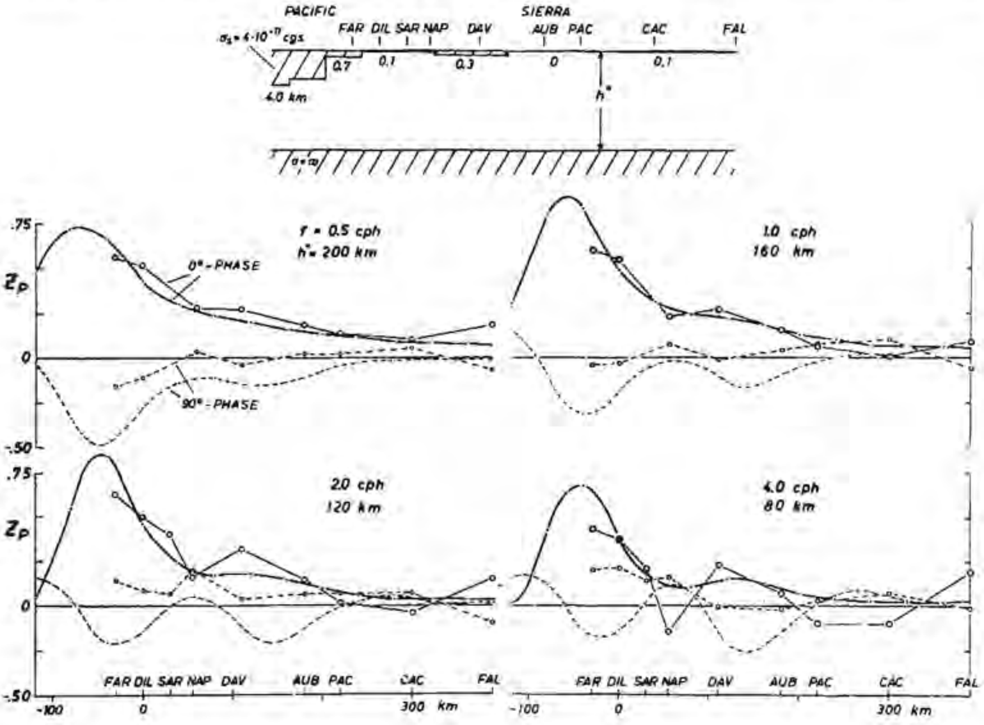

Fig. 40. Profile Farallon Islands-Fallon, Nevada: Interpretation of the coastal anomaly of bays and fast variations as edge effect of oceanic induction currents above a perfectly conducting substratum at the frequency-dependent depth h.* Upper diagram shows the 2-dimensional conductivity model in which the total conductivity of the nonuniform top layer is indicated by the thickness of an equivalent layer of seawater. Lower diagrams: Comparison of computed (dots, connected by curves) and empirical (circles, connected by straight lines) transfer values z_p. Solid curves and lines: in-phase components of z_p; dashed curves and lines: negative out-of-phase components of z_p. Notice the unexplained anomalous behavior of fast Z-variations between Napa and Davis and east of the Sierra Nevada (CAC, FAL), indicating a locally disturbed deep conductivity structure.

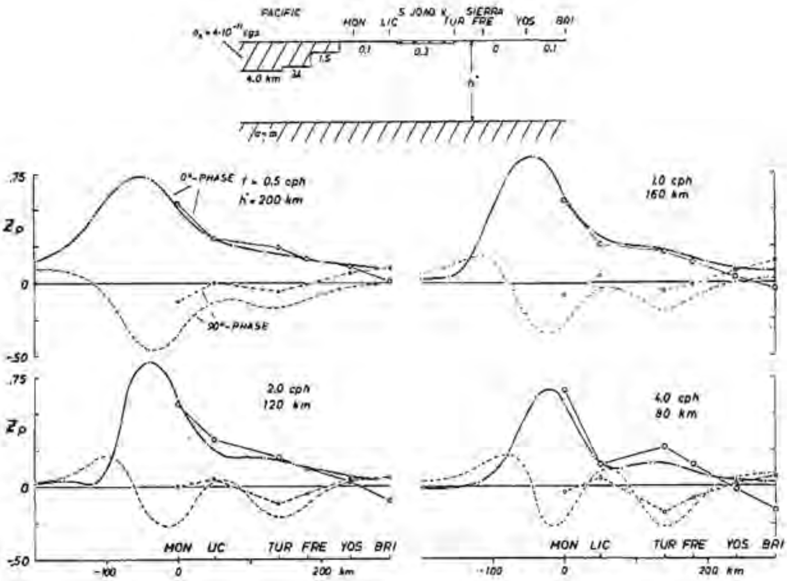

Fig. 41. Profile Monterey-Bridgeport: interpretation of the coastal anomaly between 0.5 and 4 cph as edge effect of oceanic induction currents (cf. legend of fig. 40). Comparison of computed and empirical z_p-profiles, representing the anomalous behavior of Z-variations. Negative in-phase z_p-values at Bridgeport for 2 and 4 cph remain unexplained and suggest uplift of high internal conductivities east of the Sierra Nevada.

slope. They reflect the expected offshore concentration of oceanic induction currents parallel to the coast line. We observe a slight dissymetry at high frequencies because the anomalous Z-amplitude is dampened out more rapidly above the ocean than above land (cf. extreme edge model of fig. 38). The effect of high conductivities in the San Joaquin valley is hardly noticeable at 0.5 and 1.0 cph but stands out clearly at 2 and 4 cph, reflecting the increased contribution of superficial eddy currents to the internal part.

The theoretical behavior of the out-of-phase Z-component is more complicated. For 0.5 cph the out-of-phase z_p-curves are similar to the corresponding in-phase curves but with visible humps near the edges of the San Joaquin valley. With increasing frequency the out-of-phase profiles convert into two sinusoidal undulations, indicating two anomalous "line currents," one in the ocean just offshore and the second on land in the San Joaquin valley.

The close agreement we find between the empirical and the computed curves suggests that these simple models can account indeed for the main features of the observed coastal anomaly of Z-variations (0.5 - 4.0 cph). There are some minor discrepancies. The empirical out-of-phase profiles, for instance, seem to be displaced by a constant amount from the calculated curves as is clearly seen at 0.5 and 1.0 cph. We encounter here a basic deficiency of the models. By replacing finite mantle conductivities by a perfect conductor at a certain depth we overestimate the phase of the eddy currents in the ocean, which leads to a corresponding overestimate of the phase for anomalous Z-variations near the coast. Other disagreements will be discussed in section 7.4.

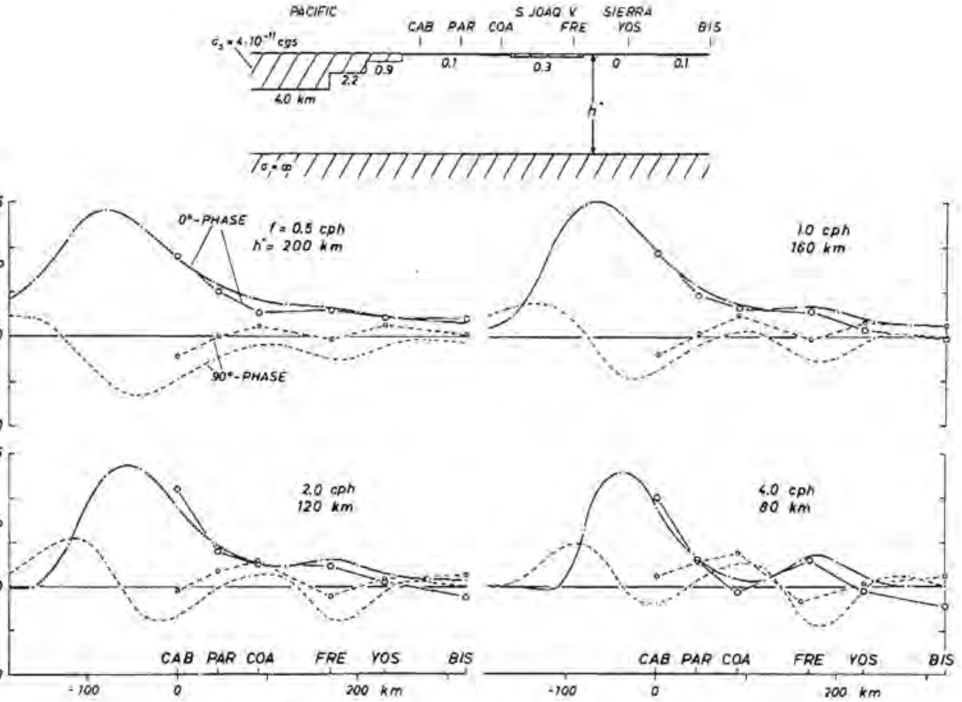

Fig. 42. Profile Cambria-Bishop: interpretation of the coastal anomaly between 0.5 and 4 cph as edge effect of oceanic induction currents (cf. legend of fig. 40). Comparison of computed and empirical z_p-profiles, representing the anomalous part in Z. Again negative z_p-values east of the Sierra Nevada at Bridgeport due to reversal of Z-amplitude (cf. station BRI in fig. 41.

The theoretical curves in figures 43 and 44 predict strongly enhanced horizontal variations above the ocean which drop off sharply toward the shore, reflecting again the pinching of oceanic eddy current parallel to the coast. On the continental side we expect a smooth increase of the horizontal amplitude from a depression near the coast which is in good agreement with the observed anomalous behavior in H and D.

Model calculations for the southern profile San Clemente Island-Yuma are complicated by the presence of a broad continental shelf (fig. 45). They predict accordingly two edge anomalies of Z-variations, one at the continental slope and the other at the actual coastline. The first-mentioned anomaly is predominant at 0.5 cph and flattens out toward 4.0 cph, while the opposite applies to the second one.

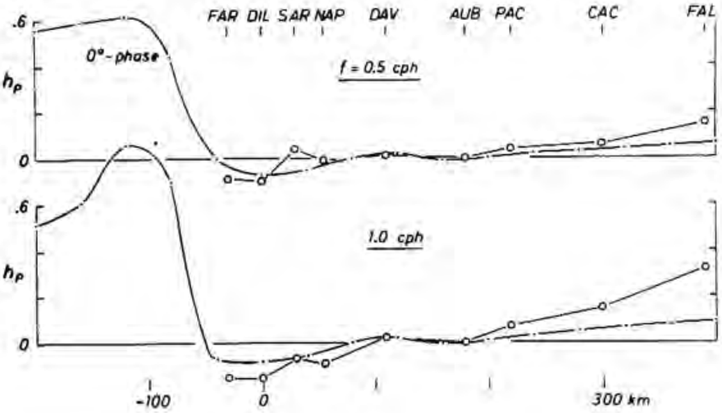

Fig. 43. Coastal anomaly of horizontal variations in California, profile Farallon Islands-Fallon, Nevada. Curves represent computed h_P-profiles for the conductivity model of fig. 40, open circles, connected by straight lines, represent empirical in-phase h_P-values; h_P is zero by definition at the reference station AUB.

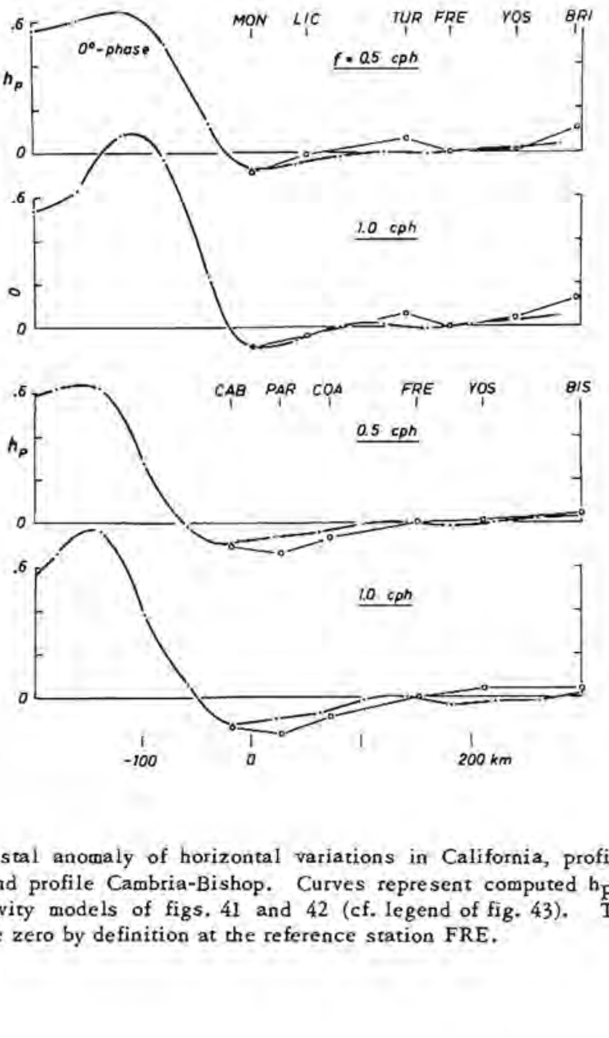

Fig. 44. Coastal anomaly of horizontal variations in California, profile Monterey-Bridgeport and profile Cambria-Bishop. Curves represent computed h_p-profiles for the conductivity models of figs. 41 and 42 (cf. legend of fig. 43). The empirical h_p-values are zero by definition at the reference station FRE.

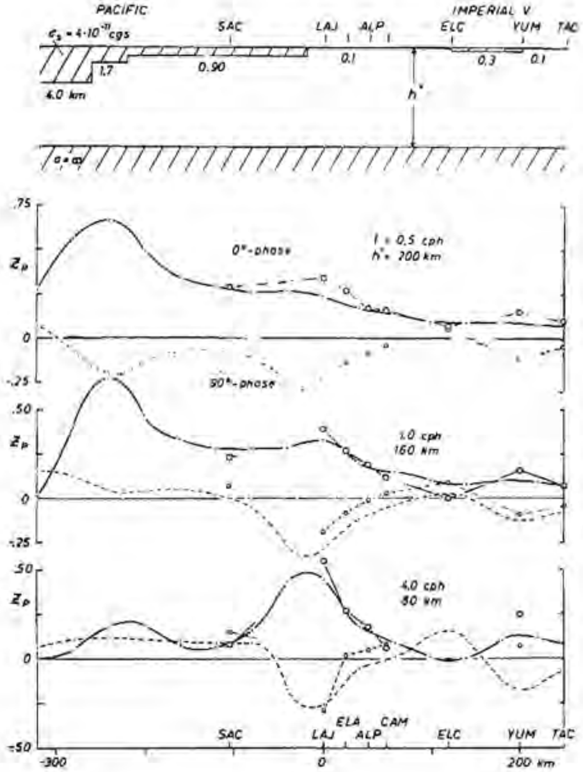

Fig. 45. Coastal anomaly of bays and fast variations in southern California, Profile San Clemente Island-Tacna, Arizona. Comparison of computed and observed zp-profiles (cf. legend of fig. 40. The model calculations predict two edge effects of oceanic induction currents, one at the continental slope and the other one at the coast. The special island effect of San Clemente is not included in the model calculations.

The fit between observed and computed zp-profiles is here in general less satisfactory than on the three northern profiles. The observed in-phase Z-variations at La Jolla exceed the theoretical values and they drop off more sharply inland than expected. On the other hand, the model calculations predict correctly the out-of-phase Z-component (except for a minor and constant displacement) and they give Z-variations of the right amplitude and phase for San Clemente Island.

In summary, the coastal anomaly of bays and similar fast variations can be explained reasonably well by the superficial conductivity contrast of seawater and rock formations above a plane deep conductivity distribution. Could the anomaly be explained in some other way, say, by an unequal distribution of mantle conductivity? This is indeed possible.

Suppose a sharp increase in mantle conductivity occurs just under the continental slope, which brings deep induction currents of bay-type disturbances close to the surface beneath the sea floor, at the same time dampening the induction in the seawater itself. In the simplified models considered here we would postulate a stepwise uplift of a perfect conductor as shown in figure 39. Notice that this step would have to be under the actual coastline in southern California rather than under the continental slope as offshore central California.

In order to explain the large anomalous Z-amplitude at the coast the height of the step has to be several times the depth of the perfect conductor beneath the ocean. Considering for instance the frequency 1 cph, it would be required that the conductor rise from 160 km under the continent to 60 km or less under the ocean. The coastal anomaly would become in this way an "edge effect" of mantle induction currents, since the induction in the ocean itself would be suppressed by the underlying good conductor at shallow depth.

Finally, the coastal anomaly could be interpreted as a combination of both effects, i.e., partly as "edge effect" of oceanic and partly as "edge effect" of mantle induction currents. This interpretation is favored presently by Cox and Filloux (Filloux, 1967) who observed concurrently with the magnetic program the transient electric field fluctuations on the ocean floor offshore from Cambria, i.e., more or less in the continuation of the profile Cambria-Bishop. They compared the electric component parallel to the general trend of the coast with the horizontal magnetic component perpendicular to the coast at CAB and obtained 110 km seaward from the continental slope an amplitude ratio of 0.08 mV/km/gamma for 1 cph (Filloux and Cox, 1966, tab. 2). This is slightly less than expected for the oceanic "edge-effect" model shown in figure 42, which predicts for this location an amplitude ratio of 0.105 mV/km/gamma. Furthermore, observations further away from the continent revealed that the attenuation of the electric fluctuations toward the open ocean is greater than expected from the simple "edge-effect" model of figure 42.

Filloux (1967) recorded also the transient magnetic fluctuations with a submerged D-variometer on the sea floor, 600 km offshore from Cambria. A comparison with simultaneous records on land revealed a distinct reduction of the D-amplitude of bays at the sea floor which demonstrated clearly the presence of induced eddy currents in the ocean. The amplitude ratio D (sea floor) to D (Cambria) is about 0.25 for 1 cph while the pure oceanic "edge-effect" model of figure 42 would yield an amplitude ratio of 0.22. The attenuation of diurnal D-variations at the sea floor was found to be surprisingly small (Larsen and Cox, 1966).

We may state in conclusion that bay-type disturbances induce indeed substantial eddy currents in the Pacific Ocean offshore the California coast, even though they seem to be a bit weaker and more strongly pinched together near the coast than expected. The observed anomaly remains nevertheless in the first place an "edge effect" of oceanic induction currents while the hypothetical rise of high mantle conductivities at the continental margin would produce only a second order anomaly on land.

7.3 Method of Calculations

The theoretical curves in figures 40 to 45 have been derived with the aid of the relaxation procedure of section 6.3 as follows: Let a conductive surface sheet occupy the horizontal (x, y) plane of Cartesian coordinates, z down. The y-axis separates a semi-infinite ocean ($x < 0$) from a semi-infinite continent ($x > 0$) above a perfect plane conductor at the depth $z = h^*$. The total conductivity τ of the sheet is only a function of x, assuming that such anomalies as the San Joaquin valley are elongated anomalous zones parallel to y (fig. 46). The conductivity profiles at the top of each illustration are vertical cross sections through these 2-dimensional models.

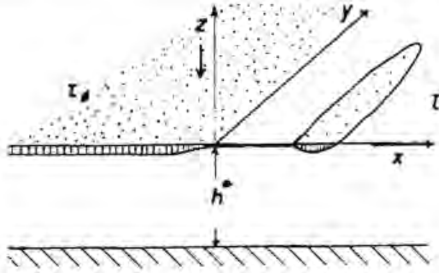

Fig. 46.

Let the oceanic value τ_ϕ from equation 7.2a be the normal part of τ which implies that the corresponding continental value τ_L from equation 7.2b is the sum of a normal plus anomalous part $\tau_a(x)$. Hence,

$$\tau_a(x_L) = \tau_L - \tau_\phi \qquad (7.3)$$

where x_L denotes some distant point on the land side. The normally induced sheet-current density on the oceanic side $\bar{j} = j_\phi$ has to merge smoothly into the normal sheet-current density j_L on land, by means of the superimposed anomalous part $j_a(x)$. Hence, $j_a(x_L) = j_L - j_\phi$ or with the notations of (6.5) and (6.6)

$$q_H(x_L) = 2\pi(j_L - j_\phi)/\overline{H} = Q_L - Q_\phi \, , \qquad (7.4)$$

the Q-ratios referring here to the y-component of the sheet currents. Substituting (7.4) into (6.8) yields for anomalous variations of the 1st kind the important relation ($Q = Q_\phi$, $\bar{\tau} = \tau_\phi$)

$$2\pi i\omega \int_{x_0}^{x_L} z_H(x)\,dx = Q_L/\tau_L - Q_\phi/\tau_\phi \qquad (7.5)$$

where x_0 denotes some distant point on the oceanic side. It is presumed of course that $z_H(x)$ has no singularities between x_0 and $+x_L$, i.e., that $\tau_a(x)$ is a continuous function of x.

We replace Q_ϕ and Q_L by their source-field free approximations from (6.5) and obtain

$$\int_{x_0}^{x_L} z_H(x)\,dx = h^*/(1 + i\eta_L) - h^*/(1 + i\eta_\phi) \, . \qquad (7.6)$$

This expresses the edge anomaly of the vertical variation field when integrated across the interface of two semi-infinite sheets of different conductivity in terms of the sheet-substratum induction parameter

$$\eta_L = 4\pi\omega\tau_L h^* \qquad \eta_\phi = 4\pi\omega\tau_\phi h^*$$

on either side. Weidelt (1966, p. 58) derived a corresponding relation in a quite different manner.

The edge anomaly naturally has its maximum when the surface induction is small on one side but large on the other side. In that case equation 7.6 reduces to

$$\int_{x_o}^{x_L} z_H(x)\,dx = h^*(1 - i\eta_L) \tag{7.7}$$

when we assume that $\eta_L \ll 1$ but $\eta_\phi \gg 1$. Table 2 shows that this applies to the land-sea interface at the California coast for the frequencies considered here. Thus, a simple integration over the in-phase Z-anomaly would have given us a direct estimate for the depth h^* of the underlying perfect conductor, and a corresponding integration over the out-of-phase Z-anomaly an estimate for the total conductivity on land. Unfortunately, this could not be done since the seaward continuation of the coastal anomaly remained inaccessible.

The numerical relaxation has been carried out with 48 grid points, spaced 40 km apart and extending from $-x_o = 960$ km offshore to $x_L = 920$ km inland. The illustrations show only the central portions of these profiles. We observe that the anomalous part $\tau_a(x)$ does not disappear at the continental end of the profiles. In order to avoid a computational "edge effect" the anomalous sheet current $j_a(x)$ has been extended analytically to infinity, using the ultimate value $j_a(x_L)$.

The relaxation was started for $f = 0.5$ cph with the "steady-state" approximation (6.12) by setting

$$q_H(x) = \tau_a(x)/\tau_\phi(x) \cdot Q_\phi .$$

The higher approximations converged and the illustrations display the resulting coastal anomaly after the 8th cycle. The numerical integrations involved have been carried out with the trapezoidal formula and with Hartmann's approximation (3.39) for Kertz's operator.

For the frequencies $f = 1$, 2, and 4 cph a 1st approximation of $q_H(x)$ was derived differently by assuming a perfectly conducting ocean off the coast. Hence, we used $q_H(x) = -Q_\phi$ for $x > 0$ and the current distribution of equation 6.25, referring to the extreme edge model of figure 38, for $x < 0$. During the 1st cycle the numerical integration over $z_H(x)$ was started just inland of the coast to avoid the edge singularity, and for each subsequent cycle one grid point toward the sea was added and included in the relaxation procedure.

The boundary condition (7.4) for the ultimate grid point on land provided us with an effective control for the precision of these calculations. It was found that $q_H(x)$ merges smoothly into $Q_L - Q_\phi$ for $x \to x_L$ as required, thereby linking the normal induction on the oceanic and continental sides properly. A remaining small discrepancy of less than 1% could have been removed probably by using a finer grid.

The theoretical z_p- and h_p-curves of the illustrations are normalized with the normal plus anomalous horizontal variations at the reference stations Auburn (figs. 40, 43), Fresno (figs. 41, 42, 44), and Cameron (fig. 45) to facilitate the comparison of model calculations and observations (cf. comment in sec. 4.4 regarding this point).

7.4 Inland Anomalies in California and Nevada

Some of the inland anomalies mentioned in section 4.5 can be explained by nonuniformities near the surface but others cannot. Let us begin with the San Joaquin valley in central California (fig. 21). Its sediments have been represented in the models by a conductive slab, 100 km wide and having a total conductivity of $1.2 \cdot 10^{-6}$ emu · cm. This is three times more than the continental average value of equation 7.2b and equivalent to 6000 m of sediments with 5 Ωm resistivity. Since the valley is 1000 km long but less than 150 km in width, we may treat it as a 2-dimensional structure (App. III). The Sierra Nevada and its igneous rock formations form an adjoining slab of zero conductivity.

The computed zp-curves on the basis of these values explain rather well the anomalous behavior of Z-variations near the edges of the San Joaquin valley. Particularly striking is the agreement between observations and model calculations for the out-of-phase zp-profiles at low frequencies (except for a constant displacement). Hence, this inland anomaly can be derived from the superficial conductivity contrast between the San Joaquin valley and the Sierra Nevada, using reasonable values for their total conductivities. If there should exist an additional deep-seated change in conductivity, its effect would be masked by the coincident superficial gradient.

The model calculations do not explain the highly anomalous behavior of Z-variations between Napa and Davis at 2 and 4 cph (fig. 40). It seems to be connected with a local rise in mantle conductivity which has not been encountered on the profile Monterey-Bridgeport further south.

There remains also the consistent misfit of the observed and computed z_p-profiles along the eastern slope of the Sierra Nevada which can be recognized on all profiles. We observe that the in-phase z_p-values drop off more rapidly toward inland than expected from the computed curves and that they reverse their sign eastward of the Sierra Nevada (CAC, BRI, BIS). This suggests that an anomalous concentration of surface or subsurface induction currents exists parallel to the Sierra. Since z_p is positive again at Fallon, Nevada, which is just 100 km east of Carson City, the internal current concentration must be rather narrow.

There is no geological evidence for a marked change in surface conductivity between the Sierra Nevada and the adjacent Basin and Range province. We conclude therefore that subsurface currents are involved which are drawn into a bulge of high mantle conductivity eastward of the Sierra (fig. 47). If we compare the inland portions of the profiles San Clemente-Yuma (fig. 45) and Farallon Islands-Fallon (fig. 40), we notice a certain similarity between

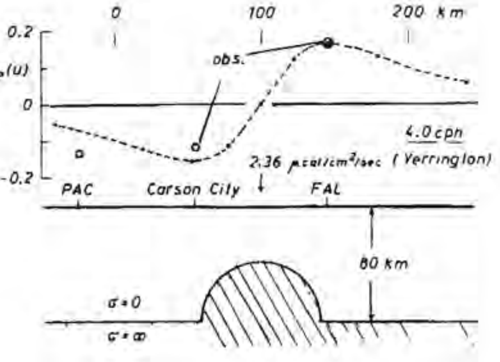

Fig. 47. Reversal of fast Z-variations between Carson City and Fallon, Nevada (cf. figs. 15 and 21). Empirical in-phase transfer values z_p for f = 4 cph (from fig. 40) are compared with the anomalous surface field (dashed curve) above the indicated semicircular elevation of perfectly conducting matter. Its "normal" depth of 80 km has been chosen in accordance with the interpretation of the coastal anomaly for this frequency. The terrestrial heat flow value is from Roy (1963).

El Centro and Yuma on the southern profile and between Carson City and Fallon on the northern profile. Hence, we may expect similarly high conductivities at shallow depth under the Imperial valley which may or may not be connected with those eastward of the Sierra Nevada.

These hypothetical zones of high internal conductivity show a distinct correlation to high terrestrial heat flow and young vulcanism, supporting the postulated correlation between ambient temperature and electrical conductivity in the earth's upper mantle (sec. 1.4). Von Herzen (1963) reported for the Gulf of California higher than normal heat flow values, ranging from 2.8 to 4.2 μcal/cm^2/sec in the upper part of the Gulf, which could continue into the Imperial valley. Further north Roy (1963) found high heat flows at Barstow, California (2.1) and at Yerrington (2.36) in comparison to Benfield's (1947) normal value at Bakersfield in the San Joaquin valley. Notice that Barstow and Yerrington lie above the hypothetical high conductivity channel along the eastern slope of the Sierra (figs. 21 and 47). The high conductivity zone between Napa and Davis northeast of San Francisco coincides with "The Geysers" in the northern Coast Range of California, an area of Quaternary vulcanism and still active hot springs and fumaroles (McNitt, 1965, pp. 245, 248-249).

7.5 Rio Grande Anomaly

The anomaly of geomagnetic variations in southern New Mexico and West Texas occurs at the boundary of two major structural provinces in North America (secs. 4.2 and 4.3). The Southern Arizona and New Mexico Rockies are parts of the Laramide Cordillera, an area of great tectonic instability with an "eventful and diversified igneous history which began in Cretaceous time and continued from place to place to the present." Particularly the Rio Grande rift belt in New Mexico is noted for its intensive Tertiary vulcanism (fig. 48). The Texas Foreland east of the Rio Grande represents a "fairly stable region with practically no igneous activity since Precambrian time" (Eardley, 1962, chaps. 15, 25, 27).

Let us consider first the surface conductivities along the profile Tucson-Sweetwater. West Texas contains a series of Permian basins and platforms with up to 3000 m of rather undeformed Permian sediments. Green and List (1963) reported for the Fort Worth basin a total conductivity of $0.24 \cdot 10^{-6}$ emu · cm which is equivalent to 60 m of seawater. They inferred this value from magnetotelluric soundings in conjunction with bore-hole measurements. We may assume similar conductivities in the Delaware and Midland basins between the stations Sweetwater and Cornudas.

Inserting this value of τ and $f = 1$ cph in (6.5) gives $2\pi\bar{j}/H = 0.005 + i \cdot 0.05$ for $h^* = 200$ km, which suggests that superficial eddy currents contribute here only a minor out-of-phase component to the internal bay field. Corresponding estimates for New Mexico and Arizona are difficult. The southern Arizona Rockies consist mainly of Precambrian rocks of presumably high resistivity. Further eastward between Lordsburg and Cornudas the profile crosses a number of Laramide uplifts, exposing Paleozoic and Precambrian formations, various Cenozoic rift valleys filled with Quaternary deposits, and interspersed young intrusives. In summary, we have to expect a variable superficial conductivity distribution, but the mean total conductivity of the whole area should be smaller than in West Texas.

We conclude therefore that the predominantly in-phase Rio Grande anomaly of bay-type disturbances has a deep-seated cause. We could postulate, for instance, distinct conductivity contrasts in a certain subsurface level--an interpretation that is favored by Caner et al. (1967)--or assume that less pronounced lateral nonuniformities prevail in a large portion of the upper mantle. With the second concept in mind we apply the evaluation method of section 6.6 to the Rio Grande anomaly and derive from the in-phase part of the anomalous surface field at 1 cph the hypothetical surface of a perfect substitute conductor.

Figure 48 shows the projected in-phase transfer values for this frequency. Evidently, the step model from figure 39 provides us with a suitable 1st approximation for the disturbed deep conductivity distribution. It explains properly the increasing Z-variations east of the Rio Grande, but it predicts a rather smooth decrease in Z toward Tucson contrary to the observed sharp reduction and partial reversal of Z between COR and LAC. A corresponding disagreement exists between the observed and calculated h_p-values for the anomalous part in D.

In order to improve the fit we develop the difference between the empirical z_p-values and the theoretical z_p-values of the step model into a series of three spatial harmonics with $2\pi/k_a = 1080$ km as fundamental wave length, using 25 grid points. The corresponding difference harmonics for h_p follow by interchanging the sine and cosine coefficients according to (3.34). This assures us that the harmonics describe a field of internal origin and that their depth dependence is $\exp(nk_a z)$ as indicated in (6.20).

The difference field is extended in this way downward and superimposed on the field of the step model, yielding with $Q^* = 1 - 2Q \approx 1$ the slope of the internal field lines at any subsurface point (6.21). An entire field line is

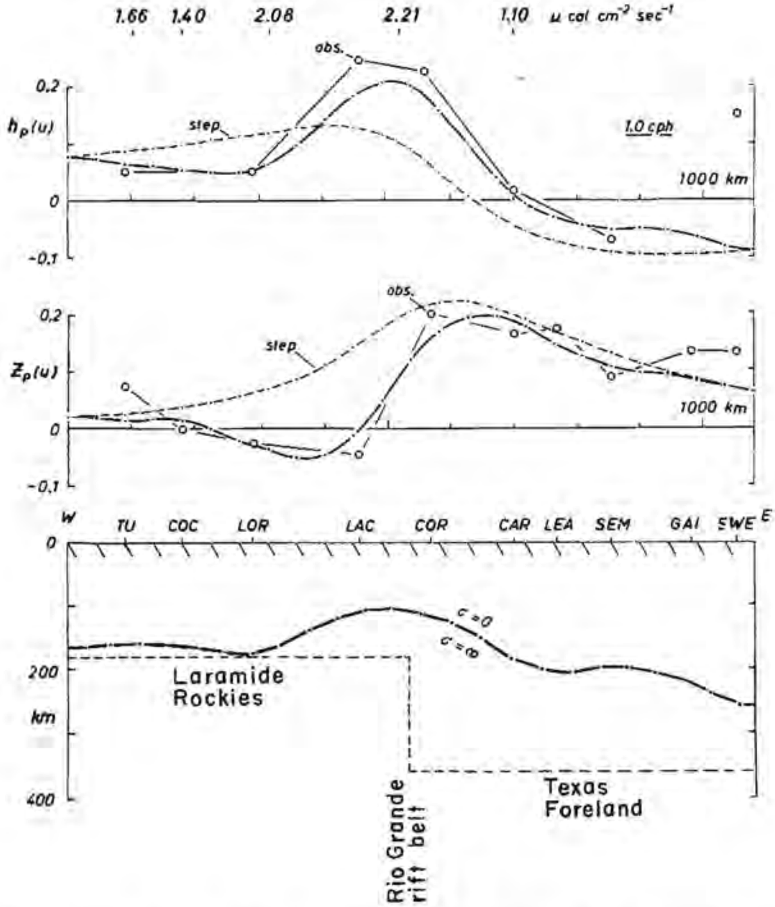

Fig. 48. Rio Grande anomaly of bays and its interpretation by an unequal deep conductivity distribution, using a perfect substitute conductor of variable depth. The upper diagrams contain as circles the empirical in-phase transfer values h_p and z_p for the profile Tucson-Sweetwater at 1 cph. They are compared with calculated h_p and z_p-profiles for the step model (light curves) and the undulatory interface (heavy curves) as shown in the cross section of the lower diagram. The correlation between high internal conductivities at shallow depth and high terrestrial heat flow at the Rocky Mountain front is evident (see text). Heat flow values are from Warren (1969) and Herrin and Clark (1956).

constructed by joining 25 pieces of slope according to the number of grid points as shown in figure 48, starting under Tucson at the "normal" depth $\overline{h}^* = 160$ km as inferred from the coastal anomaly (tab. 2). Fortunately, the resulting field line neither intersects the earth's surface nor the step model, and we may consider it to reflect the variable depth of penetration of bay-type disturbances along the profile.

The computed anomaly is of course smoother than the observed one, since only three spatial harmonics have been used to describe the difference field, the smallest wave length being 360 km. The inclusion of higher harmonics would have led to unrealistic fluctuations of the internal field lines.

We notice that the perfectly conducting interface rises from its initial value of 160 km under Tucson to 100 km under the Rio Grande Rift Belt in correspondence with the proposed high conductivity channel between Las Cruces and Cronudas (sec. 4.2). Further eastward the interface drops off to about 250 km depth under Sweetwater, reflecting a general reduction in mantle conductivity under the Texas Foreland in comparison to the mantle under the Laramide Rockies.

It is of course tempting to invoke at this point the presumed correlation between deep electric conductivity and ambient temperature (sec. 1.4). The Rio Grande Rift Belt and its young volcanics lie fittingly on top of a local rise in mantle conductivity, indicating an upward deflection of isotherms well within the earth's mantle. Furthermore, relatively high mantle temperatures under the Southern Arizona Rockies in comparison to the Texas Foreland would relate the different igneous and tectonic history of these two structural provinces to thermal imbalances deep within the earth.

To substantiate such far-reaching conclusions, Warren (personal communication) investigated the terrestrial heat flow in four bore holes between Tucson and Cornudas (fig. 48). He found that the heat flow increases indeed from 1.7 μcal/sec/cm^2 near Tucson to 2.2 at Orogrande (ORO) in the center of the Rio Grande Rift Belt. This agrees well with Decker's observations (1966) in the same area. Herrin and Clark (1956) reported for West Texas and eastern New Mexico an average heat flow of 1.1 from eleven oil wells, which is distinctly lower than the heat flow near Tucson.

We have to bear in mind that the terrestrial heat flow is the result of a very slow diffusion process from internal heat sources to the earth's surface, passing through rock formations of variable thermal conductivity. In particular near-surface strata form an insulating cover of great complexity. Furthermore, the heat flow in geothermal areas may or may not have reached thermal equilibrium, causing another ambiguity for the interpretation of heat flow data.

The evident correlation between high terrestrial heat flow and high internal conductivities in southern Arizona and New Mexico is therefore an encouraging result, suggesting that their common cause are deep-seated thermal imbalances. Even a quantitative correspondence seems to be indicated. Suppose the surface of the perfect substitute conductor represents a true isotherm within the earth, the earth's surface being a second one. Suppose that no heat sources exist between them and that thermal equilibrium has been reached. Then the constant temperature difference between the isotherms is $Q \cdot R$, when $Q = q \cdot dF$ denotes the heat flow passing through the surface element dF; R is the integrated thermal resistance of the "heat flow tube" in which the heat diffuses in the direction of the thermal gradient from the lower isotherm to the surface element dF.

We notice in figure 48 that the product heat flow per unit area times depth h^* of the perfectly conducting interface is nearly constant. This would establish the interface as true internal isotherm when we make the reasonable assumption that $R \sim h^*$.

Let us consider briefly which normal Z-amplitude of bays we have to expect in the southwestern states. By inserting the wave number of (7.1) and the depth values for 1 cph of table 3 in (5.54) we obtain $\overline{Z}/\overline{H} = 0.065$ for southern Arizona and $\overline{Z}/\overline{H} = 0.1$ for West Texas. If $\overline{Z}$ and $\overline{H}$ were completely unrelated among the analyzed bays, the normal Z-amplitude would be contained in the residual ϵ_Z of the correlation analysis. However, the unchanging positive northward gradient of the horizontal bay amplitude suggests that $\overline{Z}$ has some correlation to the normal parts in H and D, leading to a certain "normal contamination" of the transfer functions z_H and z_D. The larger than expected z_P-values at Tucson and Sweetwater in figure 48 could find in this way a simple explanation.

Table 3 contains also h^*-values in reference to the 2nd and 3rd time harmonic of diurnal variations, which have been obtained as follows: Since the survey stations lie in the range of maximum diurnal Z-variations, we derive from their relative amplitude and phase a "local" estimate for the diurnal ratio of internal to external parts. The empirical Z/Y ratios of figure 12 may be equated with the $-H_r/H_\phi$ ratio in equation 5.14 which when solved toward S_n^m yields

$$S_n^m = \frac{n \sin\theta + im\, Z/Y}{(n+1)\sin\theta - im\, Z/Y} \tag{7.8}$$

with the Z/Y ratio of the mth harmonic and $n = m + 1$ (sec. 7.1). The angle θ is set to 50° in accordance with the mean magnetic colatitude of the survey stations.

The resulting complex value for S_n^m is interpreted in terms of a uniform conducting sphere of the radius ρA (A: earth's radius, $\rho \le 1$). The pertinent induction parameter η_n from (5.50) is determined uniquely by the argument of S_n^m and can be inferred from the induction curves of figure 30. The modulus of S_n^m for this value of η_n should yield when multiplied by ρ^{2n+1} the modulus of the empirical ratio from (7.8). This allows the determination of ρ itself. The depth of the perfect substitute conductor follows then from its definition in (5.56) as

$$h^* = A\left[1 - \rho + \frac{\rho}{(2n+1)\eta_n}\right] . \tag{7.9}$$

The resulting depth values in table 3 are of the expected magnitude for the deeply penetrating Sq-variations, even though they are unusually small in southern Arizona (Tucson). This confirms once more the presence of highly conducting mantle material beneath the southern Rockies.

Let us state in conclusion possible conductivity distributions which are compatible with the empirical h^*-values as function of frequency. For that purpose we derive $G_1(0)$ from equation 5.44 for a presumed multilayered plane distribution and obtain in conjunction with (5.52) theoretical h^*-values as function of frequency. Obviously, Lahiri and Price's model "e" (sec. 1.3) has to be ruled out since it would give $h^* = 600$ km for all frequencies. Model "d", on the other hand, involving a continuous rise in conductivity throughout the upper mantle (fig. 1), leads to h^*-values which are comparable to those east of the Rio Grande. A modified distribution d^* would explain the reduced h^*-values west of the Rio Grande and under the California coast. This distribution is characterized by threefold increased conductivities between 50 and 300 km depth (fig. 49).

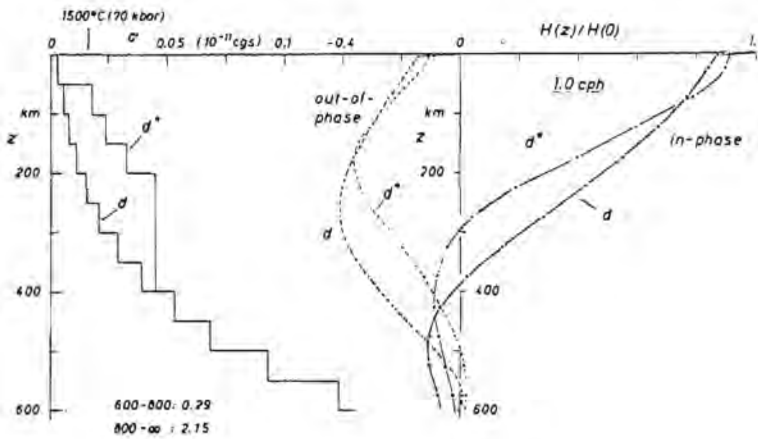

Fig. 49. Conductivity models for the upper mantle beneath the California coast/southern Arizona (model "d"*) and beneath West Texas (model "d"). The downward attenuation of horizontal H-variations within these distributions is shown in the right diagram for $f = 1$ cph (bays) and $k = 0$, using the indicated 14-layer models plus a continental cover with $0.4 \cdot 10^{-6}$ emu·cm as total conductivity of (cf. fig. 1).

What change in ambient temperature would correspond to this increase of conductivity? Suppose σ_2 and σ_1 are mantle conductivities at the same subsurface level and thereby under the same pressure, but at the different temperatures $T + 1/2\ dT$ and $T - 1/2\ dT$. It is readily verified from (1.13) that for $dT \ll T$

$$dT/T = T/T_o \cdot \ell n\,(\sigma_2/\sigma_1)\,. \tag{7.9}$$

Setting $T_o = 32,000$°K, $T = 1700$°K and $\sigma_2/\sigma_1 = 3$ yields $dT = 100$° C. Hence, we may expect that the mantle temperature between 50 and 300 km depth is about 100°C higher under the southern Rockies than in a corresponding level under the Texas Foreland with a local upwelling of very hot material under the Rio Grande Rift Belt.

These conclusions are supported by seismic observations concerning the velocity and attenuation of compressional P_n waves in the upper mantle. Herrin and Taggart (1962) and Pakiser (1963, 1965) reported that the spatial variations of P_n velocities follow a certain regional pattern. High velocities between 8.0 and 8.5 km/sec are commonly found in the Great Plains and low velocities between 7.5 and 8.0 km/sec prevail in the Basin and Range Province (fig. 50). They suggested that these low P_n velocities are associated with high mantle temperatures under the Basin and Range Province, of which the southern Arizona Rockies are a part.

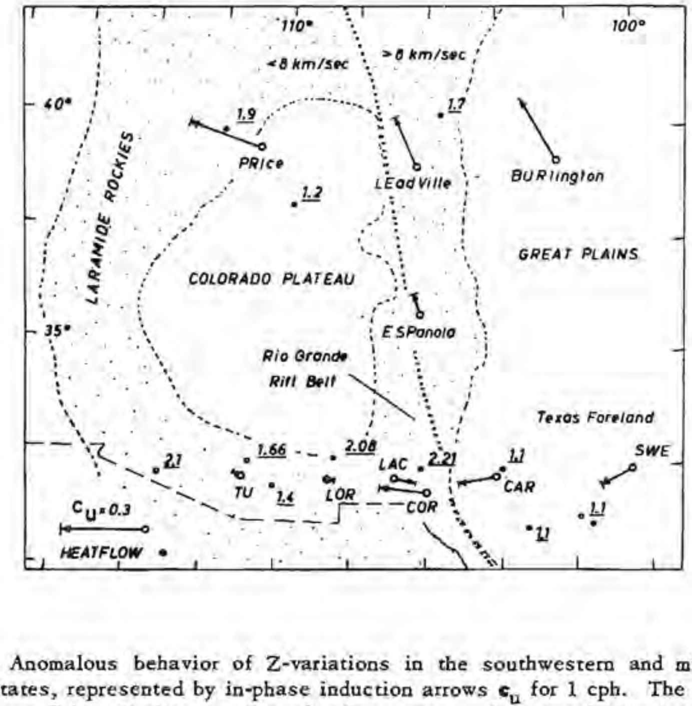

Fig. 50. Anomalous behavior of Z-variations in the southwestern and midwestern United States, represented by in-phase induction arrows $\mathbf{c}_u$ for 1 cph. The arrows at the stations Price, Burlington, Cornudas-Sweetwater point toward high internal conductivities beneath the Laramide Rockies which are distinguished also by higher than normal heat flow values. The dotted line, drawn according to Pakiser and Zietz (1965), refers to the indicated change of velocity of seismic P_n waves. Heat flow values from Bell and Roy (1965; 2.1), Warren (1969; 1.66, 1.4, 2.08, 2.21), Herrin and Clark (1956; 1.1, 1.1, 1.1), Roy (1963; 1.9), and Birch (1950; 1.2, 1.7).

Jordan et al. (1965) contoured the (normalized) amplitude of P_n and P waves in the United States, using teleseismic events and nuclear explosions. They found distinct and reproducible zones of high and low seismic amplitude. West Texas, for instance, stands out clearly as a region of higher than normal amplitude, while the western half of New Mexico appears as low-amplitude anomaly and thereby as a zone of unusually large attenuation of seismic signals.

The Rio Grande anomaly becomes in the light of these new discoveries just one particular geophysical symptom among others showing that a distinct change of upper mantle conditions occurs at the eastern border of the southern Rocky Mountain system. Lambert and Caner (1965) reported that a similar anomaly has been found in Canada and a pilot survey by Reitzel (1967) confirmed its existence at the Rocky Mountain front in Colorado. The situation seems to be more complicated in northern New Mexico where the transition from small to large Z-amplitudes occurs further east than expected (Caner et al., 1967). We may nevertheless conclude with the statement that the Rio Grande anomaly may be regarded as a general characteristic for the eastern margin of the Rocky Mountains in North America.

CONCLUSIONS AND SUGGESTIONS FOR FURTHER WORK

This survey established a clear correspondence between deep conductivity anomalies, as deduced from induction anomalies of geomagnetic variations, and geothermal anomalies, characterized by high terrestrial heat flow, volcanic activity, and tectonic instability in recent times. A similar correspondence seems to emerge for the Hungarian basin which, as stated by Boldizsar (1964), is "an isolated geothermic high, surrounded by the geothermically normal territories of central and eastern Europe." This agrees well with the anomalous behavior of geomagnetic variations in the same area as reported by Wiese (1963) and Adam et al. (1964). On the other hand, some distinct anomalies such as the absence of fast Z-variations at Mould Bay in the Canadian Arctic Archipelago (Witham, 1963) do not seem to have a clear relation to subsurface conditions (Law et al., (1965).

Only modest attempts have been made to deduce quantitatively the disturbed internal conductivity distribution beneath local induction anomalies. Finite conductivities in the upper mantle have been represented by a perfect substitute conductor at a certain depth, since there is little point in using but the simplest model as long as the prevailing "normal" conductivities in the upper mantle between, say, 50 and 250 km are insufficiently known.

Here new insight could come from magnetotelluric observations, provided the distorting effect of superficial conductivity contrasts is not the predominant feature. Thus, earth-current observations at selected sites, chosen for their stratified near-surface conductivity structure, could support conclusions drawn from the anomalous behavior of magnetic variations. Such observations have been made for many years at the Tucson Magnetic Observatory of the Coast and Geodetic Survey.

A regional separation of the bay field into external and internal parts could yield in a similar way the average change of conductivity with depth. Thus, Rikitake's investigations (1950) should be repeated, using the more closely spaced magnetic observatories now available and omitting those with obviously anomalous Z-variations.

Even though the anomalies encountered during the survey have been studied in fair detail with magnetic recording stations at fifty sites, additional field work is needed to clarify their correlation to other geophysical and geological evidence for deep-seated nonuniformities in the upper mantle. In particular the Rio Grande anomaly deserves further studies because of its connection with the Rocky Mountain system. Thus, an east-west profile of stations is suggested which crosses the Colorado Rockies and the Colorado Plateau, extending eastward into the Great Plains and westward into the Central Rockies. Attention should be paid also to anomalous east-west differences of diurnal Z-variations which were so obvious on the profile Tucson-Sweetwater (fig. 12). The observations are carried out preferably during the equinoxes when the external Sq-field is symmetric to the equator and well described by the single spherical term P_{m+1}^{m} for the m^{th} time harmonic.

Even though there is sufficient evidence for an uplift of highly conductive mantle material along the eastern slope of the Sierra Nevada, additional cross profiles extending deep into the state of Nevada are needed to outline this anomaly. Observations in the Mojave desert further south could prove or disprove the suggested connection with high internal conductivities under the Imperial valley (sec. 7.4).

Great efforts have been made to investigate the coastal anomaly in southern and central California. Its interpretation as "edge effect" of oceanic induction currents led to estimates for the deep conductivity structure beneath the continent, leaving the more complex structure off the coast to further observations at sea. Of particular interest would be the attenuated horizontal component of magnetic variations at the sea floor. It is a direct measure for the strength and phase of induction currents in the ocean and thereby for the conductivity distribution beneath the sea floor because of the inductive coupling between both conductors.

This attenuation can be determined with two recording total-field magnetometers, one moored at the surface and the second operating concurrently at the sea floor. We may presume that the variations in Z are the same at the surface and at the sea floor, when the bottom topography is sufficiently flat. Consequently, the difference of the total-field records would reveal the attenuation of the H-variations. Another sensitive indicator for deep conductivities would be the amplitude and phase of diurnal Z-variations as observed at some distance from coastlines. Observations of this kind would give new insight into the conductivity distribution beneath oceans which may or may not conform with the distribution under continents.

ACKNOWLEDGMENT

I am indebted to Professor Victor Vacquier for the initiation of the survey and his continuous support, to Drs. C. S. Cox, J. Filloux, and J. Larsen for helpful discussions and the extension of the survey toward the sea. Mr. M. P. Richards read the manuscript in various versions and gave valuable advice. I thank also Messrs. R. H. Frische, J. Santone, P. Kelly, J. Mulkey, K. Broomley, and J. Borden for their assistance during the field work and for their help with the analysis of the data and the preparation of the illustrations. The survey would not have been possible without the cooperation of many persons at the various field stations throughout the southwestern states. The Askania variographs were lent by the United States Coast and Geodetic

Survey. This work was supported by grant No. 6286 of the National Science Foundation. The numerical calculations have been carried out on the 3600 CDC computer of the computer center, University of California at San Diego.

APPENDIX I (To Section 3.6)

Trend Functions for the Long-periodic Background of Single Events

Let ΔH be the difference between the last and the first value H_j of the trace $H(t)$, which has been scaled within an interval from $t = -T_o/2$ to $t = +T_o/2$. We distinguish two limiting cases:

a. The trace returns outside of the interval smoothly to its previous undisturbed level. This trend shall be approximated by the probability function

$$H'(t) = \Delta H \cdot \exp[-a^2(t - T_o/2)^2]$$

which has the Fourier transform

$$C_{H'}(f) = \frac{\sqrt{\pi}}{a} \cdot \Delta H \cdot \exp[-(\pi f/a)^2 - i\pi f T_o] .$$

Setting $a = 2/T_0$ (fig. 51a) and $\Delta H \cdot T_0/2 = c$ gives

$$C_{H'}(f_o) = -0.15\ c \qquad C_{H'}(2f_o) = +0.0001\ c$$

as trend corrections for the first two harmonics in equation 3.9.

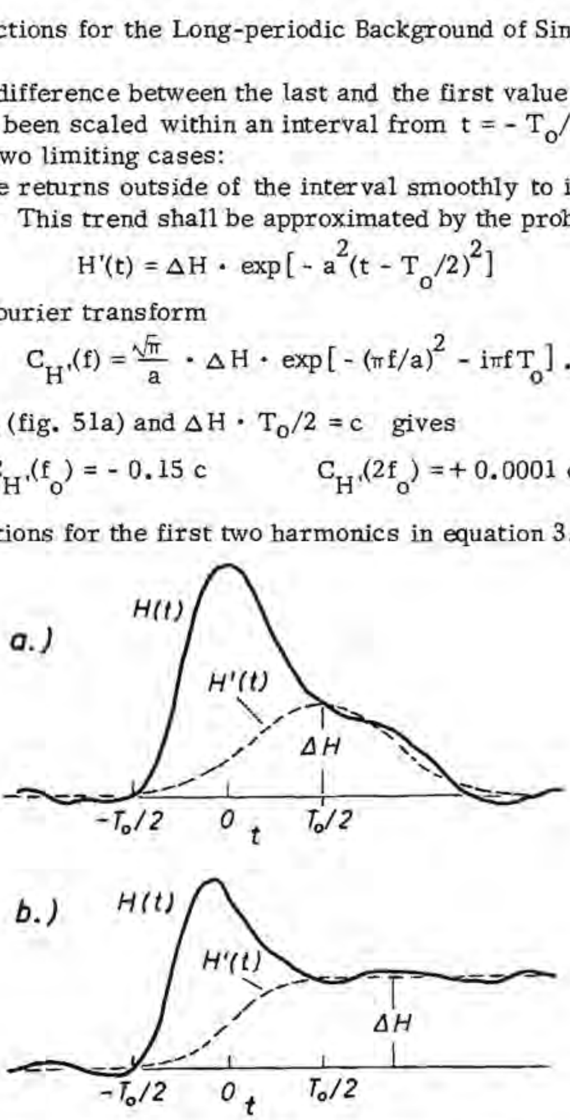

Fig. 51. Single events and analytic trend functions.

b. The trace does not return to its previous level. We approximate this stepwise change in the background by the error function

$$H'(t) = \frac{\Delta H}{2}\,[\,1 + \mathrm{erf}(a\sqrt{\pi}t)]$$

which has the transform

$$C_{H'}(f) = \frac{\Delta H}{2\pi i f}\,\exp(-\pi f^2/a^2).$$

Setting again $a = 2/T_o$ (fig. 51b) and $\Delta H \cdot T_o/2 = c$ gives the trend corrections

$$C_{H'}(f_o) = -\,i \cdot 0.15\;c \qquad C_{H'}(2f_o) = -\,i \cdot 0.007\;c\;.$$

APPENDIX II (To Section 5.2)

Spherical Bessel Functions

Spherical Bessel functions of the argument $u = i \cdot z$ are defined by modified Bessel functions $I_r(z)$ of fractional order:

$$j_n(u) = \sqrt{\frac{\pi}{2z}}\, i^n I_{n+1/2}(z) \qquad \eta_n(u) = \sqrt{\frac{\pi}{2z}}\, i^{n+1} I_{-n-1/2}(z)$$

Recurrence formulae: $f_n(u)$: $j_n(u)$, $\eta_n(u)$

$$f_{n+1} = \frac{2n+1}{u} f_n - f_{n-1}$$

$$\frac{df_n}{du} = f_{n-1} - \frac{n+1}{u} f_n \, .$$

Representation by hyperbolic functions:

$$j_o = \frac{\sinh z}{z} \qquad \eta_o = i\,\frac{\cosh z}{z}$$

$$j_1 = i\left(\frac{\cosh z}{z} - \frac{\sinh z}{z^2}\right) \qquad \eta_1 = \frac{\cosh z}{z^2} - \frac{\sinh z}{z}$$

Approximation for small arguments ($|z| \ll 1$):

$$j_n \approx \frac{u^n}{1 \cdot 3 \cdot 5 \cdot \cdots (2n+1)} \qquad \eta_n \approx -\frac{1 \cdot 3 \cdot 5 \cdot \cdots (2n-1)}{u^{n+1}}$$

Approximation for large arguments ($|z| \gg 1$, $n \ll |z|$, $|\arg. z| < \pi/2$):

$$\eta_n \approx i j_n \approx i^{n+1}\,\frac{e^z}{2z} \cdot \left[1 - \frac{n(n+1)}{2z} \pm \cdots\right] \, .$$

APPENDIX III (To Section 6.3)

Elliptic Surface Anomalies

Let $\bar{j}$ denote the sheet-current density of a uniform and stationary current which flows in a thin sheet of the total conductivity $\bar{\tau}$. The sheet forms the (x, y) plane of Cartesian coordinates and the current flow is in the direction of the positive x-axis. Let there be an elliptic area of different total conductivity $(\bar{\tau} + \tau_a)$, centered at the point of origin with the half-axes a and b (fig. 52). The resulting distortion of the sheet current is described by a superimposed anomalous current field $j_a(x, y)$. It is nondivergent and the superposition $(j_a + \bar{j})$ obeys the refraction law of field lines at the boundary of the elliptic area:

$$\mathrm{tg}\,\beta^{-}/\mathrm{tg}\,\beta^{+} = (\bar{\tau} + \tau_a)/\bar{\tau} = \lambda \;.$$

Here β denotes the angle between the current vector and the direction normal to the elliptic boundary at the inner (-) and outer (+) side.

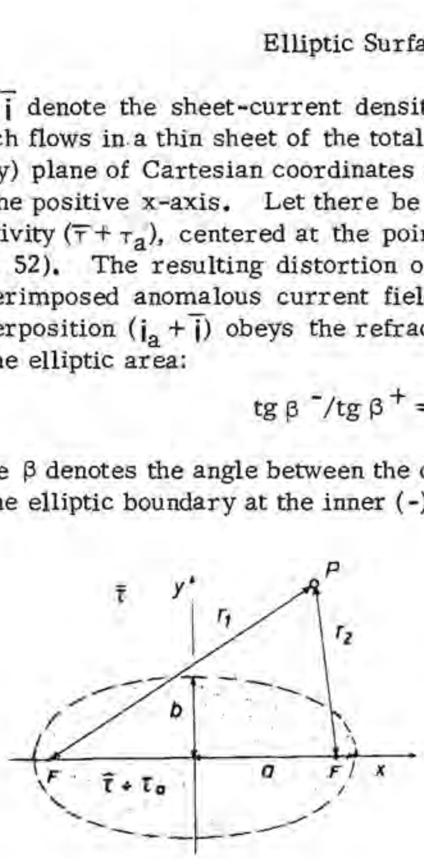

Fig. 52. Elliptic surface anomaly.

Solutions for the pertinent anomalous current function ψ_a are known. Let (η, ϕ) be elliptic coordinates, where

$$x = \alpha \cosh \eta \cos \phi \qquad y = \alpha \sinh \eta \sin \phi$$
$$\alpha^2 = a^2 - b^2 \qquad -\pi \le \phi \le \pi$$
$$\eta \ge 0$$

so that $\eta = \eta_o = \tanh^{-1}(b/a)$ defines the elliptic boundary. Then the inside and outside solutions are

$$\psi_a = \bar{j}\, C \sin\phi \begin{cases} \alpha \sinh \eta & (\eta \le \eta_o) \\ b \exp(\eta_o - \eta) & (\eta \ge \eta_o) \end{cases}$$

with

$$C = \frac{(\lambda - 1)a}{a + \lambda b} \; .$$

At a point P(x, y) inside the elliptic area the resulting anomalous current-density vector has the Cartesian components

$$j_{ax} = \bar{j} \cdot C \qquad\qquad j_{ay} = 0$$

which implies the well-known fact that the current here remains uniform and parallel to x. Outside the elliptic area

$$\left.\begin{array}{l} j_{ax} = \dfrac{y_o^3 x^2 - y^2 x_o^3}{x_o + y_o} \\ j_{ay} = x_o y_o xy \end{array}\right\} \cdot \bar{j}\, \frac{bC(a+b)}{x_o^4 y^2 + y_o^4 x^2}$$

where x_o and y_o are the half-axes of the confocal ellipse which passes through P. They can be found graphically from

$$2x_o = r_1 + r_2 \qquad \text{and} \qquad y_o^2 = x_o^2 - \alpha^2$$

when r_1 and r_2 denote the distances between P and the two foci, 2α being the distance of the foci (fig. 51). In the case of a circular anomaly of radius R, the anomalous current field is that of a 2-dimensional dipole with the moment $\bar{j}R^2(\lambda - 1)/(\lambda + 1)$. Ashour and Chapman (1965) gave a solution for the magnetic field which is connected with this current field.

The anomalous current component along the y-axis ($x = 0$, $y_o = y$) follows readily as $j_{ay} = 0$ and

$$j_{ax} = \bar{j} \cdot C \begin{cases} 1 & \text{(inside)} \\ \dfrac{-b\ (a+b)}{x_o(x_o + y)} & \text{(outside)} \end{cases}$$

reflecting the inside current concentration and the outside current dilution when $C > 0$, i.e., when the elliptic anomaly is better conducting than the surrounding sheet. When $a \gg b$ and λ is not very large, we obtain with $r^2 \approx a^2 + y^2$

$$j_{ax} = \bar{j} \cdot \tau_a/\bar{\tau} \begin{cases} 1 & \text{(inside)} \\ \dfrac{-\,ba}{r(r+y)} & \text{(outside)} \end{cases}$$

as approximation for elongated anomalies. It can be used in place of (6.12) as "steady state" approximation of the anomalous current distribution $q_H = j_a/\bar{j}$ (anomalies of the 1st kind) to give proper regard to the finite ratio of length to width of elongated anomalies.

APPENDIX IV

Computer Programs

The following programs are written in FORTRAN-63 and have been used on the 3600 Control Data Corporation computer of the University of California, San Diego. Numbers refer to equations in the text. Subr. = subroutine.

a. Error program GMVE.

Check of digitized time series for differences between adjacent values which exceed specified limit.

b. Analysis program GMV for single events (secs. 3.6, 8-11).

Harmonic analysis of single events as observed in three components at $n \leq 9$ survey stations (subr. HARMO); separation of anomalous and normal parts of observed variations, using one or more reference stations (subr. DIFRE); determination of power and cross-spectral values according to (3.10) for an assemblage of events (subr. COQUA and QUACO); determination of transfer values and residuals according to (3.22) and (3.17).

c. Program BLACKY (= UCSD library program G6) for analysis of storms (sec. 3.7).

Determination of power and cross spectra from auto and cross correlograms (lag functions); to be used in conjunction with program GMVBLA which computes the transfer functions between anomalous and normal parts of the analyzed storm according to (3.22) and (3.17).

d. Separation program KERTZO (sec. 3.16).

Evaluation of Kertz's operator (3.31) to separate a 2-dimensional field distribution, given at $n \leq 100$ nonequidistant points, into parts of external and internal origin according to (3.35). The linear interpolation formula (3.38) is used.

e. Induction program INDUSA (sec. 5.4).

Evaluation of spherical Bessel functions (App. II) for a given argument (iKa) to determine the ratio of internal to external parts above a uniform conductive sphere according to (5.49).

f. Induction program FINICO (sec. 5.3).

Determination of electromagnetic field distribution within a multilayered ($L \leq 80$) plane substratum. The calculations are carried out for $n \leq 20$ specified frequencies for a given wave number k of the source field according to (5.47, 48). The print-out contains also G(z) at interfaces, the depth h^* from (5.56) for a perfect substitute conductor and the apparent conductivity σ_c.

g. Induction program SHELCO (sec. 5.8).

Evaluation of (5.60) to determine the ratio of internal to external parts above a conductive shell and a layered core.

h. Induction program NONUNI for nonuniform thin sheets above perfect conductor (sec. 6.3).

Relaxation process to determine the anomalous current distribution within and the anomalous field distribution above a total conductivity profile, given at $n \leq 100$ equidistant points. The total conductivity merges near the ends of the profiles into constant values which are not necessarily equal (sec. 7.3). The numerical integrations of (6.8-11) are performed by the subroutines PRICE, CORE, and KERTZ. Various options exist to simulate the distant field distribution by suitable "analytical tails."

i. Internal field-line program LAPLAC (sec. 6.6).

Downward extension of a given 2-dimensional field distribution, given at $n \leq 720$ equidistant points, according to (6.20). The field is developed into a series of $m \leq 24$ spatial harmonics (subr. HARMOA), which after multiplication with the exponential depth factor for a certain subsurface level are converted again into the field distribution at that level (subr. SYNTHE).

j. Conformal mapping programs MODEL 1, 2, 3 (sec. 6.7).

Transformation of rectangular grids from the z-plane into the w-plane according to the mapping functions (6.23, 24, 26); to be used in conjunction with the programs FLDMD 1, 2, 3 to determine the transfer values h_H, z_H in the w-plane according to (6.22).

LITERATURE CITED

Adam, A., A. Wallner, and H. Wiese
1964. Elektrische Leitfaehigkeitsanisotropien des Untergrundes im Spiegel magneto-tellurischer und geomagnetischer Messungen, Gerlands Beitr. Geophys., vol. 73, pp. 310-316.

Akimoto, S., and H. Fujisawa
1965. Demonstration of the electrical conductivity jump produced by the olivine-spinel transition. J. Geophys. Res., vol. 70, pp. 443-449.

Ashour, A.
1965. The coastline effect on rapid geomagnetic variations. Geophys. J., vol. 10, pp. 147-161.

Ashour, A. A., and S. Chapman
1965. The magnetic field of electric currents in an unbounded plane sheet, uniform except for a circular area of different uniform conductivity. Geophys. J., vol. 10, pp. 31-44.

Bartels, J., N. H. Heck, and H. F. Johnston
1939. The three-hour-range index measuring geomagnetic activity. Terr. Magn., vol. 44, pp. 411-454.

Bell, P. M., and R. F. Roy
1965. Heat flow at Ajo, Arizona. Carnegie Institution of Washington, yearbook 64, pp. 150-153.

Benfield, A. E.
1947. A heat flow value for a well in California. Amer. J. Sci., vol. 245, pp. 1-18.

Birch, F.
1950. Flow of heat in the Front Range, Colorado. Bull. Geol. Soc. Amer., vol. 61, pp. 567-630.

Boldizsar, T.
1964. Terrestrial heat flow in the Carpathians. J. Geophys. Res., vol. 69, pp. 5269-5275.

Cagniard, L.
1953. Basic theory of the magnetotelluric method of geophysical prospecting. Geophysics, vol. 18, pp. 605-635.

Caner, B., H. W. Cannon, and C. E. Livingstone
1967. Geomagnetic depth sounding and upper mantle structure in the Cordillera region of western North America. J. Geophys. Res., vol. 72, pp. 6335-6351.

Chapman, S., and J. Bartels

1940. Geomagnetism. 3d impression. Oxford at the Clarendon Press. 1049 pp.

Chapman, S., and T. T. Whitehead

1923. The influence of electrically conducting material within the earth on various phenomena of terrestrial magnetism. Trans. Cambridge Phil. Soc., vol. 22, pp. 463-482.

Cox, C. S.

1960. Magnetic induction at oceanic margins. Unpublished manuscript. Scripps Inst. of Oceanography, La Jolla, Calif. 16 pp.

Decker, E. D.

1966. Crustal heat flow in Colorado and New Mexico. Trans. Amer. Geophys. Union, vol. 47, no. 1, p. 180 (abstract).

Eardley, A. J.

1962. Structural Geology of North America. 2d ed. New York: Harper & Row. 743 pp.

Eckhardt, D.

1963. Geomagnetic induction in a concentrically stratified earth. J. Geophys. Res., vol. 68, pp. 6273-6278.

Ertel, H.

1932. Theorie der durch Variationen des magnetischen Potentials induzierten Erdstroeme bei ungleichfoermiger Leitfaehigkeit der Erdrinde. Preuss. Meteorol. Inst. no. 391, Abh. 10, no. 2. 17 pp.

Filloux, J., and C. S. Cox

1966. A self-contained sea floor recorder of the electric field. J. Marine Res. (in press).

Filloux, J.

1967. Oceanic electric currents, geomagnetic variations and the deep electrical conductivity structure of the ocean-continent transition of central California. Ph.D. thesis, University of California at San Diego.

Fleischer, U.

1954. Charakteristische erdmagnetische Baystoerungen in Mitteleuropa und ihr innerer Anteil. Z. f. Geophysik, vol. 20, pp. 120-136.

Fukushima, N.

1953. Polar magnetic storms and geomagnetic bays. J. of the Fac. of Science, Univ. of Tokyo, Sect. II, vol. 8, pp. 293-412.

Green, A. W., and B. H. List

1963. The use of a total-field magnetometer in the magnetotelluric method of vertical resistivity profiling. J. Geophys. Res., vol. 68, pp. 869-875.

Hamilton, R. M.

1965. Temperature variation at constant pressures of the electrical conductivity of periclase and olivine. J. Geophys. Res., vol. 70, pp. 5679-5692.

Hartmann, O.
1963. Behandlung lokaler erdmagnetischer Felder als Randwertaufgabe der Potentialtheorie. Abhandl. Akad. Wiss. in Goettingen, Math.-Phys. Klasse. Beitraege zum Internationalen Geophysik. Jahr, no. 9. 50 pp.

Herrin, E., and S. P. Clark
1956. Heat flow in West Texas and eastern New Mexico. Geophysics, vol. 21, pp. 1087-1099.

Herrin, E., and J. Taggart
1962. Regional variations in P_n velocity and their effect on the location of epicenters. Bull. Seismol. Soc. Amer., vol. 52, pp. 1037-1046.

Hill, M. N., and C. S. Mason
1962. Diurnal variations of the earth's magnetic field at sea. Nature, vol. 195, no. 4839, pp. 365-366.

Hughes, H.
1955. The pressure effect on the electrical conductivity of peridotit. J. Geophys. Res., vol. 60, pp. 187-191.

Jordan, J., R. Black, and C. C. Bates
1965. Patterns of maximum amplitudes of P_n and P waves over regional and continental areas. Bull. Seismol. Soc. Amer., vol. 55, pp. 693-720.

Keller, G. V.
1966. Electrical properties of rocks and minerals, in S. P. Clark, ed., Handbook of physical constants, memoir 97, Geol. Soc. Amer., pp. 553-577.

Kertz, W.
1954. Modelle fuer erdmagnetisch induzierte elektrische Stroeme im Untergrund. Nachr. Akad. Wiss. Goettingen. Math.-Phys. Klasse, Abt. IIa, pp. 101-110.

Kertz, W.
1960. Leitungsfaehiger Zylinder im transversalen magnetischen Wechselfeld. Gerlands Beitr. Geophys., vol. 69, pp. 4-28.

Lahiri, B. N., and A. T. Price
1939. Electromagnetic induction in non-uniform conductors and the determination of the conductivity of the earth from terrestrial magnetic variations. Phil. Trans. Roy. Soc. London, A, vol. 237, pp. 509-540.

Lambert, A., and B. Caner
1965. Geomagnetic depth-sounding and the coast effect in western Canada. Canadian J. Earth Sci., vol. 2, pp. 485-509.

Larsen, J., and C. S. Cox
1966. Lunar and solar daily variations in the magnetotelluric field beneath the ocean. J. Geophys. Res., vol. 70, pp. 4441-4445.

Law, L. K., W. S. Paterson, and K. Witham
1965. Heat flow determinations in the Canadian Arctic archipelago. Canadian J. Earth Sci., vol. 2, pp. 59-71.

Matsushita, S.
1960. Studies of sudden commencements of geomagnetic storms using IGY data from United States stations. J. Geophys. Res., vol. 65, pp. 1423-1435.

McNitt, J. R.
1965. Review of geothermal resources, in W. H. K. Lee, ed., Terrestrial heat flow, Geophys. monograph series of Amer. Geophys. Union, no. 8, pp. 240-266.

Munk, W. H., F. E. Snodgrass, and M. J. Tucker
1959. Spectra of low-frequency ocean waves. Bull. Scripps Inst. of Oceanography, Univ. of Calif., vol. 7, no. 4, pp. 283-362.

Pakiser, L. C.
1963. Structure of the crust and upper mantle in the western United States. J. Geophys. Res., vol. 68, pp. 5747-5756.

Pakiser, L. C., and I. Zietz
1965. Transcontinental crustal and upper mantle structure. Rev. Geophys., vol. 3, pp. 505-520.

Parkinson, W. D.
1959. Direction of rapid geomagnetic fluctuations. Geophys. J., vol. 2, pp. 1-14.

Parkinson, W. D.
1962. The influence of continents and oceans on geomagnetic variations. Geophys. J., vol. 6, pp. 441-449.

Price, A. T.
1949. The induction of electric currents in non-uniform thin sheets and shells. Quart. J. Mech. and Appl. Math., vol. 2, pp. 283-310.

Price, A. T.
1950. Electromagnetic induction in a semi-infinite conductor with a plane boundary. Quart. J. Mech. and Appl. Math., vol. 3, pp. 385-410.

Price, A. T., and G. A. Wilkins
1963. New method for the analysis of geomagnetic fields and their application to the Sq field of 1932-33. Phil. Trans. Roy. Soc. London, A, vol. 256, pp. 31-98.

Reitzel, J.
1967. Magnetic deep sounding near the Rocky Mountain front: Preliminary results. Trans. Amer. Geophys. Union, vol. 48, no. 1, p. 210 (abstract).

Rikitake, T.
1950. Electromagnetic induction within the earth and its relation to the electrical state of the earth's interior. Bull. Earthquake Res. Inst., Tokyo Univ., vol. 28, pp. 45-100, 219-283.

Rikitake, T.
1959. Anomaly of geomagnetic variations in Japan. Geophys. J., vol. 2, pp. 276-287.

Rikitake, T.

1966. Electromagnetism and the earth's interior. Amsterdam-London-New York: Elsevier Publishing Co. 308 pp.

Rikitake, T., and K. Whitham

1964. Interpretation of the Alert anomaly in geomagnetic variations. Canadian J. Earth Sci., vol. 1, pp. 35-62.

Roden, R.

1964. The effect of an ocean on magnetic diurnal variations. Geophys. J., vol. 8, pp. 375-388.

Roy, R. F.

1963. Heat flow measurements in the United States. Ph.D. thesis, Harvard Univ.; through W. H. K. Lee, ed., Terrestrial heat flow, Geophys. monograph series, Amer. Geophys. Union, no. 8, p. 98.

Schmucker, U.

1959. Erdmagnetische Tiefensondierung in Deutschland 1957-59; Magnetogramme und erste Auswertung. Abhandl. Akad. Wiss. in Goettingen, Math.-Phys. Klasse. Beitraege zum Internationalen Geophysik. Jahr, no. 5. 51 pp.

Schmucker, U.

1964. Anomalies of geomagnetic variations in the southwestern United States. J. Geomagn. and Geoelectricity, vol. 15, pp. 193-221.

Schmucker, U., O. Hartmann, A. A. Giesecke, M. Casaverde, and S. E. Forbush

1964. Electrical conductivity anomalies in the earth's crust in Peru. Carnegie Institution of Washington, yearbook 63, pp. 354-362.

Siebert, M., and W. Kertz

1957. Zur Zerlegung eines lokalen erdmagnetischen Feldes in aeusseren und inneren Anteil. Nachr. Akad. Wiss. Goettingen, Math.-Phys. Klasse, Abt. IIa, no. 5, pp. 87-112.

Silsbee, H. C., and E. H. Vestine

1942. Geomagnetic bays, their frequency and current systems. Terr. Magn., vol. 47, pp. 195-208.

Srivastava, S. P.

1966. Theory of the magnetotelluric method for a spherical conductor. Geophys. J., vol. 11, no. 4, pp. 373-387.

Tozer, D. C.

1959. The electrical properties of the earth's interior, in L. H. Ahrens, ed., Physics and chemistry of the earth, vol. 3, pp. 414-436.

Untiedt, J.

1964. Ueber den linearen Zusammenhang zwischen den Komponenten erdmagnetischer Variationen und seine Bedeutung fuer die erdmagnetische Tiefensondierung. Nachr. Akad. Wiss. Goettingen II. Math.-Phys. Klasse, no. 1, pp. 1-24.

Von Herzen, H. P.
1963. Geothermal heat flow in the Gulfs of California and Aden. Science, vol. 140, pp. 1207-1208.

Waitt, J. R.
1953. Propagation of radio waves over a stratified ground. Geophys., vol. 18, pp. 416-422.

Warren, R. E.
1964. Micropulsation induction effects 15-40 seconds. Techn. report on Nonr. 222(89), Univ. Calif., Space Sciences Lab., Berkeley.

Warren, R. E., J. G. Sclater, Victor Vacquier, and Robert Roy
1969. A comparison of terrestrial heat flow and transient geomagnetic fluctuations in the southwestern United States. Geophys. (in press).

Weaver, J. T.
1963. On the separation of local geomagnetic fields into external and internal parts. Z. f. Geophys., vol. 30, pp. 29-36.

Weidelt, P.
1966. Modellrechnungen zur Deutung der norddeutschen Leitfaehigkeitsanomalie als oberflaechennahe Leitfaehigkeitsaenderung. Diplomarbeit Math. - Naturw. Fak. Univ. Goettingen. 121 pp.

Wiese, H.
1962. Geomagnetische Tiefentellurik Teil II: Die Streichrichtung der Untergrundstrukturen des elektrischen Widerstandes, erschlossen aus geomagnetischen Variationen. Geofisica pura e applicata, vol. 52, pp. 83-103.

Wiese, H.
1963. Geomagnetische Tiefentellurik Teil III: Die geomagnetischen Variationen in Mittel - und Suedost-Europa als Indikator der Streichrichtung grossraeumiger elektrischer Untergrundstrukturen. Geofisica pura e applicata, vol. 56, pp. 101-114.

Wiese, H.
1965. Geomagnetische Tiefentellurik. Deutsche Akad. Wiss. Berlin, Geomagn. Inst. Potsdam, Abh. Nr. 36. 146 pp.

Whitham, K.
1963. An anomaly in geomagnetic variations at Mould Bay in the Arctic archipelago of Canada. Geophys. J., vol. 8, pp. 26-43.

TABLE 1

Error Residuals in Z (Eq. 3.29)

f (cph)	0.5	1.0	1.5	2.0	4.0
ϵ_Z	0.07	0.11	0.16	0.21	0.42

TABLE 2

Normalized Sheet-Current Density in the Ocean (Q_ϕ) Offshore the California Coast and in Surface Layers on Land (Q_L). From equations 6.5 and 7.2.

Freq. (cph)	h* (km)	Q_ϕ		Q_L	
0.5	200	0.462 + i	0.132	0.004 + i	0.044
1.0	160	0.485	0.086	0.010	0.069
2.0	120	0.493	0.059	0.021	0.100
4.0	80	0.496	0.044	0.037	0.130

TABLE 3

Depth of Perfect Substitute Conductor h* in [km]

Freq. (cph)	Calif. coast and southern Arizona	West Texas	Model "d*"	Model "d" Lahiri and Price
1/12	430	630	400	600
1/8	300	520	-	-
1/2	200	-	190	280
1	160	250	150	210
2	120	-	120	160
4	80	-	90	120

TABLE 4

List of Survey Stations

Station	Symbol	Coordinates (°W, °N)	Magn. Decl. (Time of Op.)	Time of Operation
Profile: San Clemente Island, Calif.–Tucson, Ariz.–Sweetwater, Texas				
San Clemente Island, Calif.	SAC	118.5 33.0	14.5°E	1960 June 27 - Oct. 17
La Jolla, Calif.	LAJ	117.3 32.9	14.0°E	1960 June 22 - Oct. 24
El Cajon Calif.	ELA	117.0 32.9	14.0°E	1960 July 7 - Oct. 21
Alpine,* Calif.	ALP	116.7 32.8	14.0°E	1960 June 25 - Oct. 14
Cameron, Calif.	CAM	116.4 32.7	13.5°E	1960 July 8 - Oct. 14
El Centro, Calif.	ELC	115.6 32.9	13.5°E	1959 Nov. 19-Jan. 12 † 1960 Jan. 12 - Feb. 26
Yuma, Ariz.	YUM	114.6 32.7	13.5°E	1960 July 8 - Aug. 26
Tacna, Ariz.	TAC	114.0 32.7	13.5°E	1959 Sept. 21 - Nov. 20† 1960 Jan. 13 - Mar. 3
Sells, † Ariz.	SEL	111.9 31.9	13.5°E	1959 Sept. 22 - Oct. 14
Nogales, † Ariz.	NOG	110.9 31.4	13.5°E	1959 Sept. 7 - Sept. 26
Ray, † Ariz.	RAY	111.0 33.2	13.5°E	1959 Sept. 9 - Sept. 30
Tucson, Ariz.	TU	110.8 32.3	13.5°E	USC & GS Observatory
Cochise, † Ariz.	COC	109.9 32.1	13.0°E	1959 Sept. 8 - Oct. 12

TABLE 4 (contd.)

Station	Symbol	Coordinates (°W, °N)	Magn. Decl. (Time of Op.)	Time of Operation
Lordsburg,* N. M.	LOR	108.6 32.3	13.0°E	1959 Oct. 1 - Nov. 20† 1960 Jan. 21 - May 11
Las Cruces, N. M.	LAC	106.8 32.3	12.5°E	1959 Sept. 28-Nov. 24† 1960 Jan. 14 - June 17
Orogrande, N. M.	ORO	106.1 32.4	12.5°E	1960 May 12 - May 30
Cornudas, N. M.-Texas	COR	105.6 32.0	12.0°E	1960 Mar. 7 - May 31
Hope, N. M.	HOP	104.8 32.8	11.5°E	1960 May 16 - June 1
Carlsbad, N. M.	CAR	104.2 32.4	11.5°E	1960 Jan. 16 - June 16
Lea, N. M.	LEA	103.4 32.6	11.5°E	1960 June 2 - 16
Seminole, Tex.	SEM	102.7 32.7	11.0°E	1960 Jan. 18 - Mar. 16
Gail, Tex.	GAI	101.3 32.8	11.0°E	1960 June 3 - June 15
Sweetwater, Tex.	SWE	100.5 32.5	10.5°E	1960 Mar. 11 - June 15
Cisco, Tex.	CIS	99.0 32.5	10.5°E	1960 June 7 - June 14

Profile: Farallon Islands, California–Fallon, Nevada

Farallon Isl., Calif.	FAR	123.0 37.7	17.5°E	1960 Nov. 10 - 1961 July 7

TABLE 4 (contd.)

Station	Symbol	Coordinates (°W, °N)	Magn. Decl. (Time of Op.)	Time of Operation
Dillons Beach, Calif.	DIL	123.0 38.3	17.5°E	1960 Sept. 1 - June 12
Santa Rosa, Calif.	SAR	122.7 32.4	18.0°E	1961 April 25 - July 10
Napa, Calif.	NAP	122.3 38.3	18.0°E	1960 Dec. 20 - 1961 May 26
Williams, Calif.	WIL	122.2 39.2	19.0°E	1961 June 14 - Aug. 7
Davis,* Calif.	DAV	121.8 38.6	18.0°E	1960 Nov. 8 - 1961 April 24
Auburn, Calif.	AUB	121.1 38.9	18.0°E	1960 Dec. 14 - 1961 Sept. 4
Pacific Ranger Sta.	PAC	120.5 38.8	18.0°E	1961 July 15 - Aug. 16
Carson City, Nev.	CAC	119.8 39.2	17.5°E	1960 Dec. 15 - 1961 Sept. 1
Fallon, Nev.	FAL	118.8 39.5	18.0°E	1961 June 16 - Aug. 9

Profile: Monterey–Bridgeport, Calif.

Station	Symbol	Coordinates (°W, °N)	Magn. Decl. (Time of Op.)	Time of Operation
Monterey, Calif.	MON	121.4 36.6	17.0°E	1961 Aug. 11 - Nov. 21
Lick Obs., Calif.	LIC	121.7 37.4	17.5°E	1961 Sept. 11 - Nov. 9
Half Moon Bay, Calif.	HAB	122.5 37.5	18.0°E	1961 Aug. 12 - Oct. 28

TABLE 4 (contd.)

Station	Symbol	Coordinates (°W, °N)	Magn. Decl. (Time of Op.)	Time of Operation
Turlock Lake, Calif.	TUR	120.7 37.7	17.0°E	1961 Aug. 17 - 1962 Jan. 9
Bridgeport, Calif.	BRI	119.2 38.3	17.0°E	1961 Sept. 7 - Nov. 2

Profile: Cambria–Bishop, Calif.

Station	Symbol	Coordinates (°W, °N)	Magn. Decl. (Time of Op.)	Time of Operation
Cambria, Calif.	CAB	121.1 35.6	16.5°E	1961 Nov. 10 - 1962 Feb. 5
Paso Robles, Calif.	PAR	120.6 35.6	16.5°E	1961 Dec. 23 - 1962 Mar. 13
Coalinga, Calif.	COA	120.4 36.2	16.5°E	1961 Nov. 22 - 1962 Feb. 6
Fresno, Calif.	FRE	119.8 36.8	16.5°E	1961 Aug. 18 - 1962 Jan. 9
Yosemite, Calif.	YOS	119.7 37.8	17.0°E	1961 Nov. 1 - Dec. 21
Bishop, Calif.	BIS	118.4 37.4	17.0°E	1961 Nov. 3 - 1962 Feb. 2

Profile: Lompoc–Inyokern, Calif.

Station	Symbol	Coordinates (°W, °N)	Magn. Decl. (Time of Op.)	Time of Operation
Lompoc, Calif.	LOM	118.1 36.6	16.0°E	1962 Aug. 5 - Oct. 4
Taft, Calif.	TAF	119.5 35.2	16.5°E	1962 April 18 - Aug. 1
Porterville, Calif.	POR	119.0 36.1	16.5°E	1962 Feb. 7 - Mar. 12

TABLE 4 (contd.)

Station	Symbol	Coordinates (°W, °N)	Magn. Decl. (Time of Op.)	Time of Operation
Mojave, Calif.	MOJ	118.2 35.1	16.0°E	1962 Mar. 17-Sept. 21
Lone Pine, Calif.	LOP	118.1 36.6	16.0°E	1962 Feb. 3 - Mar. 15
Inyokern, Calif.	INY	117.8 35.7	16.0°E	1962 Mar. 16-April 17

IGY stations of the U. S. Coast & Geodetic Survey (1957-58)

Station	Symbol	Coordinates (°W, °N)	Magn. Decl. (Time of Op.)	Time of Operation
Price, Utah	PRI	110.8 39.6	15.5°E	
Leadville, Colo.	LED	106.3 39.3	13.5°E	
Casper Wyo.	CAS	106.4 42.8	14.5°E	
Espanola, N. M.	ESP	106.1 36.0	13.0°E	
Burlington, Colo.	BUR	102.3 39.4	12.0°E	
Beloit, Kan.	BEL	98.1 39.5	10.0°E	

* Uncontrolled temperature effect in Z.

† Low sensitivities in D and Z.

TABLES 5–10

Transfer Values between the Anomalous and Normal Parts of Bays and Other Fast Variations

The tables contain the results of the statistical correlation analysis between the anomalous parts H_a, D_a, Z_a and the normal parts $\bar{H}$, $\bar{D}$ of the observed variations. These normal parts are identical with the horizontal variations at the respective reference station, indicated by an asterisk (e.g., LOR*). The transfer values have been derived from an assemblage of N single events (except those in table 6Z*) according to equation 3.22. They are listed for the frequencies 0.5, 1, 2, 4 cph together with the respective residual (sec. 3.9) multiplied by 100 and arranged for each profile separately.

TABLE 5 Z

	0.5 cph						1.0 cph					
Station	$z_D(u)$	$z_H(u)$	$z_D(v)$	$z_H(v)$	ϵ_z	N	$z_D(u)$	$z_H(u)$	$z_D(v)$	$z_H(v)$	ϵ_z	N
TU	4	3	-1	6	.30	8	7	0	-2	-1	.43	8
LOR*	0	1	-6	8	.47	16	-2	-1	-7	2	.44	16
LAC	-1	3	-6	10	.42	12	-5	0	-11	6	.28	12
COR	15	1	10	10	.26	12	21	-2	5	5	.21	12
CAR	9	1	7	12	.33	12	17	2	3	6	.21	12
SEM	12	6	2	17	.23	5	9	1	4	17	.23	5
SWE	4	1	8	18	.44	12	11	6	10	9	.30	12
LEA	17	-5	-2	16	.20	5	15	6	-3	18	.14	5
GAI	12	-10	-3	11	.35	5	11	0	-4	13	.25	5
SWE*	8	-8	-3	12	.44	5	9	6	-2	16	.11	5
ELC	6	4	-7	2	.38	6	2	-2	-7	-5	.40	6
TAC*	8	6	0	6	.28	11	5	6	1	5	.30	11
SEL	9	4	1	5	.39	7	5	5	-2	6	.26	7
COC	6	-1	0	5	.38	6	0	2	3	8	.39	6
	2.0 cph						4.0 cph					
TU	-5	-5	-4	10	.80	8						
LOR*	-8	0	-5	3	.37	16	-14	3	3	2	.48	11
LAC	-18	7	-2	5	.32	10	-21	7	3	7	.27	10
COR	23	0	5	4	.23	12	12	6	2	-5	.42	8
CAR	21	8	1	4	.22	12	2	9	-9	-3	.43	10
SEM	15	6	1	5	.19	5	-3	0	-11	-11	.30	4
SWE	11	9	12	8	.32	12	-2	17	2	0	.25	8
ORO	11	12	3	3	.25	5	13	13	3	0	.23	5
HOP	18	7	-1	-2	.24	5	13	7	-7	-4	.12	5
SWE*	3	18	3	-4	.25	5	2	14	-2	-5	.19	5
ELC	-2	-10	-4	-8	.45	6						
TAC*	4	4	5	5	.69	11						
SEL	6	0	-6	-4	.61	7						
COC	1	-3	-6	-3	.76	6						

TABLE 5 H, D

	1.0 cph						1.0 cph					
Station	$h_D(u)$	$h_H(u)$	$h_D(v)$	$h_H(v)$	ϵ_h	N	$d_D(u)$	$d_H(u)$	$d_D(v)$	$d_H(v)$	ϵ_d	N
TU	-16	-4	7	-16	.74	8	0	13	2	-9	.71	8
LOR*	0						0					
LAC	11	0	1	-1	.31	12	18	0	17	-10	.32	12
COR	19	2	3	5	.31	12	15	-4	20	-7	.29	12
CAR	17	-9	1	4	.27	11	6	-10	18	-15	.37	12
SEM	14	2	1	5	.61	5	-10	-28	12	21	.38	5
SWE	31	-9	5	2	.24	12	7	-28	41	-23	.34	12
LEA	-4	10	-1	-7	.59	5	7	22	15	7	.41	5
GAI	-3	0	1	11	.87	5	7	1	2	5	.77	5
SWE*	0											
ELC	-4	10	14	1	.45	7	4	13	10	4	.75	7
TAC*	0						0					
SEL	12	-3	9	-5	.55	7	-2	-25	-6	2	.48	7
COC	12	2	4	-3	.38	6	1	-22	-12	7	.56	6

TABLE 6 Z* (magnetic storm)†

	0.5 cph						1.0 cph					
Station	$z_D(u)$	$z_H(u)$	$z_D(v)$	$z_H(v)$	ϵ_z	$\nu=24$	$z_D(u)$	$z_H(u)$	$z_D(v)$	$z_H(v)$	ϵ_z	$\nu=24$
SAC	12	17	-5	0	.35	(cf. 3.5)	13	14	-4	-6	.28	(cf. 3.5)
LAJ	25	22	11	15	.21		29	20	12	13	.16	
ELA	18	17	5	8	.29		20	14	5	5	.18	
ALP	13	10	-1	5	.36		14	10	1	2	.24	
CAM*	8	9	-4	3	.50		8	7	-3	0	.36	
	2.0 cph						4.0 cph					
SAC	13	5	-4	-12	.29		12	-7	-7	-11	.52	
LAJ	33	25	20	13	.19		39	22	24	2	.34	
ELA	21	14	10	3	.26		21	10	12	-5	.57	
ALP	13	8	4	1	.28		12	-1	4	-2	.54	
CAM*	6	4	0	-3	.55		5	1	2	-1	.83	

† Magnetic storm, shown in Plate II and analyzed for 12 succeeding hours; cf. section 4.6.

TABLE 6 Z

	0.5 cph						1.0 cph					
Station	$z_D(u)$	$z_H(u)$	$z_D(v)$	$z_H(v)$	ϵ_z	N	$z_D(u)$	$z_H(u)$	$z_D(v)$	$z_H(v)$	ϵ_z	N
SAC	23	17	4	-3	.29	12	18	14	0	-12	.22	12
LAJ	28	20	18	14	.21	13	30	25	17	9	.13	13
ELA	23	15	11	7	.24	11	21	17	9	2	.18	11
ALP	13	11	4	7	.16	10	15	11	3	-2	.23	10
CAM*	13	9	2	2	.40	13	8	8	0	-4	.38	13
YUM	15	7	10	5	.31	7	15	9	10	2	.34	7
TU	7	1	3	6	.34	8	4	2	-1	1	.44	8
	2.0 cph						4.0 cph					
SAC	9	6	-8	-19	.46	11	0	-13	-9	-12	.52	11
LAJ	32	32	20	9	.30	11	44	33	21	4	.29	11
ELA	26	13	6	7	.25	7	23	15	1	-4	.62	11
ALP	16	4	3	-7	.33	10	16	9	-1	-6	.51	11
CAM*	4	9	-2	-6	.65	11	6	2	-5	-7	.61	11
YUM	20	5	3	1	.33	7	19	16	11	-23	.22	3
TU												

TABLE 6 D, H

Station	$d_D(u)$	$d_H(u)$	$d_D(v)$	$d_H(v)$	ϵ_d	N	$h_D(u)$	$h_H(u)$	$h_D(v)$	$h_H(v)$	ϵ_h	N
					0.5 cph							
SAC	3	5	5	2	.88	12	-1	0	4	3	.87	12
LAJ	0	1	0	3	.89	12	3	1	2	-1	.86	12
ELA	-1	-6	0	1	.70	11	4	4	2	0	.78	11
ALP	-2	-3	1	0	.85	10	9	5	3	-5	.52	10
CAM*	0											
YUM	7	-11	3	6	.45	7	7	4	2	2	.79	7
TU	8	-21	7	3	.37	8	19	0	0	3	.31	8
					1.0 cph							
SAC	0	8	12	1	.70	12	7	5	3	0	.83	12
LAJ	1	1	7	4	.76	12	3	2	2	-3	.93	12
ELA	1	-8	6	2	.73	11	6	7	1	-4	.76	11
ALP	2	-1	5	0	.80	10	9	7	0	-8	.62	10
CAM*	0											
YUM	9	0	15	14	.45	7	18	6	0	-8	.56	7
TU	6	-7	17	1	.42	8	26	-2	1	1	.31	8

TABLE 7 Z

	0.5 cph						1.0 cph					
Station	$z_D(u)$	$z_H(u)$	$z_D(v)$	$z_H(v)$	ϵ_z	N	$z_D(u)$	$z_H(u)$	$z_D(v)$	$z_H(v)$	ϵ_z	N
FAR	48	31	10	13	.13	14	47	38	1	5	.13	14
DIL	50	21	9	6	.12	12	49	27	5	-1	.12	12
SAR	50	20	3	-8	.25	7	41	26	1	-11	.17	7
MAP	23	17	-5	7	.25	14	15	17	-10	2	.21	14
DAV	27	10	0	6	.20	13	24	14	0	2	.15	13
WIL	31	25	10	2	.31	5	33	23	4	-9	.13	5
AUB*	21	6	-5	3	.25	15	13	8	-4	-1	.23	15
PAC	11	7	-9	13	.37	6	8	0	-9	1	.30	6
CAC	11	3	-10	4	.40	12	-1	3	-11	-3	.29	12
FAL	14	11	1	11	.60	9	4	11	-3	13	.24	9
	2.0 cph						4.0 cph					
FAR	50	39	-5	-15	.14	9	30	31	-16	-12	.39	13
DIL	50	18	-2	-12	.27	12	39	13	-17	-12	.41	13
SAR	35	20	-3	-7	.24	6	20	10	-12	-9	.31	6
NAP	9	15	-17	-11	.23	10	-19	-1	-14	-8	.54	14
DAV	30	14	3	-10	.21	9	21	12	1	0	.54	13
WIL	19	10	-4	-3	.31	6	20	8	-4	0	.27	6
AUB*	16	4	-3	-8	.24	10	8	2	3	0	.84	14
PAC	4	-2	-3	-7	.55	5	-6	-9	-3	-2	.39	5
CAC	-8	3	-5	-5	.28	13	-9	-4	-3	-7	.42	13
FAL	5	17	9	5	.30	6	10	19	1	0	.27	6

TABLE 7 D, H

0.5 cph

Station	$d_D(u)$	$d_H(u)$	$d_D(v)$	$d_H(v)$	ϵ_d	N	$h_D(u)$	$h_H(u)$	$h_D(v)$	$h_H(v)$	ϵ_h	N
FAR	-17	8	-6	1	.21	14	3	-10	4	-8	.52	14
DIL	-17	9	-5	2	.21	12	-8	-6	-4	-3	.41	12
SAR	-7	11	0	-1	.25	7	9	3	-4	-11	.65	5
NAP	-6	4	-3	-1	.52	14	2	-3	2	-6	.74	14
DAV	2	1	4	3	.84	13	2	-3	9	0	.62	13
WIL	17	6	7	-3	.59	10	8	-1	1	-9	.75	10
AUB*	0						0					
PAC	7	-1	3	6	.84	6	-3	2	0	0	.88	6
CAC	6	-1	5	8	.57	12	2	4	3	-3	.70	12
FAL	21	-1	10	6	.41	9	4	3	5	7	.76	8
					1.0 cph							
FAR	-19	7	-7	1	.29	14	0	-18	2	-2	.45	14
DIL	-19	8	-4	1	.38	12	-11	-7	-3	-3	.58	12
SAR	-7	18	6	-2	.26	7	-6	3	0	-5	.70	5
NAP	-11	-5	-5	2	.55	14	2	-4	-1	-5	.87	14
DAV	5	3	10	2	.49	13	-2	-4	9	11	.63	13
WIL	20	10	12	-6	.50	10	11	-1	7	-20	.60	10
AUB*	0						0					
PAC	13	0	4	-5	.68	6	4	-1	-7	-5	.80	6
CAC	13	-1	0	4	.55	12	5	13	7	5	.31	12
FAL	33	9	13	5	.29	9	9	9	8	12	.39	8

TABLE 8 Z

	0.5 cph						1.0 cph					
Station	$z_D(u)$	$z_H(u)$	$z_D(v)$	$z_H(v)$	ϵ_z	N	$z_D(u)$	$z_H(u)$	$z_D(v)$	$z_H(v)$	ϵ_z	N
MON	52	20	11	8	.14	13	55	25	11	-1	.12	13
HAB	36	26	5	15	.46	9	40	37	5	14	.28	9
LIC	23	17	-7	8	.25	11	19	19	-9	2	.16	11
FRE*	14	8	-3	5	.29	13	10	9	-3	5	.14	13
TUR	27	11	-2	6	.16	3	18	6	-1	3	.09	3
BRI	11	-11	-8	-6	.43	11	11	-17	-6	-15	.30	11
	2.0 cph						4.0 cph					
MON	56	21	7	7	.11	10	70	19	17	-15	.21	10
HAB	40	43	3	7	.25	6	36	27	23	22	.25	7
LIC	21	24	4	4	.26	7	5	16	-5	-4	.22	7
FRE*	8	10	1	7	.22	11	9	13	5	7	.40	10
TUR	17	13	6	11	.19	7	21	17	10	16	.30	7
BRI	9	22	-2	-7	.14	7	-1	-24	-5	-6	.31	7

TABLE 8 D, H

0.5 cph

Station	$d_D(u)$	$d_H(u)$	$d_D(v)$	$d_H(v)$	ϵ_d	N	$h_D(u)$	$h_H(u)$	$h_D(v)$	$h_H(v)$	ϵ_h	N
MON	-18	15	-9	3	.15	13	-8	-4	4	-1	.54	13
HAB	-11	14	-4	0	.41	9	-2	3	1	22	.93	9
LIC	-2	5	-1	2	.81	11	-7	4	-1	1	.64	11
FRE*	0						0					
TUR	8	6	4	-1	.59	12	-5	1	-3	6	.71	12
BRI	14	-1	4	5	.39	11	0	9	-2	9	.70	11

1.0 cph

Station	$d_D(u)$	$d_H(u)$	$d_D(v)$	$d_H(v)$	ϵ_d	N	$h_D(u)$	$h_H(u)$	$h_D(v)$	$h_H(v)$	ϵ_h	N
MON	-25	23	-7	8	.19	13	-11	-3	-2	3	.51	13
HAB	-16	15	0	6	.49	9	-7	0	3	14	.95	9
LIC	-5	5	5	5	.91	11	-3	-6	-6	-1	.83	11
FRE*	0						0					
TUR	7	10	13	2	.53	12	-8	1	-4	15	.66	12
BRI	21	-12	2	0	.50	11	3	14	-3	15	.59	11

TABLE 9 Z

	0.5 cph						1.0 cph					
Station	$z_D(u)$	$z_H(u)$	$z_D(v)$	$z_H(v)$	ϵ_z	N	$z_D(u)$	$z_H(u)$	$z_D(v)$	$z_H(v)$	ϵ_z	N
CAB	26	36	2	15	.19	10	25	42	0	16	.12	10
PAR	11	24	-3	4	.13	4	7	27	-4	0	.09	4
COA	9	9	-8	1	.23	6	1	21	-13	-5	.22	6
FRE*	14	7	-4	4	.42	12	10	10	-1	6	.38	12
TUR	19	15	-1	11	.12	5	16	14	3	4	.18	5
YOS	14	0	-8	-2	.36	11	6	0	-6	-5	.47	11
BIS	8	-6	-10	-5	.32	9	0	-4	-8	-8	.41	9
	2.0 cph						4.0 cph					
CAB	27	51	0	3	.25	13	25	45	1	-10	.39	13
PAR	6	21	-6	-7	.18	5	5	17	-10	-11	.18	5
COA	1	18	-12	-9	.26	11	-11	7	-13	-14	.35	11
FRE*	9	15	-1	5	.37	14	7	13	8	10	.40	14
TUR	24	15	6	9	.34	5	31	11	10	17	.30	5
YOS	6	-1	-3	-5	.65	12	4	-6	-1	-2	.58	12
BIS	-1	-6	-6	-5	.55	14	-4	-10	-6	-6	.43	14

TABLE 9 D, H

0.5 cph

Station	$d_D(u)$	$d_H(u)$	$d_D(v)$	$d_H(v)$	ϵ_d	N	$h_D(u)$	$h_H(u)$	$h_D(v)$	$h_H(v)$	ϵ_h	N
CAB	-8	1	-1	-2	.57	10	-11	-7	-1	-2	.50	10
PAR	-9	-3	-1	-2	.13	4	-9	-5	-1	-3	.17	4
COA	-3	-1	0	-2	.74	6	-5	-5	-1	5	.24	6
FRE*	0						0					
TUR	-1	8	-2	-2	.80	6	-3	-4	-2	0	.80	6
YOS	5	-4	1	1	.80	11	0	1	-1	-1	.98	11
BIS	6	-4	2	2	.54	9	4	5	3	7	.71	9
					1.0 cph							
CAB	-11	1	-4	-2	.54	10	-9	-8	-1	-4	.52	10
PAR	-6	-11	0	-6	.15	4	-11	-4	0	13	.17	4
COA	-4	-6	2	-3	.83	6	-8	-3	-2	0	.60	6
FRE*	0						0					
TUR	0	0	-2	0	.90	6	-3	3	-2	-1	.85	6
YOS	4	-8	1	0	.75	11	1	4	2	2	.88	11
BIS	7	-11	-3	4	.65	9	10	4	4	19	.45	9

TABLE 10 D, H

0.5 cph

Station	$d_D(u)$	$d_H(u)$	$d_D(v)$	$d_H(v)$	ϵ_d	N	$h_D(u)$	$h_H(u)$	$h_D(v)$	$h_H(v)$	ϵ_h	N
LOM	-2	7	-5	-1	.43	10	-12	-5	-6	-9	.31	10
TAF	2	5	1	3	.89	8	-2	-4	2	-1	.67	8
MOJ*	0						0					
INY							3	-1	2	-4	.32	5
POR*	0						0					
LOP	31	10	-2	5	.28	5	2	4	5	5	.40	5
1.0 cph												
LOM	-10	-10	-9	3	.47	10	-13	-9	-2	-16	.37	10
TAF	-5	9	4	15	.53	8	-5	-6	3	4	.65	8
MOJ*	0						0					
INY							15	-2	1	-21	.43	5
POR*	0						0					
LOP	45	8	20	4	.30	5	-4	8	6	12	.28	5

TABLE 10 Z

	0.5 cph						1.0 cph					
Station	$z_D(u)$	$z_H(u)$	$z_D(v)$	$z_H(v)$	ϵ_z	N	$z_D(u)$	$z_H(u)$	$z_D(v)$	$z_H(v)$	ϵ_z	N
LOM	19	43	4	17	.16	10	25	46	-3	-12	.26	10
TAF	15	20	-3	7	.24	8	9	20	-3	-2	.15	8
MOJ*	6	13	0	9	.26	8	4	7	-5	1	.32	5
INY	5	12	-5	3	.40	5	-2	3	-7	2	.26	5
POR*	11	13	-5	12	.30	5	9	20	-2	3	.17	5
LOP	2	-1	-8	2	.48	5	1	1	-6	-6	.20	5
PRI*	29	-15	7	12	.49	9	34	-18	2	15	.25	9
LED*	13	-19	-6	17	.73	9	12	-15	-11	17	.52	9
ESP*	9	-11	-3	5	.76	9	4	-9	-4	9	.70	9
BUR*	18	-35	-2	23	.71	9	18	-19	-9	35	.52	9
BEL*	64	-12	1	-28	.47	6	43	-27	11	-22	.30	6
	2.0 cph						4.0 cph					
LOM	10	54	1	-19	.11	6	12	46	7	-30	.22	6
TAF	8	12	-14	-18	.29	5	0	-1	-11	-19	.35	6
MOJ*	5	12	4	-7	.21	6	9	9	6	-7	.15	6
INY	-7	-4	-11	0	.44	5						
POR*	1	16	1	2	.13	5	2	16	3	8	.16	5
LOP	-10	-5	-4	-6	.22	5	-7	-8	-5	-4	.21	5

TABLES 11–15

Second and Third Time Harmonic of Diurnal Variations during Quiet Days (Sec. 3.17)

Amplitudes are given in gammas and the angles refer to the phase of a cosine wave relative to zero hour 105°WMT (tab. 11) and 120°WMT (tabs. 12-15).

TABLE 11

Profile: Tucson, Ariz.–Sweetwater, Tex.; 1960 April 19-22

		2. harmonic			3. harmonic		
Station	Long. (°W)	D	H	Z	D	H	Z
TU	110.8	18.4 252°	5.4 160°	7.4 205°	8.6 49°	1.1 194°	2.5 11°
LOR†	108.6	17.9 251°	5.3 165°	4.6 203°	9.1 43°	.15 23°	2.2 5°
LAC	106.8	17.8 244°	5.2 168°	5.2 187°	8.7 37°	.24 109°	2.4 353°
COR	105.6	18.2 241°	5.3 159°	8.2 185°	9.1 32°	.55 205°	2.7 346°
CAR	104.2	16.3 242°	5.4 159°	6.7 175°	7.5 27°	.75 180°	3.2 329°
SWE*	100.5	16.2 233°	5.3 147°	10.4 182°	7.6 23°	1.2 181°	3.9 324°

† Uncontrolled temperature effect.

* Corrected for temperature variations.

TABLE 12

Profile: San Clemente Island, Calif.–Tucson, Ariz.;
1960 Aug. 31–Sept. 1, Sept. 9-11

		2. harmonic			3. harmonic		
Station	Long. (°W)	D	H	Z	D	H	Z
SAC	118.5	18.0 242°	4.9 159°	9.4 177°	11.1 43°	2.6 295°	5.9 353°
LAJ	117.3	21.0 238°	6.8 143°	13.8 173°	14.7 39°	5.0 274°	8.4 345°
ELA	117.0	21.0 239°	7.3 146°	12.7 176°	14.1 42°	4.5 289°	8.0 347°
ALP†	116.7	21.3 238°	7.3 150°		14.1 39°	4.1 281°	
CAM*	116.4	22.2 237°	5.6 152°	9.53 164°	13.7 39°	5.1 276°	5.1 331°
TU	110.8	21.2 221°	6.8 129°	8.8 163°	14.1 19°	4.5 253°	5.4 327°

† Uncontrolled temperature effect.

* Corrected for temperature variations.

TABLE 13

Profile: Farallon Islands, Calif.—Carson City, Nev.;
1961 Feb. 24-27, Mar. 2, April 5, 6, 17

		2. harmonic			3. harmonic		
Station	Long. (°W)	D	H	Z	D	H	Z
FAR	123.0	12.5 276°	7.8 181°	10.7 206°	5.3 84°	3.85 24°	6.6 28°
DIL	123.0	11.5 276°	6.8 175°	11.6 207°	4.9 86°	3.6 15°	6.2 27°
NAP	122.3	12.8 271°	7.0 180°	7.4 203°	5.4 80°	4.1 20°	4.3 28°
DAV†	121.8	12.5 268°	8.1 175°	6.9 209°	5.2 75°	4.2 12°	4.5 26°
AUB	121.1	12.7 270°	7.3 176°	8.6 208°	5.1 76°	3.5 16°	4.3 26°
CAC	119.8	10.8 271°	7.2 174°	5.3 205°	4.9 83°	4.6 16°	3.1 23°

† Uncontrolled temperature effect.

TABLE 14

Profile: Monterey–Bridgeport, Calif.; 1961 Oct. 16-18

		2. harmonic			3. harmonic		
Station	Long. (°W)	D	H	Z	D	H	Z
MON	121.4	8.7 254°	7.4 147°	9.6 192°	6.4 52°	1.8 347°	6.4 359°
LIC	121.7	10.0 255°	7.8 145°	7.5 188°	6.5 53°	1.7 353°	4.9 8°
FRE	119.8	9.6 253°	8.7 140°	5.8 176°	6.1 42°	2.1 343°	4.1 1°
BRI	119.2	9.7 255°	6.5 147°	6.1 206°	7.0 44°	0.2 243°	4.1 5°

TABLE 15

Profile: Cambria–Bishop, Calif.; 1961 Nov. 29, Dec. 12-18

		2. harmonic			3. harmonic		
Station	Long. (°W)	D	H	Z	D	H	Z
CAB	121.1	9.3 274°	6.7 187°	7.5 193°	5.6 97°	4.6 19°	5.2 34°
COA*	120.4	9.9 269°	6.5 191°	4.5 196°	5.4 93°	4.4 23°	3.3 42°
FRE	119.8	9.0 273°	6.9 189°	4.9 203°	5.2 94°	4.8 19°	3.2 41°
YOS	119.7	9.0 273°	6.8 191°	4.0 211°	5.0 100°	4.9 25°	2.7 51°
BIS	118.4	9.1 269°	6.7 183°	3.6 213°	5.1 87°	4.8 16°	2.1 43°

*Corrected for temperature variations.

TABLE 16

Amplitude Ratio of Vertical to Horizontal Pulsations (sec. 3.17)

Station		Station		Station	
TU	<0.1	SAC	0.1	FAR	0.3
LOR	<0.1	LAJ	0.9	DIL	0.3
LAC	0.3	ELA	0.4	NAP	0.2
COR	0.1	ALP	0.1	DAV	0.3
CAR	0.3	CAM	<0.1	AUB	0.2
SEM	0.1	YUM	0.2	PAC	<0.1
SWE	<0.1			CAC	<0.1
		CAB	0.4	FAL	0.1
MON	1.0	PAR	0.1		
HAB	0.7	COA	0.2	LOM	0.4
LIC	<0.1	FRE	0.5	TAF	0.3
TUR	0.6	YOS	<0.1	MOJ	0.1
BRI	0.1	BIS	0.1	POR	0.4
				LOP	0.1

EXPLANATIONS FOR PLATES I-VI

The plates represent enlarged photographic copies from the 16 mm recording film, to show the anomalous behavior of transient variations at various sites (original distance between hour marks: 5 mm). The notations are D, H, Z: magnetic elements; T: Temperature; B: base line. Clock corrections are given at the right-hand corner of each magnetogram.

PLATE I

"Rio Grande anomaly" during bay disturbance (profile: Lordsburg, New Mexico-Sweetwater, Texas); the bay begins with an "ssc"-like impetus at 21:36 (May 11, 1960) and the anomaly is evident from the reversal of Z between LAC and COR and the general increase of the Z-amplitude east at COR, CAR, SWE.

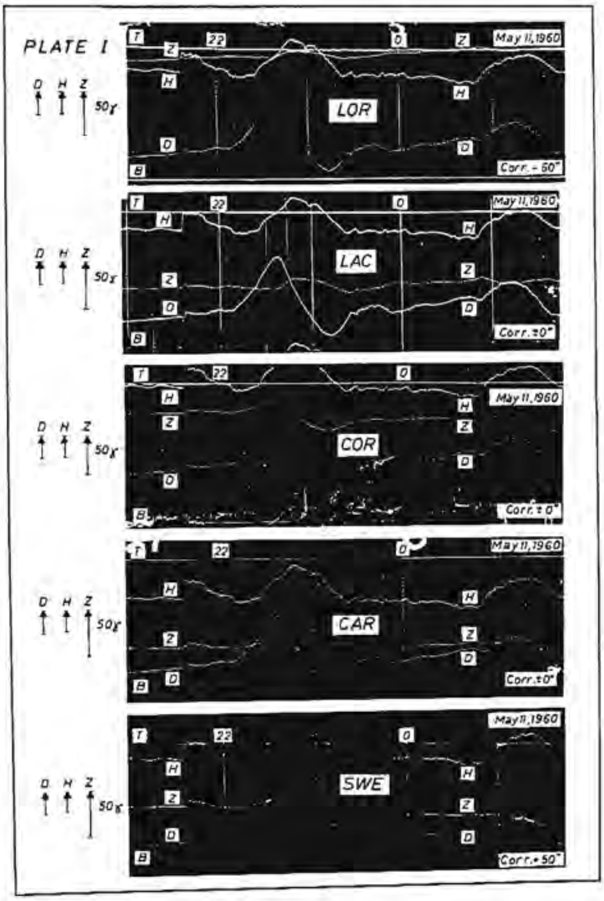

PLATE II

"Coastal anomaly in southern California" during magnetic storm (profile: San Clemente Island – Cameron, California + Dillons Beach north of San Francisco). The intensified Z-variations at the coast preserve a remarkable correlation to those in D; notice in particular the phase lead of Z relative to D at LAJ during the sinusoidal effect from 3:00 to 3:30.

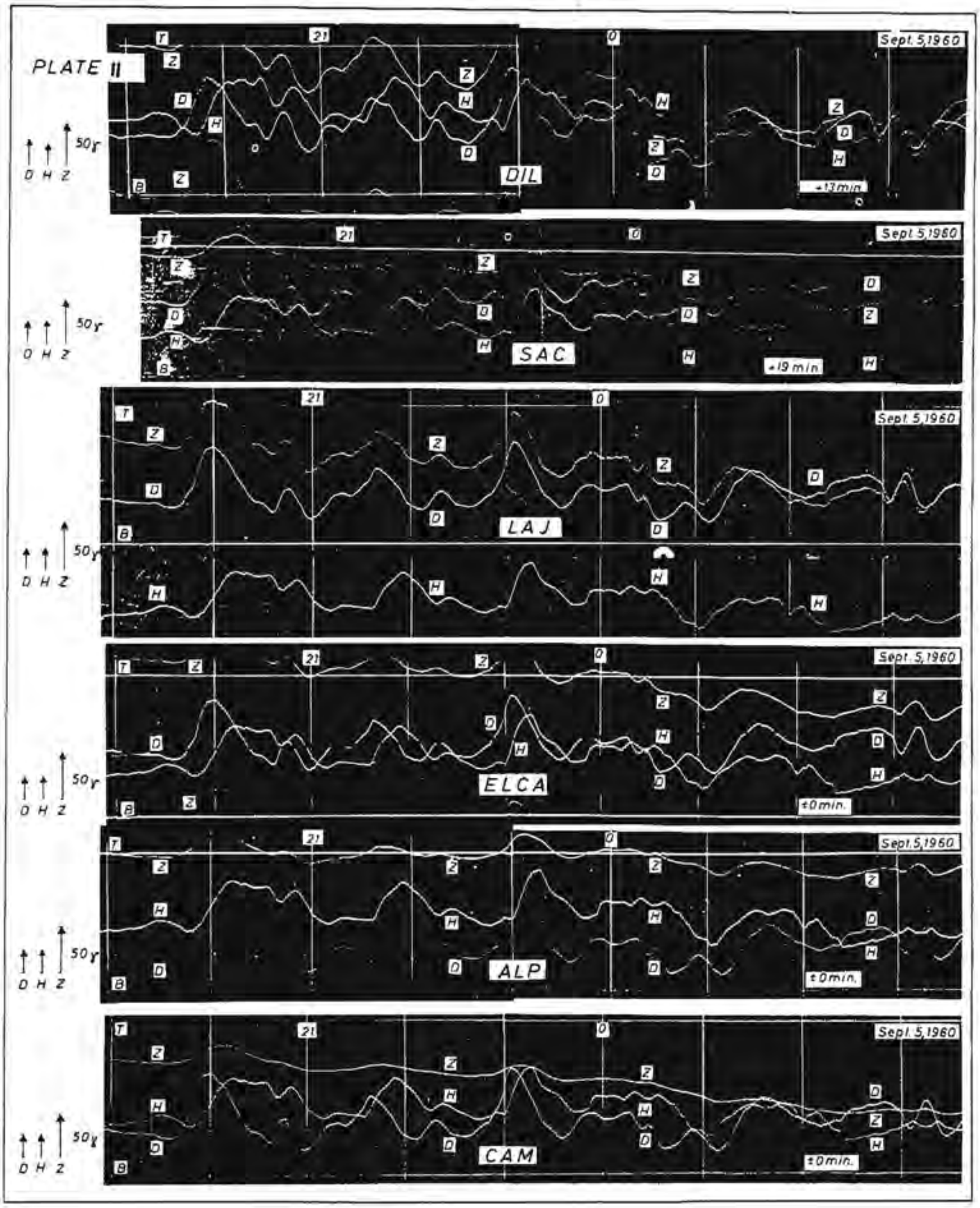

PLATE III

"Coastal anomaly in southern California" during sequence of short-period fluctuations; cf. Plate II.

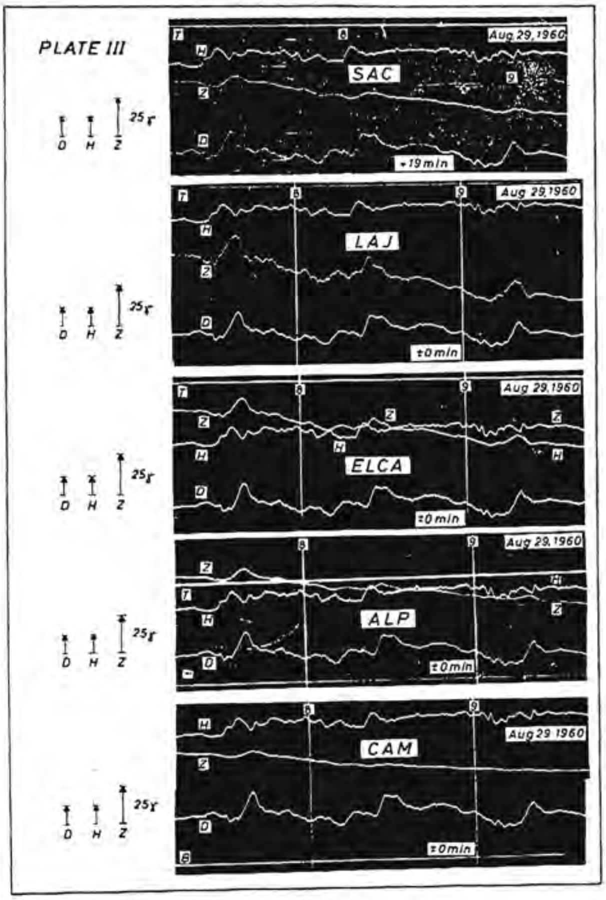

PLATES IV AND V

"Coastal anomaly and inland anomalies in central California" during bay disturbance (IV) and magnetic storm (V); profile Farallon Islands-Carson City, Nevada; intensified Z-variations at the coast (FAR, DIL), which are similar to those in D, phase shift of Z about 100 km inland (NAP, ANG), and reversal of Z across the Sierra Nevada (CAC).

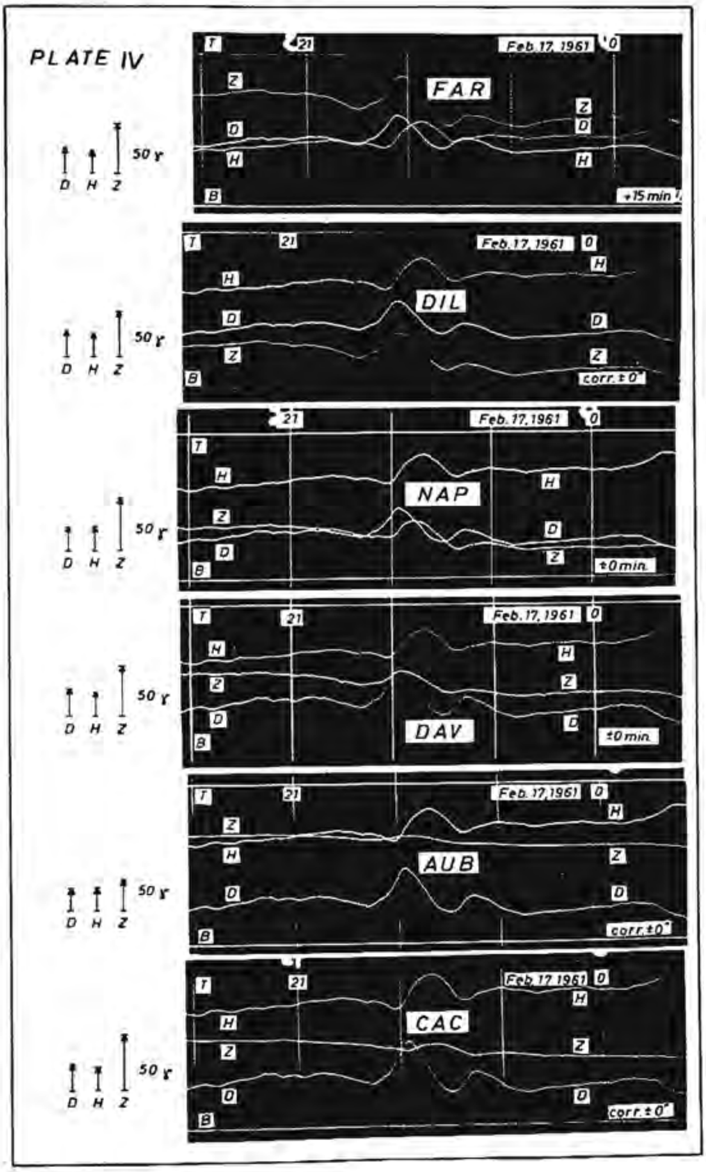
PLATE IV

PLATE V

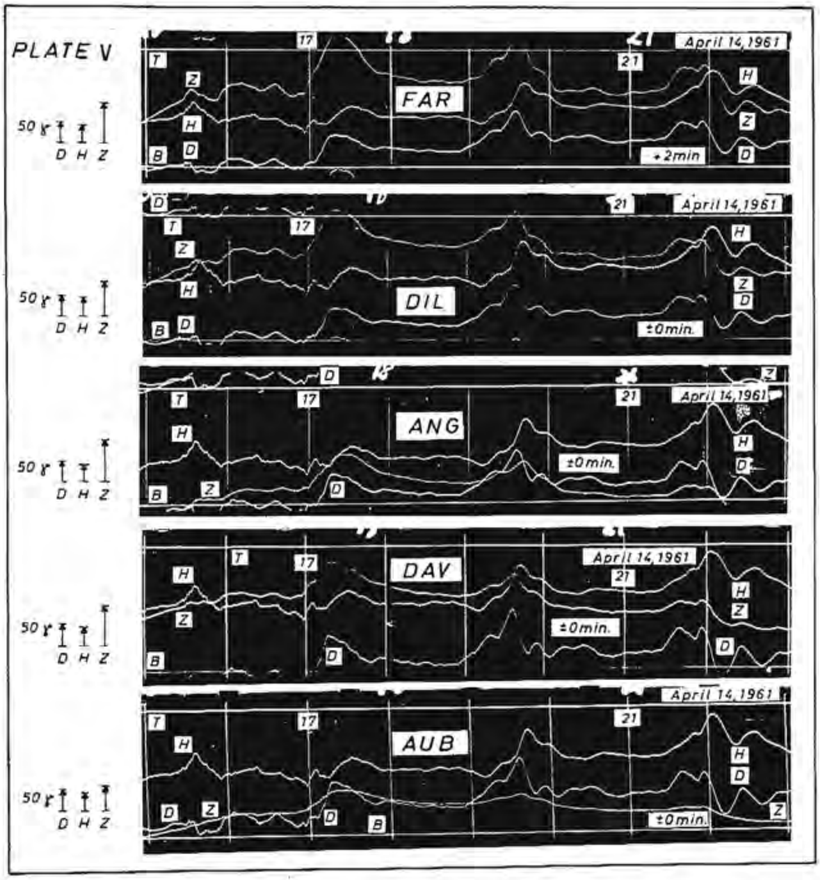

PLATE VI

Short-period fluctuations on the profile Farallon Islands – Carson City; cf. Plates IV and V; notice in particular that the Z-traces at the coastal station DIL appear smoother than those at the inland stations NAP, DAV, CAC reflecting the effect of shallow conductivity inhomogeneities on land (cf. tab. 16).